

# Development of a Heterodyne Interferometer For Nanometer Scale Displacement Measurement

by

Aaron Stibich  
B.Eng., University of Victoria, 1995

A Thesis Submitted in Partial Fulfillment of the  
Requirements for the Degree of

MASTER OF APPLIED SCIENCE

in the Department of Mechanical Engineering

We accept this thesis as conforming to the required standard

[Redacted Signature]

---

Dr. Y. Stepanenko, Co-Supervisor (Department of Mechanical Engineering)

[Redacted Signature]

---

Dr. S. Dost, Co-Supervisor (Department of Mechanical Engineering)

[Redacted Signature]

---

Dr. R. Podhorodeski, Departmental Member (Department of Mechanical Engineering)

[Redacted Signature]

---

Dr. G. Field, Outside Member (Precision MicroDynamics Inc.)

[Redacted Signature]

---

Dr. J. Bornemann, External Examiner (Department of Electrical Engineering)

© Aaron Stibich, 1997

University of Victoria

All rights reserved. This thesis may not be reproduced in whole or in part, by photocopy or other means, without the permission of the author.

Co-Supervisors: Dr. Y. Stepanenko

Dr. S. Dost

## **Abstract**

The following thesis discusses the development of a heterodyne interferometer for the purpose of nanometer scale displacement measurements. High resolution displacement transducers are employed in numerous applications, including vibration analysis, surface profiling, position control, tilt meters, and non-destructive quality evaluation of solid parts. The University of Victoria Institute for Robotics and Intelligent Systems (IRIS) research group has recently established a materials and mechatronics laboratory, creating a need for a high resolution displacement transducer. Design criteria for this device are sub-nanometer resolution, a sample rate of approximately 1 kHz, a dynamic range (measurement range / resolution) of  $1 \times 10^7$  or more, and enough flexibility and robustness to take measurements in a variety of research projects. Research into the available technologies led to the conclusion that a heterodyne interferometer was the best candidate. This technique has a wide bandwidth, excellent dynamic range, and is highly resistant to noise. A heterodyne interferometer was successfully assembled and calibrated with 1 nm accuracy and sub-nanometer resolution.

Examiners:

[Redacted]

---

Dr. Y. Stepanenko, Co-Supervisor (Department of Mechanical Engineering)

[Redacted]

---

Dr. S. Dost, Co-Supervisor (Department of Mechanical Engineering)

[Redacted]

---

Dr. R. Podhorodeski, Departmental Member (Department of Mechanical Engineering)

[Redacted]

---

Dr. G. Field, Outside Member (Precision MicroDynamics Inc.)

[Redacted]

---

Dr. J. Bornemann, External Examiner (Department of Electrical Engineering)

# Table of Contents

Abstract .....	ii
Table of Contents .....	iv
List of Tables.....	vii
List of Figures .....	viii
Acknowledgments.....	x
Dedication .....	xi
1.0 Introduction.....	1
1.1 Objectives and Motivation.....	1
1.2 Thesis Outline .....	3
2.0 Review of High Resolution Displacement Measurement Techniques.....	4
2.1 Michelson Interferometry .....	5
2.2 Homodyne Three Phase Interferometry.....	8
2.3 White Light Interferometry.....	11
2.4 Fabry-Perot Interferometry .....	15
2.5 Capacitive Sensors .....	20
2.6 Comparison of Displacement Measurement Techniques.....	22
3.0 Heterodyne Interferometry.....	24
3.1 Theory .....	25
3.2 System Components .....	27
3.2.1 Helium-Neon Laser.....	27
3.2.2 Retardation Plate.....	28
3.2.3 Polarizing Beam Splitter .....	30

3.2.4	Bragg Cell .....	32
3.3	System Design .....	36
3.3.1	Zeeman Laser Heterodyne Interferometer .....	37
3.3.2	Bragg Cell Heterodyne Interferometer .....	38
4.0	Phase Demodulation .....	40
4.1	Phase Demodulation Circuitry .....	40
4.1.1	RF Circuitry .....	41
4.1.2	Low Frequency Circuitry .....	42
4.1.3	Circuit Design Considerations .....	43
4.2	Algorithm for Displacement Measurement .....	43
4.2.1	Amplitude Adjustment.....	45
4.2.2	Phase Measurement .....	45
4.2.3	Displacement Measurement.....	48
5.0	RF Noise .....	50
5.1	Beat Signal .....	50
5.2	Sources of RF Noise .....	51
5.3	RF Noise Reduction Techniques.....	52
5.4	RF Shielding .....	53
5.5	Amplitude Stabilization .....	55
5.6	RF Filtering.....	56
6.0	Displacement Errors.....	59
6.1	Low Frequency Noise .....	60
6.1.1	Cumulative Error .....	60
6.1.2	Non-cumulative Error .....	61
6.2	Medium Frequency Noise.....	61
6.3	Wide Band Noise .....	62
6.4	Noise Suppression.....	63
6.5	Compensation for Changes in Ambient Parameters .....	63
6.5.1	Pressure .....	65
6.5.2	Temperature .....	65
6.5.3	Humidity .....	66

6.5.4	Carbon Dioxide.....	66
7.0	Calibration Method.....	67
8.0	Results.....	70
8.1	Calibration.....	70
8.2	Displacement Error Analysis.....	73
8.2.1	Low Frequency.....	73
8.2.2	Medium Frequency.....	76
8.3	Measurement of Temperature Sensitivity.....	79
8.4	Bandwidth.....	89
9.0	Conclusion.....	90
9.1	Future Work.....	91
10.0	References.....	93
11.0	Appendix A.....	97

# List of Tables

Table 2.1	Comparison of displacement measurement techniques .....	22
Table 6.1	Sources of displacement errors .....	59
Table 6.2	Sensitivity of refractive index to environmental parameters .....	65

# List of Figures

Figure 2.1	Michelson interferometer.....	5
Figure 2.2	Interference fringes.....	6
Figure 2.3	Mach Zender interferometer.....	7
Figure 2.4	Three phase homodyne optical configuration.....	9
Figure 2.5	Three fringe intensity as function of phase.....	9
Figure 2.6	Theoretical fringe pattern of a white light interferometric system ....	12
Figure 2.7	White light interferometer.....	13
Figure 2.8	White light interferometer intensity time history.....	14
Figure 2.9	Fabry-Perot interferometer.....	15
Figure 2.10	Fabry-Perot interferometer interference fringes.....	17
Figure 2.11	Capacitive displacement transducer.....	20
Figure 3.1	HeNe laser.....	27
Figure 3.2	Retardation plate.....	28
Figure 3.3	Quarter wave plate - affect on linearly polarized light.....	29
Figure 3.4	Polarizing beam splitter.....	30
Figure 3.5	Rp and Rs as functions of angle of incidence.....	31
Figure 3.6	Polarizing beam splitter transmittance characteristics.....	32
Figure 3.7	Bragg cell.....	33
Figure 3.8	Diffraction of light by an acoustic wave.....	34
Figure 3.9	Light reflection from two equivalent acoustic wavefronts.....	35
Figure 3.10	Zeeman laser heterodyne interferometer.....	37
Figure 3.11	Bragg cell heterodyne interferometer.....	38
Figure 4.1	RF phase demodulator circuitry.....	41
Figure 4.2	Low frequency phase demodulator circuitry.....	42
Figure 4.3	Displacement measurement algorithm flow diagram.....	44
Figure 4.4	Phase measurement flow diagram.....	47
Figure 4.5	Displacement measurement flow diagram.....	48
Figure 5.1	Heterodyne interferometer beat signal.....	51
Figure 5.2	RF conductive shielding.....	52

Figure 5.3	Card entry filter .....	53
Figure 5.4	Reflection and absorption of RF shielding.....	54
Figure 5.5	Filtered beat signal.....	56
Figure 5.6	Phase detector RF output .....	57
Figure 5.7	Spectrum of phase detector output after first filter stage .....	58
Figure 7.1	Piezoelectric holder.....	67
Figure 7.2	Piezoelectric stepping circuit.....	68
Figure 7.3	Piezoelectric circuit output .....	69
Figure 8.1	Interferometer measurement of piezoelectric steps .....	70
Figure 8.2	Interferometer calibration data - Dec. 18.....	71
Figure 8.3	Interferometer calibration data - Feb. 15 .....	72
Figure 8.4	Interferometer long term drift - with tires.....	74
Figure 8.5	Interferometer long term drift - no tires.....	75
Figure 8.6	Interferometer short term drift - with tires.....	77
Figure 8.7	Interferometer short term drift - no tires .....	78
Figure 8.8	Temperature measurement circuit.....	79
Figure 8.9	Temperature and displacement measurement #1 .....	80
Figure 8.10	Periodic component of displacement and temperature #1 .....	81
Figure 8.11	Cross correlation of displacement and temperature #1.....	82
Figure 8.12	Temperature and displacement measurement #2 .....	83
Figure 8.13	Periodic component of displacement and temperature #2 .....	84
Figure 8.14	Cross correlation of displacement and temperature #2.....	85
Figure 8.15	Temperature and displacement measurement #3 .....	86
Figure 8.16	Periodic component of displacement and temperature #3 .....	87
Figure 8.17	Cross correlation of displacement and temperature #3.....	88
Figure 8.18	1/2 Hz square wave displacement.....	89

## **Acknowledgments**

I would like to thank Dr. Yuri Stepanenko, Dr. Sadik Dost, and Nick Audet for their support and patience.

To my dear wife, Melodie.

# 1.0 Introduction

## 1.1 Objectives and Motivation

High resolution displacement transducers have been employed in numerous applications. These applications include vibration analysis [21,22,23,28], surface profiling [11,29,30], position control [24], tilt meters [8,25], and non-destructive quality evaluation of solid parts [31]. Recently, a need was perceived in the University of Victoria Institute for Robotics and Intelligent Systems (IRIS) research group for a high resolution displacement transducer.

Since 1993, the IRIS group has been conducting research in the area of materials and mechatronics, focussing on the development and application of piezoelectric materials and structures. A laboratory has been established for piezoelectric materials processing. In addition, several graduate students are currently pursuing research on topics related to piezoelectric actuators.

A high resolution displacement transducer is required both as a means of characterizing the piezoelectrics being produced in the IRIS lab, and as a means of measuring the performance of the piezoelectric actuators used in our research. The transducer will be used to confirm the  $d_{xx}$  parameters of the manufactured piezoelectrics (see [1] for a description of  $d_{xx}$  parameters). The instrument can also be used to measure hysteresis, decay of the  $d_{xx}$  parameters, and frequency response of the piezoelectric actuators.

Unstacked piezoelectric actuators typically have a full scale deflection on the order of 100 nm. It is desirable in most measurement situations to have a resolution of at least 1/100th of the full scale. This will allow for detailed vibration analysis, and for observation of hysteresis effects. The transducer, therefore, must have a resolution of 1 nm or better.

The instrument must also be capable of measuring large displacements. Bimorph piezoelectric structures can have deflections on the scale of mm, meaning that measurement over a range of at least  $\pm 0.5$  cm must be easily accomplished. This calls for an extremely high dynamic range, defined as the ratio of measurement range to resolution. A 1 nm resolution, combined with a range of 1 cm gives a dynamic range of  $1 \times 10^7$  - far beyond the capabilities of most commercially available displacement transducers.

As stated earlier, the instrument can be used for dynamic analysis. Piezoelectric materials typically have extremely high natural frequencies (on the order of MHz), and are therefore capable of responding to very high forcing frequencies. However, these materials have sizable capacitances, making the power requirements of high speed motion impractical. Driving speeds of piezoelectric structures are typically limited to a few hundred hertz. The displacement transducer, therefore, must have a sample frequency of approximately 1 kHz.

Finally the instrument must be flexible and robust enough to take accurate displacement measurements in a variety of research areas. Current research topics in the materials and mechatronics laboratory include: development of a piezo electric motor, flutter control, and adaptive optics. The instrument will preferably be non-contact, to avoid loading of the surface. In addition, the instrument must be able to make measurements in confined spaces, on a variety of surfaces, and be less sensitive to vibration and alignment problems. In short, the measurement technique must accommodate the wide variety of piezo-electric materials and applications currently under research within the IRIS materials and mechatronics research group.

The objectives of this thesis are to build, calibrate, and test a high resolution displacement transducer. The instrument must have nanometer to sub-nanometer resolution, dynamic

---

range in excess of  $1 \times 10^7$ , a sample rate of approximately 1 kHz, and the capability to take accurate displacement measurements in a variety of research areas.

## 1.2 Thesis Outline

This thesis is comprised of nine chapters which can be grouped into 3 main categories: background, system design issues, and results.

Chapters two and three cover the background of high resolution displacement measurement. Chapter two is a review of various high resolution displacement transducers: Michelson interferometry, homodyne three phase interferometry, white light interferometry, Fabry-Perot interferometry, and capacitive sensors. The review of these techniques includes a comprehensive comparison and an explanation of why heterodyne interferometry was chosen. Chapter three describes, in detail, the two most prominent heterodyne techniques, including background theory and a description of the optical components involved.

The design issues involved in heterodyne interferometry are discussed in chapters four to seven. Chapter four describes the phase demodulation process. In this chapter, the RF circuitry involved is outlined and the algorithm for calculating the displacement is described. Chapters five and six are devoted to the many sources of noise involved in nm scale displacement measurements, as well as the steps taken to attenuate and/or compensate for this noise. Chapter five deals with the RF noise present in the high speed phase demodulation circuitry. Chapter six describes physical errors in the displacement measurement. In chapter seven the calibration method is described.

Finally, in chapter eight the results of various tests are given. This includes the calibration results, resolution and accuracy of the instrument, an analysis of displacement errors, and the measured relationship between temperature and drift.

The thesis is concluded in chapter nine by a short summary and recommendations for future work.

---

## **2.0 Review of High Resolution Displacement Measurement Techniques**

The field of high resolution displacement measurement began with the invention of the Michelson interferometer in 1880. In the past 100 years, the field has expanded considerably to include dozens of techniques. The most popular displacement measurement techniques are described in this chapter and compared on the basis of resolution, range, bandwidth, and robustness.

Note that only high resolution techniques are described here, defined as sub-micron. This rules out many popular displacement transducers such as the LVDT and linear encoders.

## 2.1 Michelson Interferometry

The Michelson interferometer is the most basic design on which all other interferometers have been developed. This type of interferometer employs a coherent light source and a beam splitter to create two beams: one beam reflects off the target and the other acts as a reference.

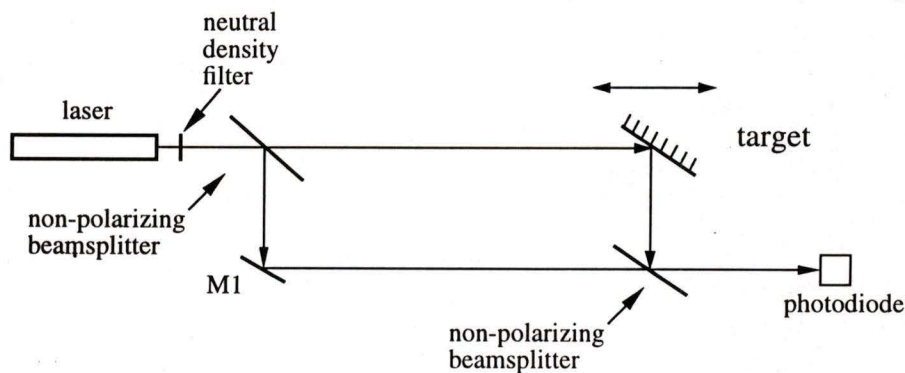


**Figure 2.1:** Michelson interferometer

Because the two beams are coherent and collimated, they interfere when recombined at the photodiode. The intensity of the interference fringe depends on the phase difference of the two beams. The equation for a linearly polarized monochromatic wave at any point P is given by

$$E_i(t) = A_i \cos(\omega t + \phi_i) \quad (2.1)$$

where:  $i$  = target ( $i=1$ ) and reference ( $i=2$ ) beam index

$A_i$  = amplitude of target and reference beams

$\omega$  = frequency of laser light

$t$  = time

$\phi_i$  = phase of target and reference beams

The intensity of the combined signal and reference beam is found by multiplying the combined electrical field by the conjugate

$$I(t) = \left( E_1(t) + E_2(t) \right) \times \left( E_1(t) + E_2(t) \right)^* \quad (2.2)$$

The resulting field intensity is given by

$$I(\Delta\phi) = I_1 + I_2 + 2\sqrt{I_1 I_2} \cos(\Delta\phi) \quad (2.3)$$

where:  $\Delta\phi = \phi_1 - \phi_2$

$$I_1 = 1/2 A_1^2$$

$$I_2 = 1/2 A_2^2$$

The detected intensity varies sinusoidally with the phase difference, as shown in figure 2.2. These alternating bright and dark bands in the intensity pattern are referred to as interference fringes and can be used to measure displacement.

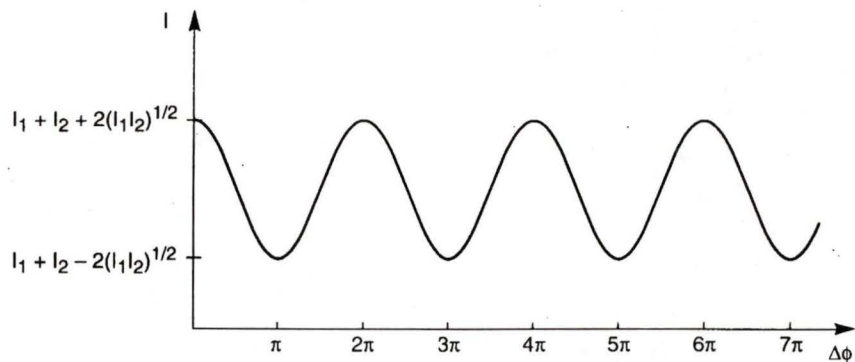


**Figure 2.2:** Interference fringes

The phase difference is related to the difference in the optical path lengths (OPL) between the source and the observation point for the two waves, named the optical path difference (OPD).

$$OPD = OPL_1 - OPL_2 = \left( \frac{\lambda}{2\pi} \right) \Delta\phi \quad (2.4)$$

where:  $\Delta\phi = 2\pi n$

$n$  = number of fringes counted

$\lambda$  = wavelength of laser light

As we move from one bright fringe to an adjacent bright fringe, the phase difference changes by  $2\pi$ , corresponding to a single wavelength of displacement (600 - 900 nm for visible light). It is this inherent precision that makes interferometry such a valuable tool.

Resolution can be increased by a factor of two by using a Mach Zender configuration, as shown in figure. In this type of interferometer, coherent light reflects off the target at a right angle. The laser beam travels the same path back, but is diverted before reaching the laser.

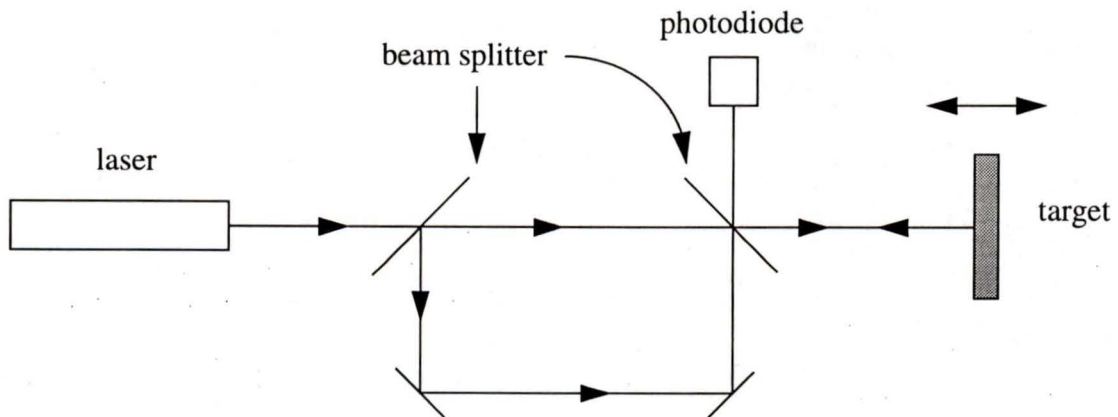


**Figure 2.3:** Mach Zender interferometer

Because the beam has travelled the same path twice, the OPD becomes

$$OPD = \left( \frac{\lambda}{4\pi} \right) \Delta\phi \quad (2.5)$$

Interferometer type displacement transducers have many advantages. The non-contact measurement eliminates loading of the surface under measurement. The instrument has very high spatial resolution, the ability to scan conveniently over multiple measured points, and high measurement bandwidth. In addition, conjunction with optical fibres gives the ability to measure under adverse environmental conditions in highly inaccessible locations, such as inside machinery or within the human body. Lastly, semiconductor, solid-state and rare-earth-doped fibre sources allow reduced system complexity, cost, and operation at a wider range of wavelengths.

Michelson and Mach Zender interferometers are limited in resolution due to inherent AM noise. The intensity of the interfering light is modulated by variations in the laser output intensity and ambient light. Without the use of noise suppression or compensation techniques, resolutions greater than  $\lambda/8$  (approximately 100 nm) are difficult to achieve.

The Michelson interferometer is extremely popular instrument, and applications are too numerous to mention. Some of the early contributors to the development of this instrument are Deffari [2,3] and Keller [4].

## 2.2 Homodyne Three Phase Interferometry

Three phase homodyne techniques have been developed successfully by Lawrence Mertz [5,6] to circumvent the AM noise inherent in amplitude based interferometry. A three phase homodyne interferometer has also been developed by Mark Johnson and Yves Delaporte using fibre optics [7].

The expression for two interfering beams is given in equation (2.3) and can be seen to have three degrees of freedom: the mean intensity  $I_1 + I_2$ , the fringe contrast  $2\sqrt{I_1 I_2}$ , and

the phase difference  $\Delta\phi$ . All of these parameters will vary with time. To increase resolution, it is essential to have at least three detector signals contributing their information toward the displacement measurement. Mertz [5,6] proposes the use of three detector signals corresponding to fringes having  $\pm 120^\circ$  phase relationships.

The optical configuration of the three phase homodyne interferometer used by Mark Johnson and Yves Delaporte [7] is shown in figure 2.4.

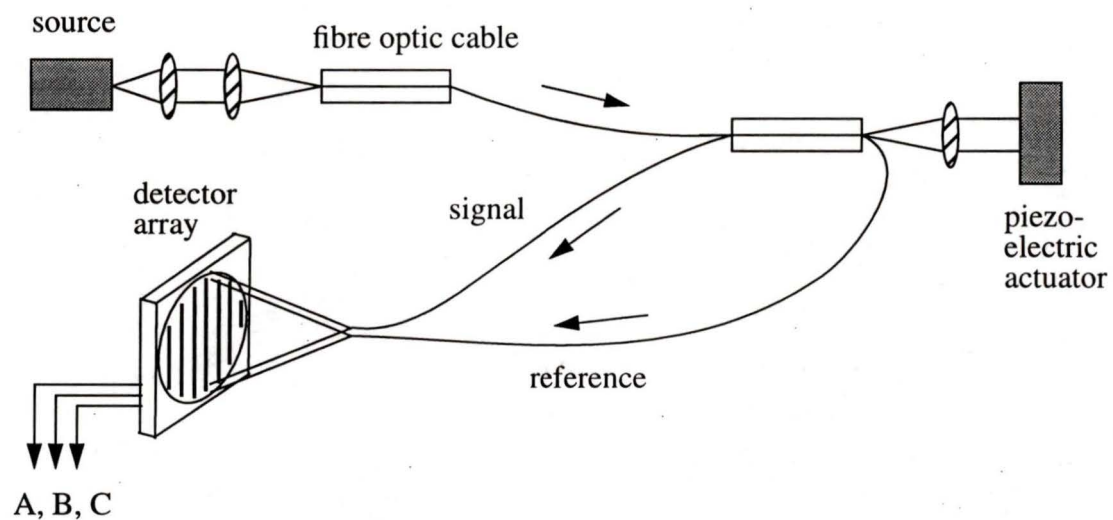


**Figure 2.4:** Three phase homodyne optical configuration

A 40 mW semiconductor laser is coupled into a polarization-maintaining single mode fibre. The beam is split into reference and signal, and the signal beam is reflected off a piezoelectric actuator which is used to provide a known displacement. The two beams are then allowed to recombine and exit the fibre optic. The combined beams create a periodic fringe pattern which is incident on a silicon detector array of 81 pixels. The three signals A, B, and C are chosen such that they are separated by a phase angle of  $120^\circ$ .

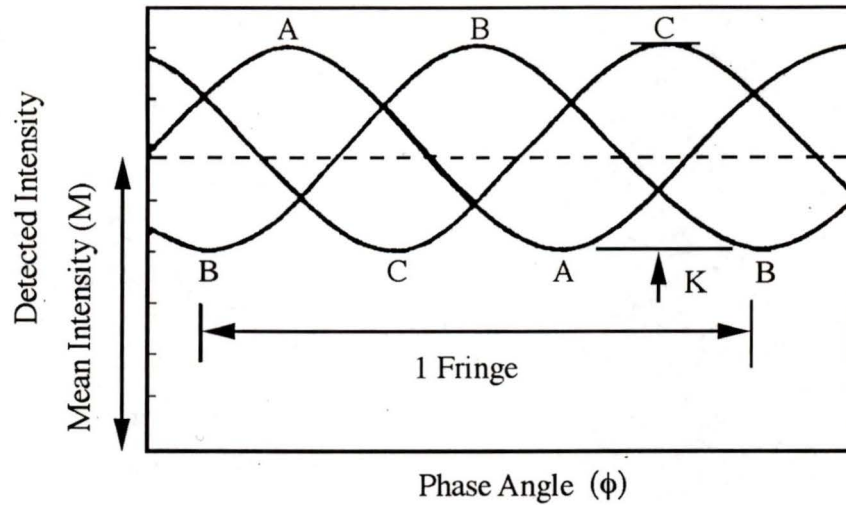


**Figure 2.5:** Three fringe intensity as function of phase

The three interferometer signals shown in figure 2.5 have the form

$$A = M + K\sin(\phi - 120^\circ) \quad (2.6)$$

$$B = M + K\sin(\phi) \quad (2.7)$$

$$C = M + K\sin(\phi + 120^\circ) \quad (2.8)$$

where:  $M$  = mean intensity  
 $K$  = fringe contrast  
 $\phi$  = phase angle

It is assumed that individual detector gains have been equalized and amplifier offsets have been removed. The complex convolution of A, B, and C can be written as

$$Z = Ae^{-\frac{2\pi i}{3}} + Be^{0i} + Ce^{\frac{2\pi i}{3}} \quad (2.9)$$

where the real part is

$$I = -\frac{1}{2}A + B - \frac{1}{2}C \quad (2.10)$$

and the imaginary part is

$$Q = -\frac{\sqrt{3}}{2}A + \frac{\sqrt{3}}{2}C \quad (2.11)$$

It can be assumed that any fluctuations in mean intensity or contrast will be reflected equally in A, B, C. If this is true, I and Q will not respond to changes in these parameters. The phase can now be calculated as

$$\phi = \text{atan}\left(\frac{Q}{I}\right) \quad (2.12)$$

Three phase homodyne interferometers have all of the advantages of the Michelson interferometer with the added advantage of AM noise compensation. The optics involved are easily procured and implemented, and are relatively low cost. Both Mertz and Johnson/Delaporte have reported nm scale resolution over bandwidths on the order of 10 kHz.

The three phase homodyne interferometer has 2 distinct disadvantages. The signal processing electronics required to transform A, B, and C into a phase measurement are complex and costly. The complexity may be reduced at the expense of measurement speed [5]. Secondly, the instrument must be carefully aligned to avoid phase error in the A, B, and C signals.

The three phase homodyne interferometer was successfully applied by Mertz to measure angular rotation [8]. The angle encoder is capable of measuring 13 prad to a bandwidth of 500 Hz, over a range of 18°.

## 2.3 White Light Interferometry

Low coherence or white light interferometry is a well established method for measuring range in a precise and unambiguous way. The method exploits the low coherence of the source to provide absolute measurements of the target position. White light interferometers, for measurement of point to point distance, were successfully developed and tested in the late 1980's. Among the contributors are Montgomery Smith and Chris Dobson at the University of Tennessee Space Institute [9], and Bruce Danielson and C. Boisrobert at the U.S. National Institute of Standards and Technology [10]. The technique has also been used for surface profile measurements by Leslie Deck and Peter de Groot at the Zygo Corporation [11].

The output pattern of a white light interferometer has a distinct visibility profile due to the low-coherence property of the light source. The reference and signal beams will interfere to produce maximum intensity only at the balanced position (reference and signal arms have equal length). As the target moves out of the balance position, the amplitude of the interference fringes falls off rapidly due to the wide line width of the source [12]. This is illustrated in figure 2.6.

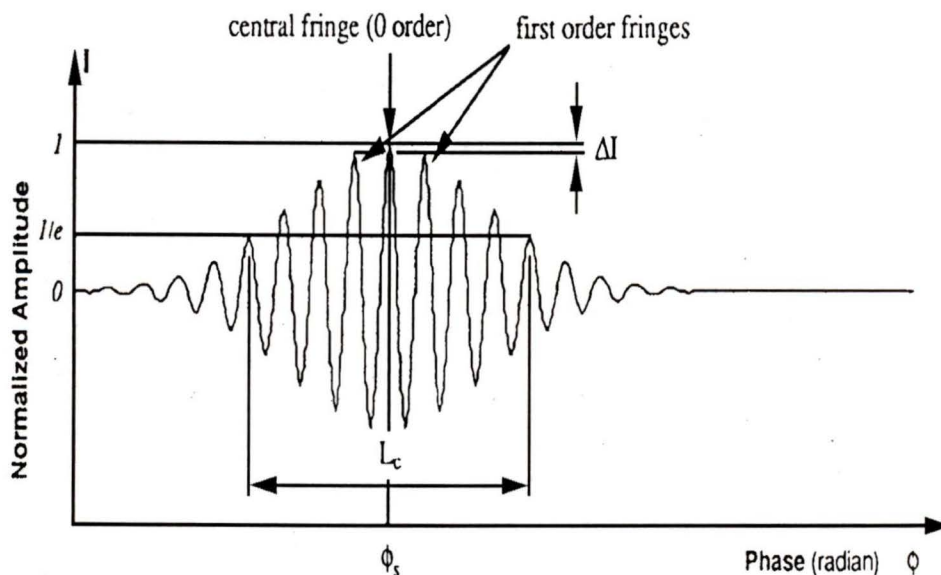


**Figure 2.6:** Theoretical fringe pattern of a white light interferometric system

The normalized output,  $I(\phi)$ , can be written as

$$I(\phi) = e^{-\left(\frac{\phi - \phi_s}{\pi L_c}\right)^2} \cos(\phi - \phi_s) \quad (2.13)$$

where:  $\phi$  = phase of signal beam at an arbitrary position  
 $\phi_s$  = phase of signal beam at the balanced position  
 $L_c$  = coherence length of source

The optical configuration used by Leslie Deck and Peter de Groot [11] is shown in figure 2.7. White light from a tungsten-halogen lamp is directed by a beam splitter to a Mirau-type interferometric objective [13].

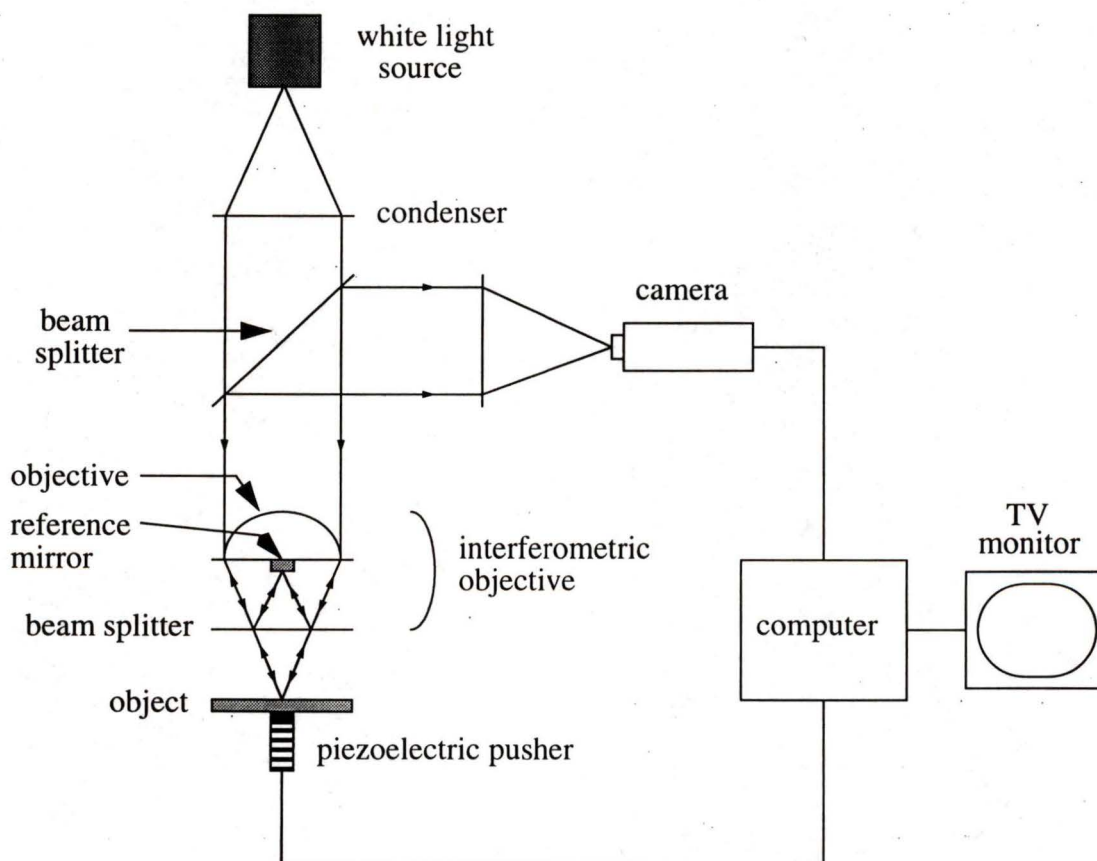


**Figure 2.7:** White light interferometer

The interferometric objective is designed such that the reference and signal beams are balanced when the surface of the object is at the focal point of the signal beam. Using a stacked piezoelectric, the object is translated as much as  $100\ \mu\text{m}$  along the optical axis. As the object translates, the camera monitors the intensity of the interference pattern. The intensity pattern time history during a  $100\ \mu\text{m}$  scan measured by Leslie Deck and Peter de Groot is shown in figure 2.8.

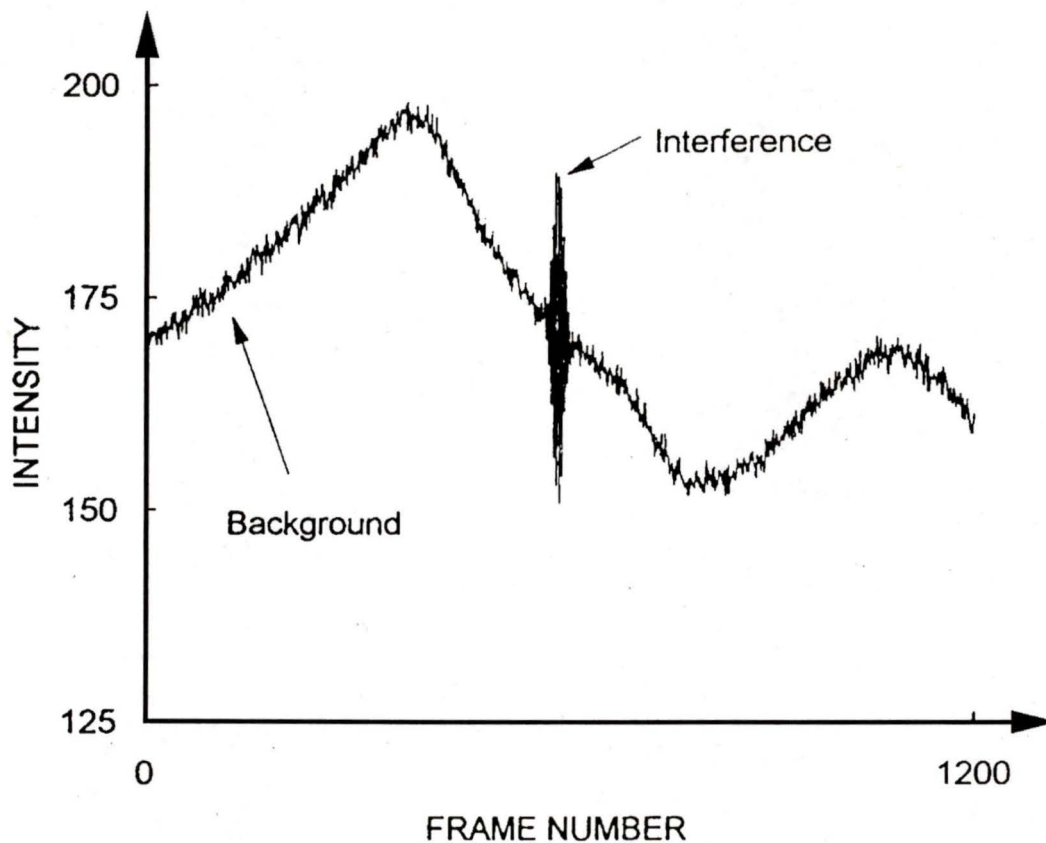


**Figure 2.8:** White light interferometer intensity time history

Because the interference is extremely localized, it generates a sharply defined coherence region only a few micrometers wide. The rest of the distribution represents low frequency background illumination that stems from test surface scatter and defocus. The position of the surface can be found by finding the point at which the interference intensity is maximum. This begins by using a high pass filter to remove the background noise. The signal is then averaged extensively, providing an accuracy of approximately  $\pm 10\ \text{nm}$  [9].

The intensity history shown in figure 2.8 was measured at one pixel of the camera. The instrument, therefore, can easily be used to measure surface profiles by monitoring multiple camera pixels.

The white light interferometer has the disadvantage of requiring excessive averaging and signal processing making for long measurement periods. The instrument typically requires ten seconds or more to make a single measurement. In addition, the interferometer is limited in range to only 100  $\mu\text{m}$ .

Reported applications of this technique include estimation of trench depth in integrated circuit devices [14], position measurement [15], and determination of the thickness of thin films [16].

## 2.4 Fabry-Perot Interferometry

The Fabry-Perot interferometer is a highly sensitive instrument used for measurement of sub-angstrom ( $1 \text{ nm} = 10 \text{ \AA}$ ) displacement measurements [17,18]. The optical configuration of a typical Fabry-Perot interferometer is shown in figure 2.9.

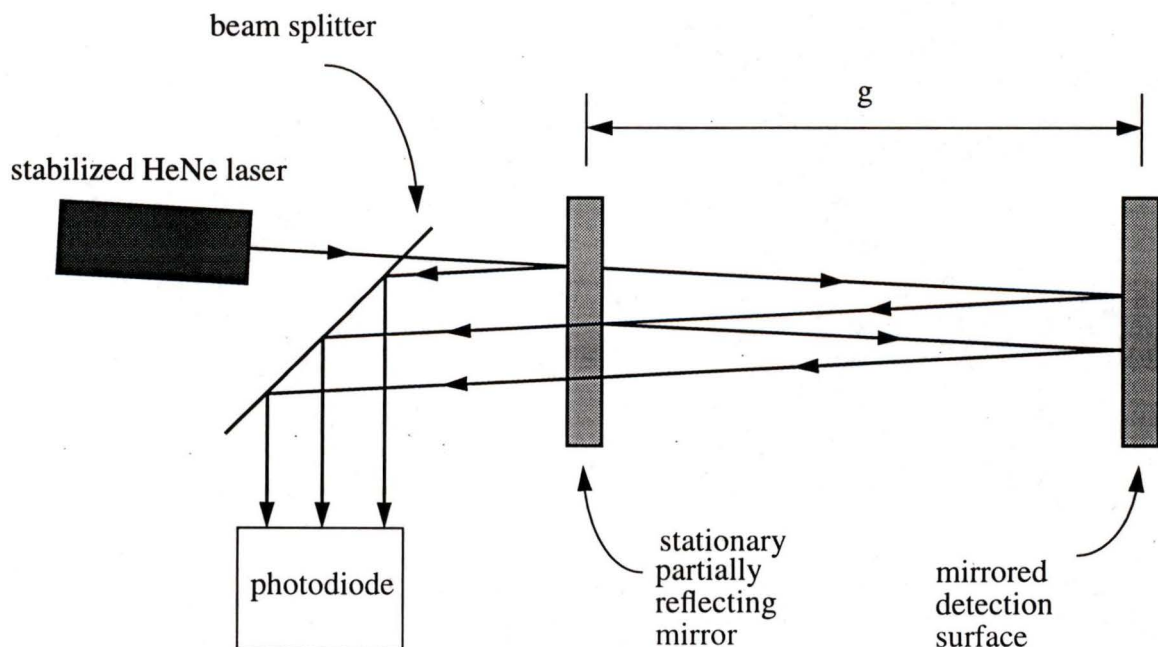


**Figure 2.9:** Fabry-Perot interferometer

A stabilized Helium-Neon (HeNe) laser is used as a light source. After passing through a 50/50 beam splitter, the laser beam is incident on a partially reflecting mirror typically having a reflection coefficient of 95% or higher. The transmitted light reflects multiple times inside the Fabry-Perot cavity creating a much more defined interference fringe. A more defined interference fringe means a steeper increase in intensity, which translates into higher sensitivity.

The basic sensitivity of the detector follows at once from the classic Fabry-Perot equations [19]. The reflected power  $P_r$  is related to the incident power  $P_i$  by

$$\frac{P_r}{P_i} = 1 - \frac{1}{1 + K \sin^2 \phi} \quad (2.14)$$

where:  $K = \frac{4R}{(1-R)^2}$

$R$  = reflectivity of mirror

$$\phi = \frac{2\pi g}{\lambda}$$

$g$  = mirror spacing

$\lambda$  = wavelength of laser

The power ratio as a function of mirror spacing is shown in figure 2.10, using  $R = 95\%$ .

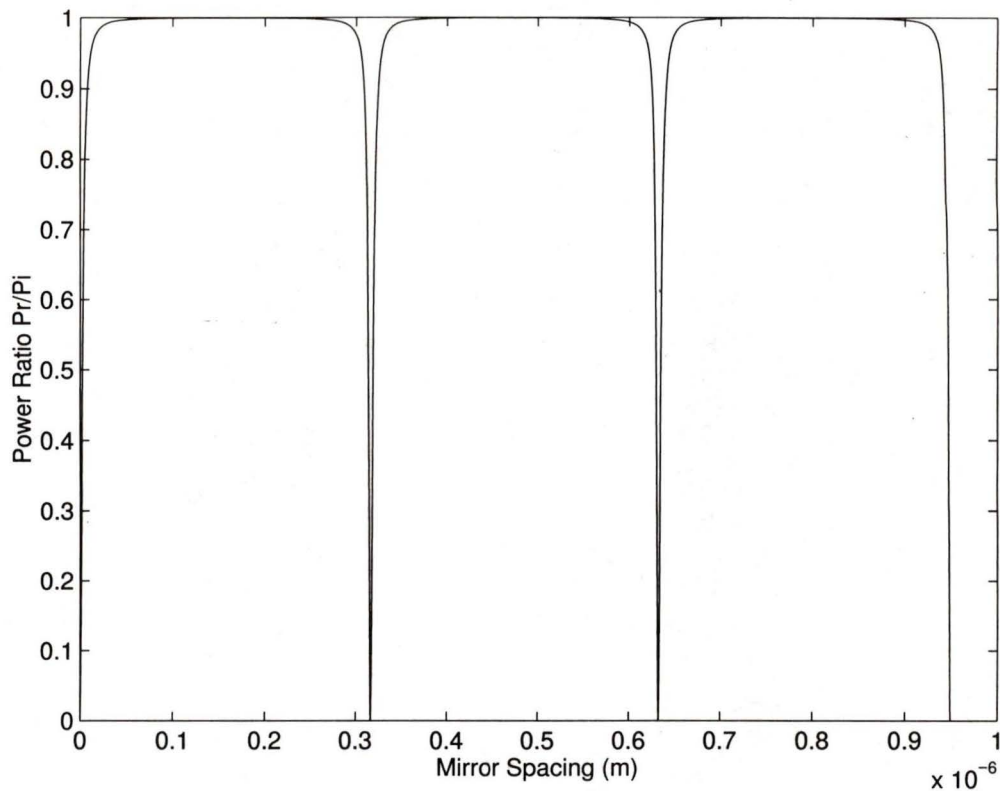


**Figure 2.10:** Fabry-Perot interferometer interference fringes

The sensitivity of the interferometer as a function of mirror spacing is given by

$$\sigma = \frac{d}{dg} \left( \frac{P_r}{P_i} \right) \quad (2.15)$$

One will normally bias  $\phi$  to a position of maximum sensitivity  $\phi_o$ . One can assume that the surface is highly reflective ( $K \gg 1$ ), and that the instrument is very near the bias position ( $\sin\phi \approx \phi$ ). Using these assumptions, the phase  $\phi_o$  can be expressed as follows (see Appendix A for proof)

$$\phi_o = \sqrt{\frac{1}{3K}} + m\pi \quad (2.16)$$

where:  $m = 0, 1, 2, \dots$

This leads to the expression for maximum sensitivity

$$\sigma_o = \frac{9\pi}{4\lambda} \sqrt{\frac{K}{3}} \quad (2.17)$$

To find the theoretical resolution of the Fabry Perot interferometer, we must determine the minimum noise level that can be attained. The two fundamental sources of noise in any photodiode signal, which cannot be avoided, are the Johnson and shot noise. Shot noise occurs due to both the quantized nature of light, and the time varying flux of photons incident on the photodiode (see section 6.3 for further detail). Johnson noise is the noise associated with thermal vibration of electrons. The electrons which allow current conduction in a resistor are subject to random motion which increases with temperature. This fluctuation of electron density will generate a noise voltage at terminals of a resistor [20]. Shot noise will dominate Johnson noise for sufficiently large laser power. This has led to Johnson noise generally being neglected in the field of interferometry.

At the optimum bias point as given by equation (2.16),  $P_r/P_i = 0.25$ , resulting in a corresponding standing current  $I_o$  in the detector.

$$I_o = \frac{P_r e \eta}{h\nu} = \frac{P_i e \eta}{4h\nu} \quad (2.18)$$

where:  $\eta$  = quantum efficiency of the diode

$h$  = Planck's constant

$\nu$  = laser frequency

This current gives rise to shot noise current  $i_n$ . Shot noise current is a white signal and is defined as a function of bandwidth.

$$i_n = \sqrt{2eI_o \Delta f} \quad (2.19)$$

where:  $\Delta f$  = bandwidth of sampling electronics

From equation (2.17) we can obtain the signal current  $i_s$  produced by a displacement  $\Delta g$  of the mirror.

$$i_s = \frac{1}{\sqrt{2}} \left( 3^{1.5} \cdot \frac{\pi}{4} \right) \left( \frac{\Delta g}{\lambda} \right) \left( \frac{e\eta P_i \sqrt{K}}{h\nu} \right) \quad (2.20)$$

Using equations 2.19 and 2.20 we obtain the signal-to-noise ratio

$$\frac{S}{N} = \frac{i_s^2}{i_n^2} = \frac{27\pi^2}{16} \cdot \frac{K\eta P_i \left( \frac{\Delta g}{\lambda} \right)^2}{\Delta f h\nu} \quad (2.21)$$

If we assume that a signal-to-noise ratio of unity represents the smallest detectable signal, the detection sensitivity of the system,  $\Delta g_{\min}$ , becomes

$$\Delta g_{\min} = \lambda \cdot \left( \frac{4}{3^{1.5} \pi} \right) \cdot \sqrt{\frac{\Delta f h\nu}{K\eta P_i}} \quad (2.22)$$

For a 1 mW HeNe laser, a reflectivity of 0.99, a system bandwidth of 1 Hz, and a quantum efficiency appropriate for an silicon photodiode,  $\Delta g_{\min}$  of the instrument is just over  $1 \times 10^{-7}$  Å - two orders of magnitude below the diameter of the hydrogen nucleus.

The most attractive feature of the Fabry-Perot interferometer is its incredibly high sensitivity - by far the most sensitive displacement transducer available today. In addition, the region where the laser beam carries phase information is confined to the space between the mirrors, which can be made very narrow (typically less than 1 mm). The requirements for mechanical stability of the apparatus are therefore very modest.

The disadvantages of the Fabry-Perot interferometer are considerable. The instrument is extremely limited in range. Displacements of more than a few nm will move the interference pattern out of the maximum sensitivity area. The instrument is also extremely sensitive to proper alignment of the Fabry-Perot cavity mirrors and great pains must be taken to

ensure that alignment remains constant. The displacement measurement is extremely sensitive to wavelength drift and intensity variations in the laser. The HeNe laser used in such an interferometer must be well stabilized.

## 2.5 Capacitive Sensors

Capacitive sensors are a well established displacement sensor used because of their high sensitivity, low cost, and ease of assembly. However, due to its limited range the number of applications for this device are limited. Capacitive sensors have been used for the detection of ultrasonic surface vibrations [21,22,23], closed-loop control of the separation of two objects such as the mirrors of a Fabry-Perot interferometer [24], and angular tilt meters [25].

The schematic diagram of the capacitive transducer and its associated electronics is shown in figure 2.11.

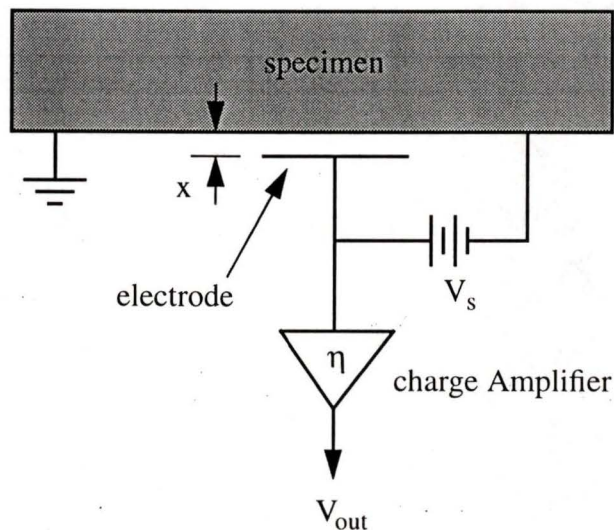


**Figure 2.11:** Capacitive displacement transducer

The circular electrode, of area  $A$ , is held at a distance  $x$  from the polished surface. A DC voltage ( $+V$ ) is applied to the electrode, with the sample surface at ground potential. Any change in the position of the surface causes the gap  $x$  to change by an amount  $\delta x$ . This results in a change in the capacitance ( $\delta C$ ) between the electrode and the surface, and

leads to the creation of a charge  $\delta q$  on the top surface of the electrode. The change in charge is given by

$$\delta q = V\delta C \quad (2.23)$$

Now substitute  $C = \frac{\xi A}{x}$ , where  $\xi$  is the dielectric constant in the gap.

$$\delta q = -\frac{\xi VA\delta x}{x^2} \quad (2.24)$$

The change in charge  $\delta q$  can be detected via a charge amplifier, where  $V_{out} = \eta q$ , giving an output voltage proportional to  $\delta x$ .

$$\delta V_{out} = -\frac{\eta\xi V_s A}{x^2} \delta x \quad (2.25)$$

The voltage signal  $\delta V_{out}$  is linearly proportional to the bias voltage  $V_s$  and inversely proportional to the square of the initial gap dimension  $x$ . Reducing the gap size greatly increases the instrument sensitivity at the expense of the maximum applied bias voltage. The electrode is typically placed within 10  $\mu\text{m}$  of the surface to provide maximum sensitivity, resulting in a limited range of approximately  $\pm 5 \mu\text{m}$ .

In addition to the poor dynamic range of the instrument, measurements are plagued by non-linearity. This can cause control problems unless advanced signal processing techniques are used. A second disadvantage of this instrument is its relative frailty. The electrode can be easily damaged due to arcing or accidental contact to the surface.

On the positive side, resolutions of 1 nm and better have been reported using this method over bandwidths in excess of 10 MHz. This transducer is non-contact and is more suitable than piezoelectrics for precise vibration analysis due to the absence of surface loading.

## 2.6 Comparison of Displacement Measurement Techniques

The techniques described in sections 2.1 to 2.5 can be compared based on the design criteria for the displacement transducer: resolution, range, bandwidth, and system robustness.

Resolution is defined as the smallest measurable displacement. Range is the largest displacement that can be measured before errors due to non-linearities or cumulative effects make the measurement unusable. All of the range values are given with respect to a reference. The frequency given in the bandwidth column is an estimate of the device's upper end corner frequency. Note that Michelson, three phase homodyne, and Fabry-Perot interferometers operate at the frequency of light (approximately  $10^{14}$  Hz) meaning that the corner frequency is defined by the capacitance of the photodiode used. Photodiodes are available that can detect frequencies in the GHz range. Finally the system robustness is given a rating of either excellent, good, or poor. Systems with excellent robustness are resistant to mechanical vibration, do not require precise alignment, and are able to make measurements in various applications with various types of surfaces.

**Table 2.1: Comparison of displacement measurement techniques**

Measurement Technique	Resolution	Range	Bandwidth	Robustness
Michelson	~100 nm	~±0.5 m	*	good
Homodyne three phase	~1 nm	~±0.5 m	*	poor
White light	~10 nm	~±50 μm	< 1 Hz	excellent
Fabry-Perot	~ $1 \times 10^{-7}$ Å	~±2.5 nm	*	poor
Capacitive	~1 nm	~±5 μm	~10 MHz	poor
Heterodyne	~0.1 nm	~±0.5 m	*	good

\* dependant on the capacitance of the photodiode

---

As stated in section 1.1, the displacement transducer must have a resolution of 1 nm or better, a maximum range of  $\pm 0.5$  cm or better, a sample rate of approximately 1 kHz, and must be flexible enough to make measurements on several types of transducers (eg. piezoelectric wafers, bimorphs, etc...). Table 2.1 shows that homodyne three phase interferometry comes close to satisfying all of the design criteria, but was not chosen due to its susceptibility to alignment problems. In addition homodyne three phase requires complex and expensive signal processing electronics. Only heterodyne interferometry, discussed in the next chapter, meets all of the design criteria.

---

## 3.0 Heterodyne Interferometry

A comparison of alternative displacement measurement techniques resulted in the conclusion that only heterodyne interferometry could satisfy all of the design criteria: nanometer scale resolution, dynamic range in excess of  $10^7$ , bandwidth of approximately 500 Hz, and robust operation. After the selection process was completed, the necessary optical, electrical, and computer components were procured. The thesis from this point onwards describes the work involved in assembling, de-bugging, and testing the heterodyne interferometer.

This chapter gives a general description of optical components used in heterodyne interferometry, as well as a description of the two most popular heterodyne techniques. This is followed by design issues, described in chapters four to seven. Chapter eight presents the calibration results, along with various measurements of drift, and the effect of temperature on drift. The thesis is concluded in chapter nine by a short summary and recommendations for future work.

Heterodyne interferometry was first proposed by Whitman and Korpel in 1969 for the analysis of acoustic surface perturbations [26]. The versatility of the design was later improved by Royer through the addition of a frequency shifting Bragg cell [27]. Output from this type of interferometer is exceptionally resistant from noise, allowing for interpolation into the sub-nanometer range. The device is inherently high speed and extremely

versatile. Heterodyne interferometers are also non-contact and have a dynamic range reported to be in excess of  $1 \times 10^9$ , making them suitable for a wide range of applications.

The many advantages of heterodyne interferometry have led to applications in a variety of fields. Heterodyne interferometers have been used in high resolution vibration analysis [28], surface profiling [29,30], and quality control [31].

### 3.1 Theory

Heterodyne interferometry frequency encodes the interference signal in order to avoid AM noise produced by laser intensity fluctuations and ambient light. This is accomplished by introducing a frequency difference between the signal and reference beams. The electric field of the two beams at any point P can be represented by the following relations

$$E_1(t) = A_1 \cos(\omega_1 t + \phi_1) \quad (3.1)$$

$$E_2(t) = A_2 \cos(\omega_2 t + \phi_2) \quad (3.2)$$

where:  $A_1, A_2$  = amplitude of the signal and reference beams  
 $\omega_1, \omega_2$  = frequencies of the signal and reference beams  
 $\phi_1, \phi_2$  = phase relative to the origin of the two waves at the point P.

The resultant intensity at P is then

$$I(t) = [E_1(t) + E_2(t)] \cdot [E_1(t) + E_2(t)]^* \quad (3.3)$$

expanding

$$I(t) = [A_1 \cos(\omega_1 t + \phi_1)]^2 + [A_2 \cos(\omega_2 t + \phi_2)]^2 + 2 \cdot [A_1 \cos(\omega_1 t + \phi_1)] [A_2 \cos(\omega_2 t + \phi_2)] \quad (3.4)$$

By substituting  $\cos^2(A) = 1/2(1+\cos(2A))$  and  $\cos(A+B) = \cos(A)\cos(B) - \sin A \sin B$ , equation (3.4) can be expressed as follows

$$I(t) = \left(\frac{A_1^2}{2}\right) + \left(\frac{A_2^2}{2}\right) + \frac{1}{2} [A_1^2 \cos 2(\omega_1 t + \phi_1) + A_2^2 \cos 2(\omega_2 t + \phi_2)] \quad (3.5)$$

$$+ A_1 A_2 \cos [(\omega_1 + \omega_2)t + (\phi_1 + \phi_2)] + A_1 A_2 \cos [(\omega_1 - \omega_2)t + (\phi_1 - \phi_2)]$$

The output from the photodetector, which cannot respond to the components at frequencies of  $2\omega_1$ ,  $2\omega_2$ , and  $(\omega_1 + \omega_2)$ , becomes

$$I(t) = \frac{1}{2}A_1^2 + \frac{1}{2}A_2^2 + A_1 A_2 \cos [(\omega_1 - \omega_2)t + (\phi_1 - \phi_2)] \quad (3.6)$$

The output from the photodetector is a D.C. current modulated by a periodic signal at a frequency  $(\omega_1 - \omega_2)$ , known as the beat signal. The phase of the beat signal is measured and used to determine displacement.

$$\Delta x = \left(\frac{\Delta\phi}{2\pi}\right) \cdot \frac{\lambda}{2} \quad (3.7)$$

where:  $\Delta\phi = \Delta(\phi_1 - \phi_2)$

Sections 3.2 and 3.3 deal with the optics involved in heterodyne interferometry. Section 3.2 describes the individual components used, and section 3.3 describes the overall optical configuration.

## 3.2 System Components

Before describing the optical design of the heterodyne interferometer, it is necessary to briefly explain the functions and underlying principles of the various components. The following are the most common components used in heterodyne interferometry.

### 3.2.1 Helium-Neon Laser

The Helium-Neon (HeNe) laser is an electrically pumped gas laser which usually produces a red beam at 632.8 nm. Relative to semiconductor lasers, this particular laser is fragile, inefficient, bulky, and requires a high operating voltage. However, light generated by the HeNe laser has an extremely narrow line width and high quality wavefronts, two specifications which are essential to high resolution phase measurement.

A HeNe laser is a gas-filled tube with internal electrodes exciting the gas to emit light. Mirrors on each end of the tube define the laser cavity. Early HeNe lasers were quite simplistic, but over the years manufacturers have incorporated a number of refinements in order to improve performance. Figure 3.1 shows the internal structure of a typical modern HeNe laser with output in the milliwatt range (reproduced and modified from [32]).

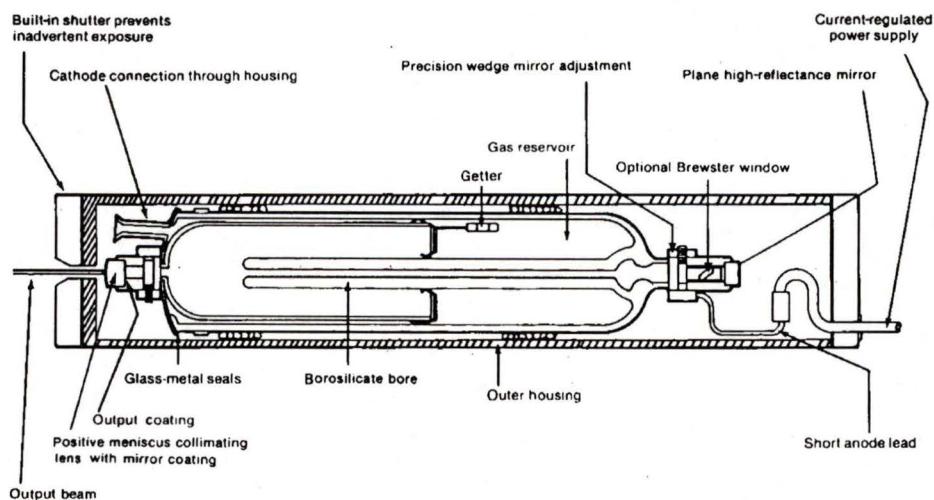


**Figure 3.1:** HeNe laser

The discharge passes from the cathode to the anode at the other end through a capillary bore, which is only a few mm in diameter. The capillary structure concentrates the discharge, thus improving overall efficiency. The small diameter of the discharge bore also helps control laser beam diameter, mode, and beam divergence. In a standard Helium-Neon laser, one mirror is totally reflective, while the one at the opposite end of the cavity transmits about 1 percent of the light which becomes the external laser beam. The Brewster's window is used to polarize the laser output.

Lasing occurs in the active medium when electrons passing through the active medium collide with both the Helium and Neon atoms, raising them to excited levels. The more abundant helium atoms collect most of the electrical energy, then transfer that energy readily to neon atoms which have an excited state at about the same energy above their ground states. The neon atoms then lose their excitation energy and drop to lower energy levels via several transitions. The wavelength an individual laser emits depends on the choice of optics and operating condition of the tube.

### 3.2.2 Retardation Plate

The retardation plate is a birefringent, uni-axial material in which the P and S polarization states travel at different speeds. This is accomplished using a non-isotropic, single crystal material with different refractive indexes along the P and S polarization planes.

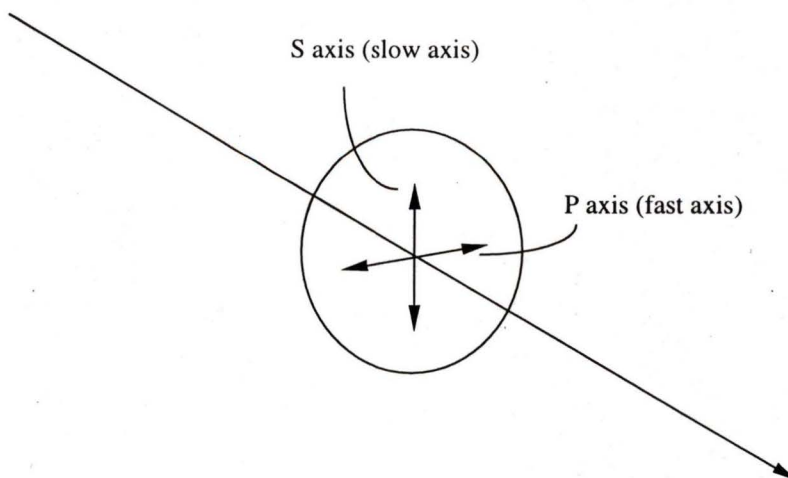


*Figure 3.2: Retardation plate*

Retardation plates can be designed to create any desired phase lag between the P and S by controlling the thickness and refractive index of the material; typical commercially available retardation plates are  $\lambda/4$  (quarter wave plate),  $\lambda/2$  (half wave plate), and  $\lambda$  (full wave plate). The lag relationship is given by equation (3.8).

$$N\lambda = \pm d(n_s - n_p) \quad (3.8)$$

where:  $N$  = phase lag (1/4, 1/2 or 1)  
 $d$  = crystal thickness  
 $n_s$  = S polarization plane refractive index  
 $n_p$  = P polarization plane refractive index

A  $\lambda/4$  wave plate is used in the design of a heterodyne interferometer. The 90 degree phase shift of the P polarization state causes a linearly polarized beam to become elliptically polarized, where the eccentricity is determined by the plane of polarization. The eccentricity of the retarded beam as a function of incident polarization is shown in figure 3.3. Note that if the incident beam is completely polarized in the S or P axis, there will be no change in the polarization state; if the plane is at 45 degrees, the polarization state will become circular.

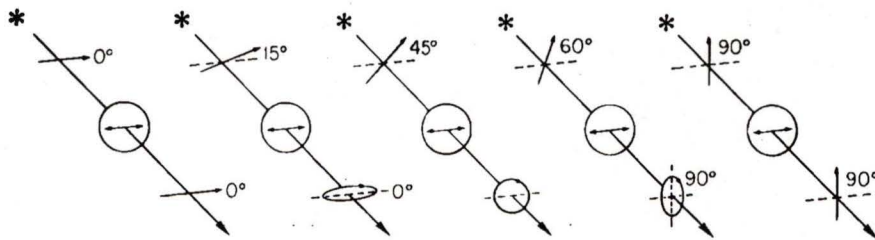


**Figure 3.3:** Quarter wave plate - affect on linearly polarized light

The  $\lambda/4$  wave plate is typically used in Mach Zehdner type interferometers to isolate the laser from feedback. A linearly polarized beam at a 45 degree angle is passed through the  $\lambda/4$  wave plate, bounced off the target, and then passes through the  $\lambda/4$  wave plate again.

This shifts the polarization state by 90 degrees and allows the reflected beam to be separated from the incident (see figure 3.11 for an illustration).

### 3.2.3 Polarizing Beam Splitter

The polarizing beam splitter can function as a polarizer, beamsplitter, or both. It consists of a pair of right angle prisms, hypotenuse face to hypotenuse face, with a special multi-layer dielectric film designed to act as a series of Brewster's angle polarizers (reproduced from [33]).

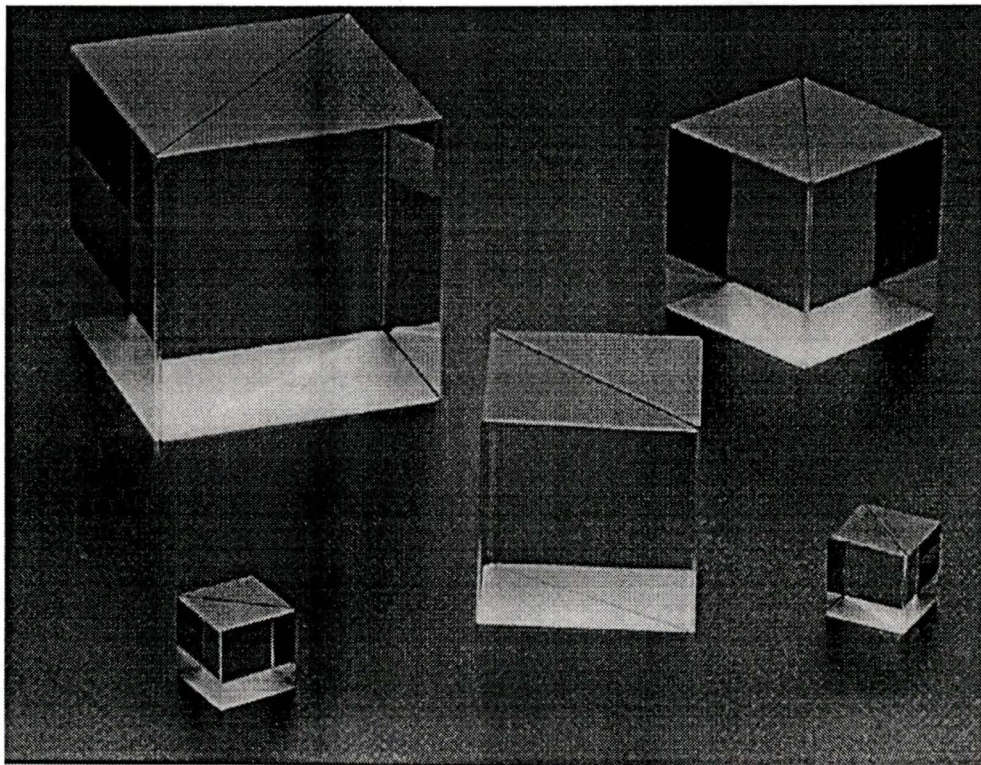


*Figure 3.4: Polarizing beam splitter*

The Brewster's angle is defined as the angle of incidence at which the reflectance of the P plane polarization state is minimum. The relationship between  $R_p$ ,  $R_s$  and the angle of incidence is a function of the material and the change in refractive index between the air and the Brewster's lens, or in this case, between the prism and the multilayer dielectric film. The relationship in four specific materials is shown in figure 3.5 (reproduced with modifications from [35]).

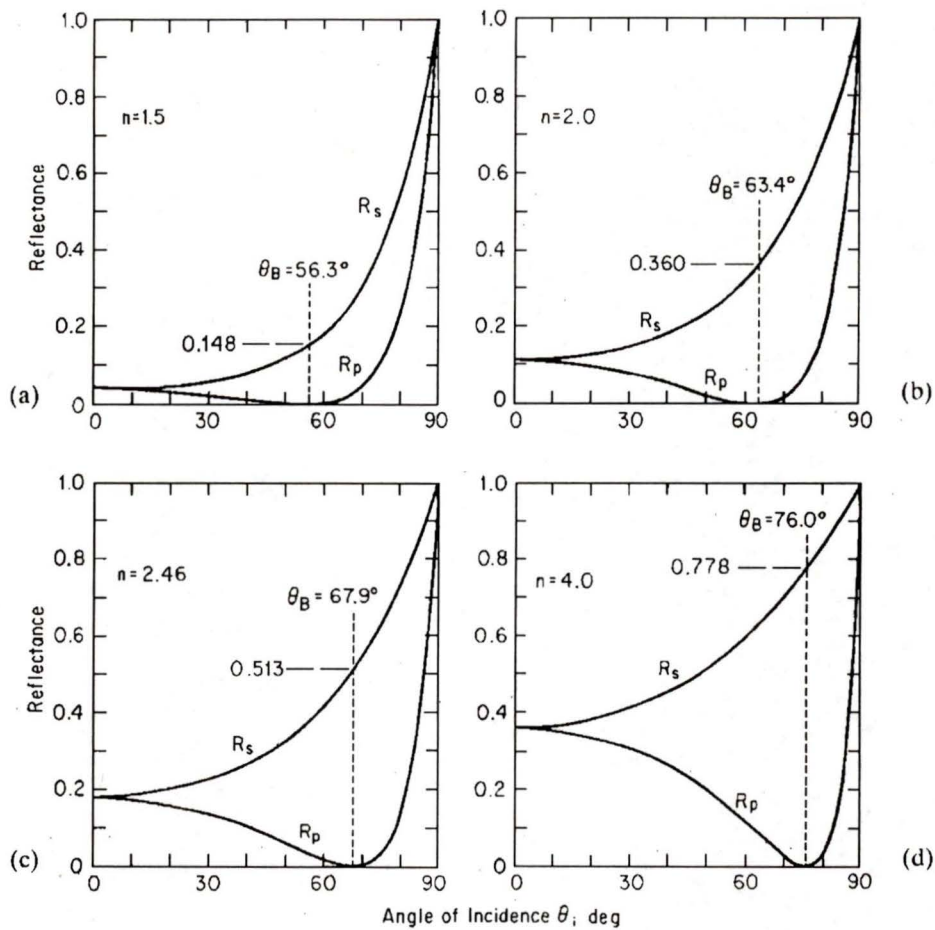


**Figure 3.5:**  $R_p$  and  $R_s$  as functions of angle of incidence

- where:
- (a) Alkali halides in ultraviolet and sheet plastics in infrared
  - (b) AgCl in infrared
  - (c) Se in infrared
  - (d) Ge in infrared

The ratio between  $R_p$  and  $R_s$  at the Brewster's angle increases with increased refractive index, but the Brewster's angle also increases with increased refractive index. The performance of the polarizer can be improved by placing many Brewster's angle polarizers in succession, known as a "pile of plates" polarizer. This is the case in the polarizing beam splitter. The dielectric film consists of many layers, acting as a pile of plates polarizer. At

every dielectric interface within the stack, the radiation is incident at or near Brewster's angle, and the P-polarized component is transmitted with almost no reflection. The S-polarized component, in contrast, is partially reflected at each interface. When a resonance condition exists among these many partial reflections, the total reflectance of the stack for S-polarized radiation is raised to 97% or better (modified images from [34]).

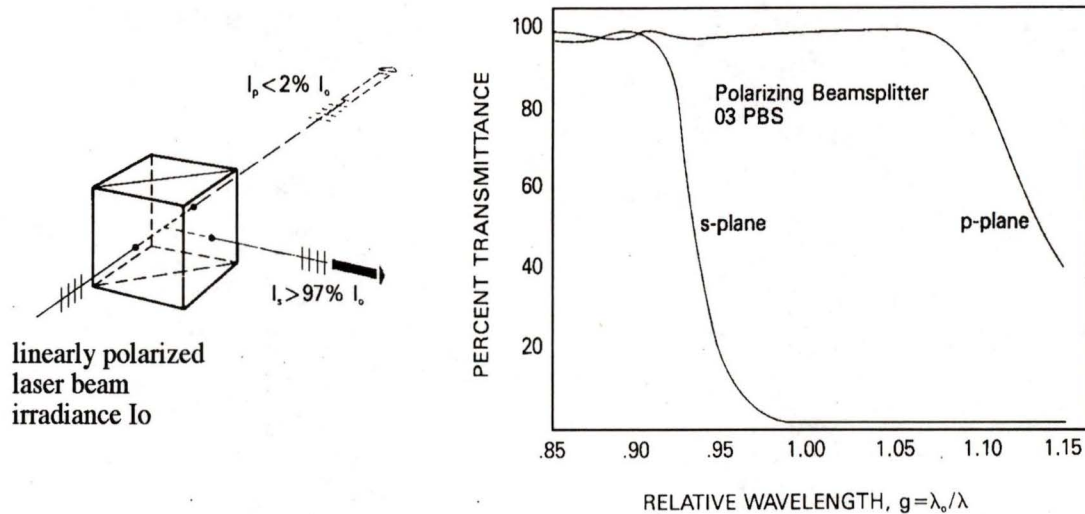


**Figure 3.6:** Polarizing beam splitter transmittance characteristics

The polarizing beam splitter is used in conjunction with the  $\lambda/4$  wave plate to prevent feedback into the laser cavity, as shown in figure 3.11.

### 3.2.4 Bragg Cell

A Bragg cell uses acoustic signals to diffract and modulate an incident laser beam. Diffraction of light by sound waves was predicted by Brillouin in 1922 [36], and has proved to be a convenient means of controlling the frequency, intensity, and direction of an optical beam. The following is a general description of the Bragg cell operation, without a detailed analysis of acousto-optic theory.

The Bragg cell consists of a quartz crystal with an acoustic transducer attached at one end and an acoustic dampening device at the other. The transducer introduces a high frequency sound wave into the quartz medium, with sound velocity  $v_s$  and wavelength  $\lambda_s$ . The sound wave causes a sinusoidal perturbation of the density of the material, which in turn causes a change in its index of refraction. Figure 3.7 shows a simplified representation of the Bragg cell and the variation of the refraction index along the path of the acoustic wave.

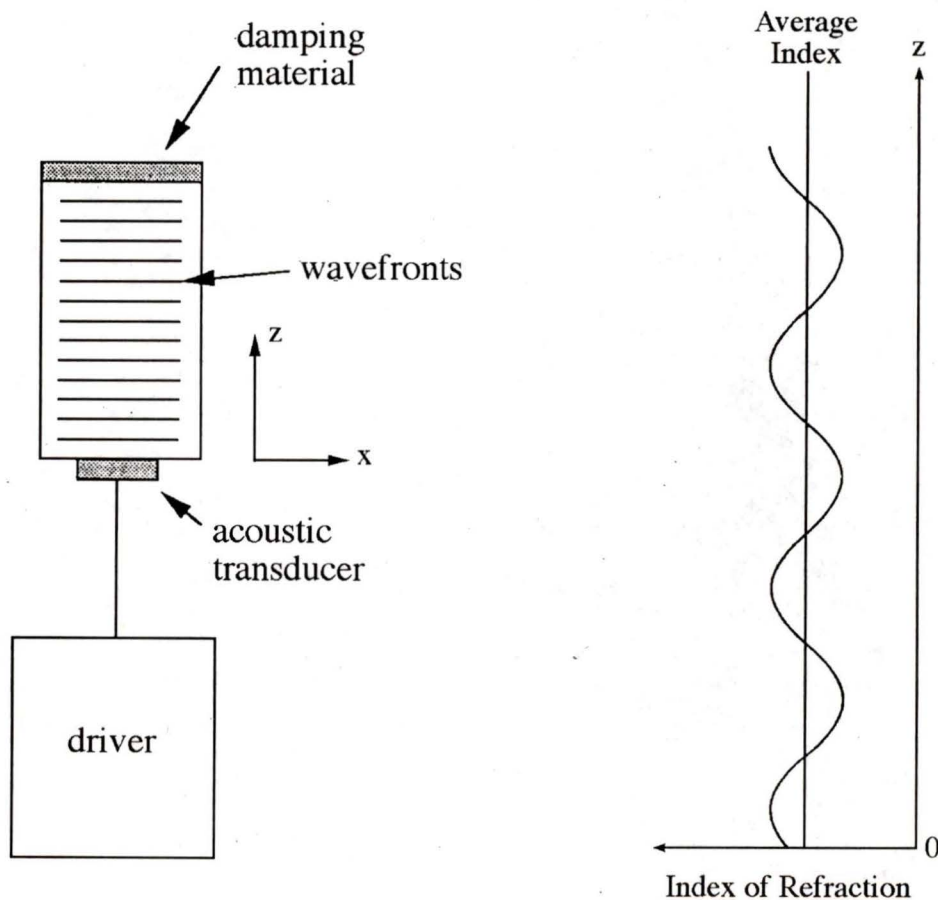


**Figure 3.7:** Bragg cell

The change in refractive index caused by the acoustic wave acts as a partially reflecting mirror, moving at velocity  $v_s$ . When an optical beam is incident upon the sound wave at an angle  $\theta_i$ , it is partially diffracted. The diffracted wave is spherical but will only effectively propagate along lines of uniform phase.

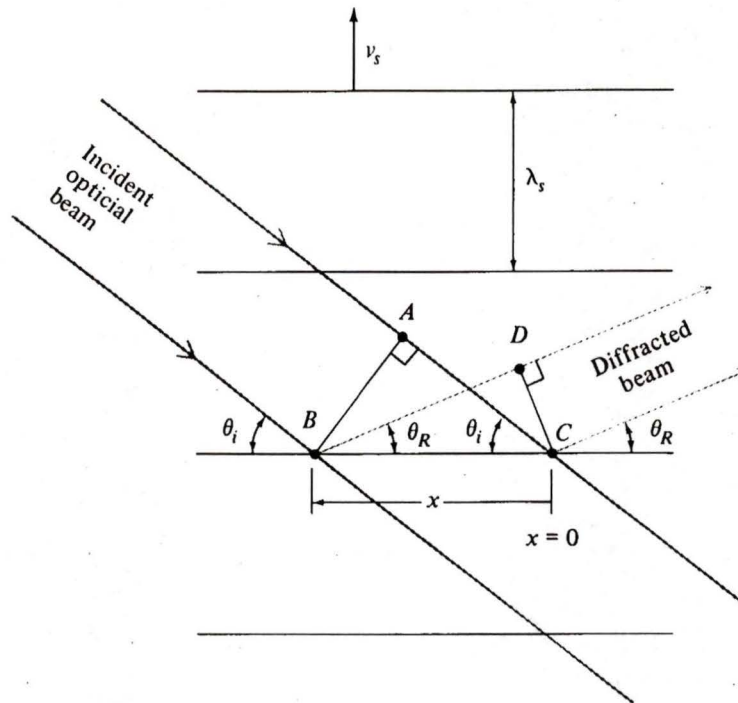


**Figure 3.8:** Diffraction of light by an acoustic wave

A necessary condition for diffraction in a given direction is that all the points on the mirror contribute in phase to the diffraction along this direction. Considering the diffraction from two points, such as C and B in figure 3.8, it is then necessary that the optical path difference  $AC - BD$  be some multiple of the optical wavelength  $\lambda/n$  for diffraction along  $\theta_r$  to occur. This condition takes the form

$$x (\cos \theta_i - \cos \theta_r) = \frac{m\lambda}{n} \quad (3.9)$$

where:  $m = 0, \pm 1, \pm 2 \dots$   
 $n$  = refractive index of quartz  
 $\theta_i$  = angle of incidence  
 $\theta_r$  = refraction angle

The only way in which (3.9) can be satisfied simultaneously for all points  $x$  along a given reflector is if  $m=0$ , from which it follows that

$$\theta_i = \theta_r = \theta \quad (3.10)$$

In addition to the requirement that the different parts of a given optical wave front interfere constructively, we require that the diffraction from any two acoustic wave fronts add up in phase along the direction of the reflected beam. The path difference  $AO + OB$  shown in figure 3.9 of a given optical wave front, resulting from reflection from two equivalent acoustic wave fronts, must thus be equal to the optical wavelength  $\lambda$ .

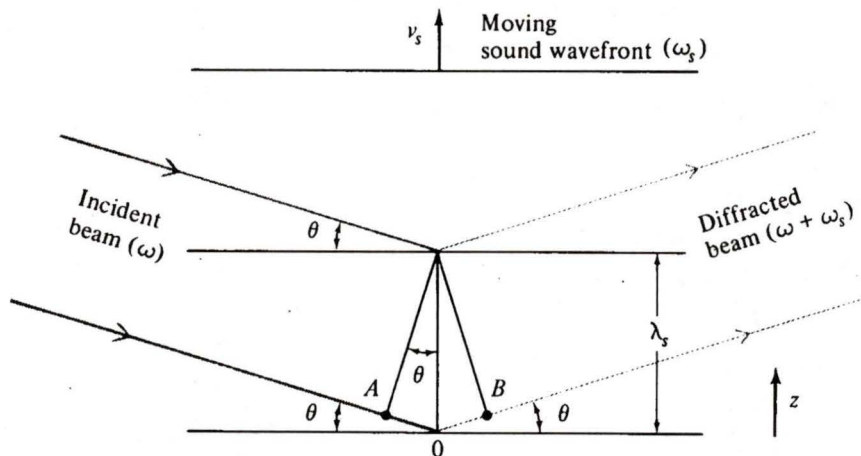


**Figure 3.9:** Light reflection from two equivalent acoustic wavefronts

This condition can be written as

$$2\lambda_s \sin\theta = \frac{\lambda}{n} \quad (3.11)$$

The diffraction of light that satisfies (3.11) is known as Bragg diffraction.

The diffracted optical beam will undergo a shift in frequency due to the Doppler effect. The Doppler effect states that any electro-magnetic wave reflecting from a moving object

is frequency shifted by an amount  $\Delta\omega$

$$\Delta\omega = 2\omega \cdot \frac{v}{c/n} \quad (3.12)$$

where:  $\omega$  = optical frequency

$v$  = velocity of the object, in direction parallel to wave propagation

From figure 3.9 we have  $v=v_s \sin\theta$ , and thus

$$\Delta\omega = 2\omega \cdot \frac{v_s \sin\theta}{c/n} \quad (3.13)$$

Using (3.11) for  $\sin\theta$  we obtain

$$\Delta\omega = \frac{2\pi v_s}{\lambda_s} = \omega_s \quad (3.14)$$

The frequency of the reflected optical beam, therefore, is  $\omega + \omega_s$ , where  $\omega_s$  is as in (3.14). The diffracted beam is upshifted by a frequency  $\omega_s$ . In the design of a heterodyne interferometer, an ultrasonic wave passes through the Bragg cell at a frequency of 70 MHz. The interference of the reference and signal beams produces a 70 MHz beat signal at the photodiode.

### 3.3 System Design

There have been several proposed designs of heterodyne interferometers, two of which were considered for use in this project. Both methods utilize the basic principle of creating a frequency difference between the reference and target beams, but differ in the frequency shifting technique. Introducing a frequency shift between the reference and target beams can be accomplished using several methods, with varying success in maintaining coherency and amplitude. The methods discussed here are the Zeeman laser and Bragg cell.

### 3.3.1 Zeeman Laser Heterodyne Interferometer

A Zeeman laser source simultaneously emits two frequencies which are inversely circularly polarized relative to each other. The two beams can be physically separated using a  $\lambda/4$  wave plate and a polarizing beam splitter, as shown in figure 3.10.

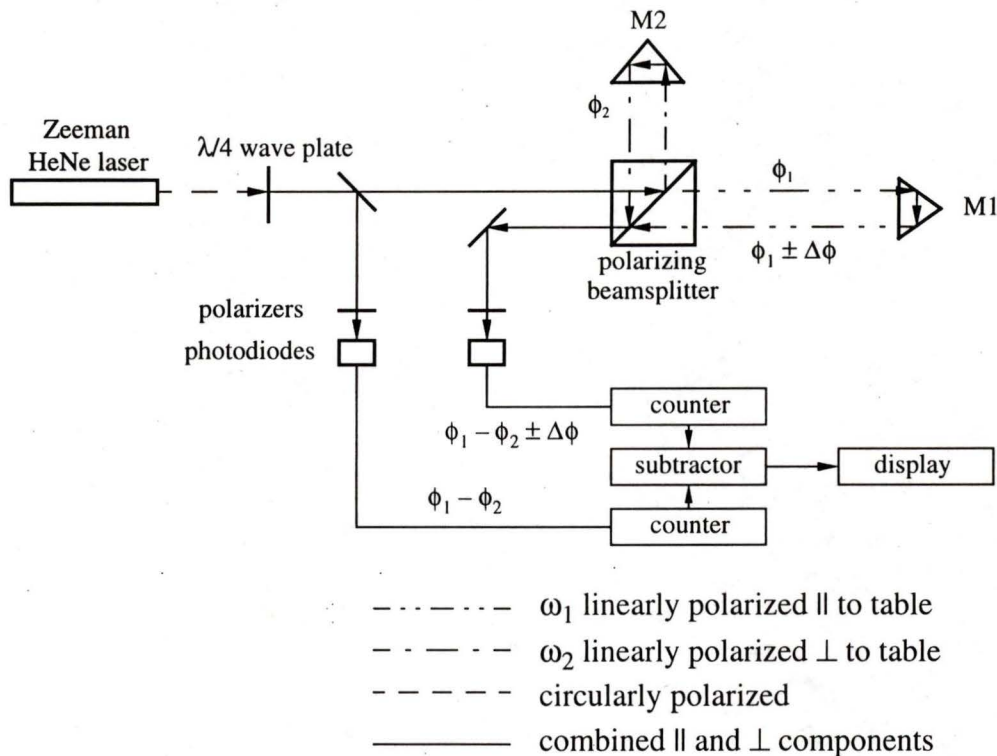


**Figure 3.10:** Zeeman laser heterodyne interferometer

After passing through the  $\lambda/4$  wave plate, the two frequency components become linearly polarized in orthogonal planes. The phase angle between these two components is unknown and can change over time. For this reason, the phase angle between these two polarization states must be measured. This is accomplished by partially reflecting the beam using a 50/50 beamsplitter and passing the beam through a polarizer set at a polarization angle 45 degrees to both the S and P planes. This polarizes both frequency components into the same plane, causing a beat signal to form. The phase of this beat signal,  $\phi = \phi_1 - \phi_2$ , is sampled using a photodiode and then sent to a counter.

The transmitted beam continues to the polarizing beam splitter, where the S component

reflects and becomes the reference beam. The P component passes through the polarizing beam splitter and bounces off the target. When the two beams recombine at the second photodiode, the phase angle of the beat signal,  $\phi = \phi_1 - \phi_2 + \Delta\phi$ , now contains the initial phase angle plus the change in phase. The second beat signal is also sent to a counter. Subtraction of the two count values in hardware provides the target displacement.

Although Zeeman laser heterodyne interferometers are desirable because of their inherent simplicity and compactness of the design, they are limited to approximately 2.5 nm in resolution because of imperfections in the  $\lambda/4$  wave plate and polarizing beam splitter, leading to imperfect separation of the optical frequencies [37].

For the above reasons, the Zeeman laser method was not used. Instead, the optics are based on a Bragg cell frequency shifting device.

### 3.3.2 Bragg Cell Heterodyne Interferometer

A heterodyne interferometer utilizing a Bragg frequency shifting technique was chosen because of the Bragg cell's ability to maintain beam coherency and wave front quality. The system design of a Bragg cell heterodyne interferometer is shown in figure 3.11.

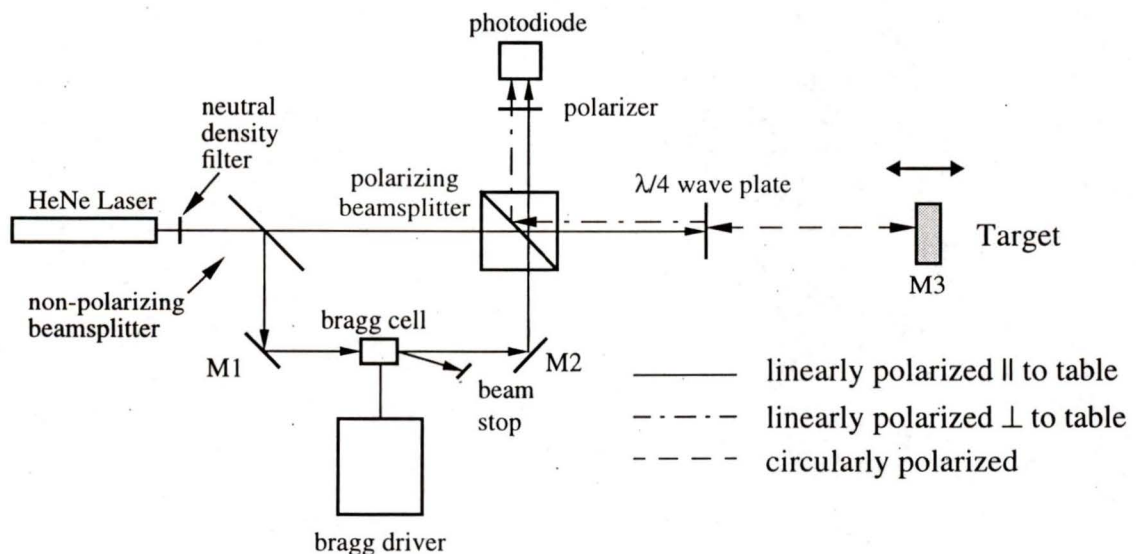


**Figure 3.11:** Bragg cell heterodyne interferometer

---

A 5 mW Helium-Neon laser beam, linearly polarized in the plane parallel to the optical table is used as a light source. The intensity of the laser is first attenuated by 95% using a neutral density filter, thereby preventing saturation of the photodiode. The beam is then split using a 50/50 non-polarizing beam splitter, with the reflected beam becoming the reference. The reference beam reflects off M1 and passes through the Bragg cell where it is shifted in frequency by 70 MHz. The first order, frequency shifted beam is directed through the polarizing beam splitter and into the photodiode. The signal beam passes through both beam splitters, through the  $\lambda/4$  wave plate, and reflects off the moving mirror M3. When the beam passes through the  $\lambda/4$  wave plate the second time, its polarization state is shifted by 90 degrees with respect to the incident beam (see section 3.2.2). The polarizing beam splitter has approximately 97% reflectivity to this polarization state (see section 3.2.3), forcing the signal beam to reflect into the photodiode. Using the  $\lambda/4$  wave plate and polarizing beam splitter in this manner isolates the laser cavity from feedback. Excessive feedback into the optical cavity can cause loss of coherency.

The reference and signal beams are re-combined after the polarizing beam splitter, but do not interfere to produce a beat signal because they are in orthogonal polarization states. The polarizer shifts the polarization of each component to a plane 45 degrees from both the P and S states. The beat signal is passed from the photodiode to a high speed amplifier which converts the current signal to a voltage signal. The amplified signal is then passed to the phase demodulation circuit, described in the following chapter.

---

## 4.0 Phase Demodulation

After establishing a beat signal, the phase of the signal must be measured accurately in order to estimate displacement. An analog radio frequency (RF) phase demodulation circuit was designed to input the 70 MHz beat signal and a 70 MHz reference signal, and to output two DC voltages proportional to the sine and cosine of the phase angle. Because the output is in quadrature, both displacement and direction can be measured. The output from the circuit is sampled using both a quadrature decoder board (for high speed, low resolution) and an A/D board (for low speed, high resolution). A weighting algorithm is used to compensate for the varying sensitivity of the two quadrature signals.

### 4.1 Phase Demodulation Circuitry

The phase demodulation circuit inputs two 70 MHz signals, the heterodyne interferometer beat signal and a reference, and outputs the sine and cosine of the phase angle between the two. The circuit is analog, built with high performance components and therefore has a very high bandwidth. The bandwidth was not measured due to a lack of a satisfactory phase modulator, but it is estimated to be at least 10 MHz based on bandwidth specifications of the circuitry components.

The phase demodulation circuit is divided into two components: RF and low frequency circuitry. These components are described in sections 4.1.1 and 4.1.2.

### 4.1.1 RF Circuitry

The function of the RF portion of the circuit is to filter the beat signal and stabilize the amplitude before measuring the phase using a Mini-Circuits phase detector. The RF component of the circuit is shown in figure 4.1.

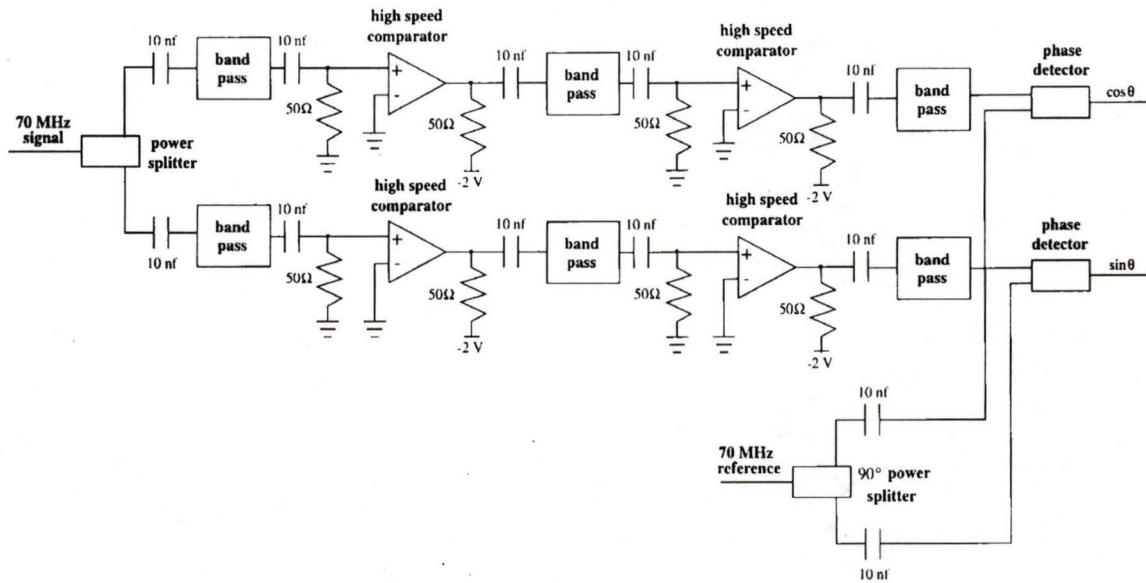


**Figure 4.1:** RF phase demodulator circuitry

The beat signal is split using a Mini-Circuits RF power splitter and then immediately high pass filtered using a 10 nF capacitor, followed by a 70 MHz band pass filter. The band pass filter helps to remove RF noise as well as wide band noise from the amplifier. The signal is then squared using an Analog Devices high speed comparator. This component provides a stable amplitude of  $\pm 500$  mV. Fluctuations of up to 20% in the signal amplitude are not reflected in the comparator output. The signal is then band pass filtered, amplified, and band pass filtered again before being sent to the Mini-Circuits phase detector.

The 70 MHz reference signal is generated by the Bragg cell driver and does not require filtering or amplification. The signal is passed through a 90 degree power splitter and then into the phase detector.

The Mini-Circuits phase detector takes two RF signals as input and outputs a DC voltage proportional to the cosine of the phase angle between the two inputs. Comparing the beat signal to the reference signal and the 90 degree phase shifted reference signal produces the sine and cosine of the phase angle. The output is now in quadrature and can be used to measure both displacement and direction.

### 4.1.2 Low Frequency Circuitry

The output from the Mini-Circuits phase detector is at a low amplitude, with a low signal to noise ratio, and requires signal processing (see figure 5.6). The low frequency portion of the phase demodulator is shown in figure 4.2.

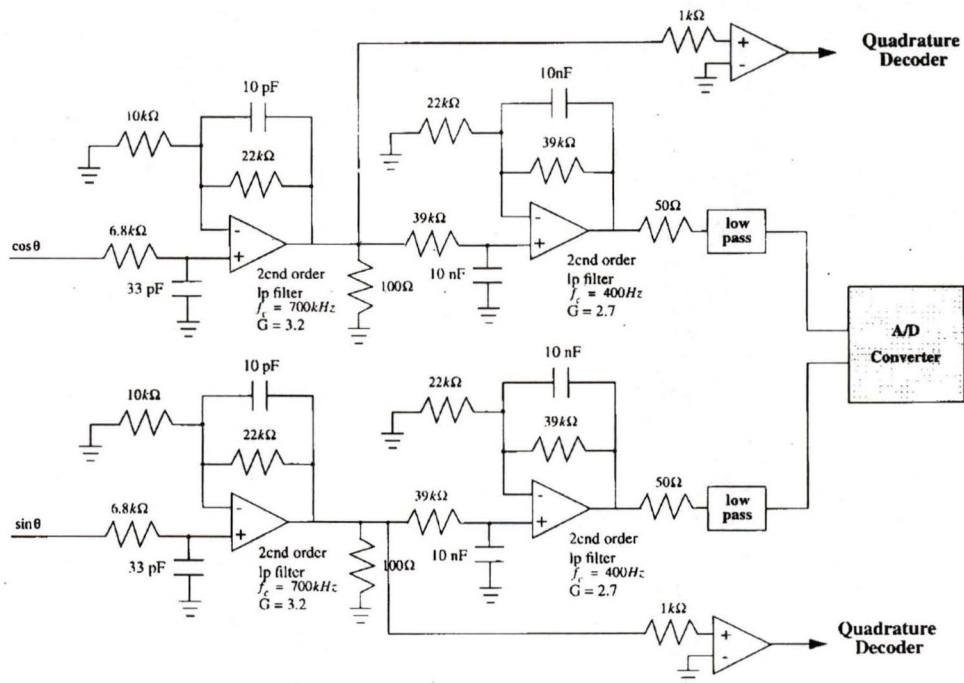


**Figure 4.2:** Low frequency phase demodulator circuitry

The cosine and sine of the phase angle are first filtered using a second order filter with  $f_c = 700$  kHz. This filter removes RF leakage from the phase detector, but still allows enough bandwidth to detect high speeds.

$$v = f \cdot \frac{\lambda}{2} \quad (4.1)$$

where:  $v$  = speed of target  
 $f$  = frequency output from phase detector  
 $\lambda$  = wavelength of laser light = 632 nm

The corner frequency of the first low pass filter,  $f_c = 700$  kHz, corresponds to a speed of 22 cm/s.

The filtered signal is sent to a comparator and used as input into the high speed ( $f_s = 10$  MHz) quadrature decoder board. The cosine and sine signals are then sent to anti-aliasing filters with  $f_c = 400$  Hz; this cut off frequency corresponds to approximately 4/10 of the National Instruments A/D board sample frequency. The low frequency component of sine and cosine are sampled with the A/D board and used to interpolate to higher resolution.

### 4.1.3 Circuit Design Considerations

The first component in any RF circuit prototype is a low impedance ground plane. Differences in impedance to different grounding points on a bread board can cause offsets in the zero point, otherwise known as ground loops. The ground plane has been especially designed to have low impedance for frequencies up into the GHz range. The ground plane serves a second function as a partial shield against RF broadcasting.

Impedances in normal wiring can become quite sizable at high frequencies due to parasitic inductances, and it is therefore imperative to run all grounds to a low impedance ground plane, preferably soldering the IC connections directly to the plane. Impedance must be kept to a minimum when connecting circuit components in order to reduce excessive impedance mismatching and reflection. This involves keeping the circuit layout compact, using short connection wires, keeping circuit component leads short, and never using plug-in IC connectors.

---

## 4.2 Algorithm for Displacement Measurement

The conversion of the output voltages from the demodulator circuit into a displacement measurement is done in software. The phase demodulation circuitry outputs two signals to the computer: a quadrature square wave to the quadrature decoder board to provide high speed/low resolution, and an analog signal to the A/D board to provide a low speed/high resolution measurement. The signals are then converted to a phase angle, and from the phase angle the displacement can be calculated. The overall process is illustrated via a block diagram in figure 4.3.

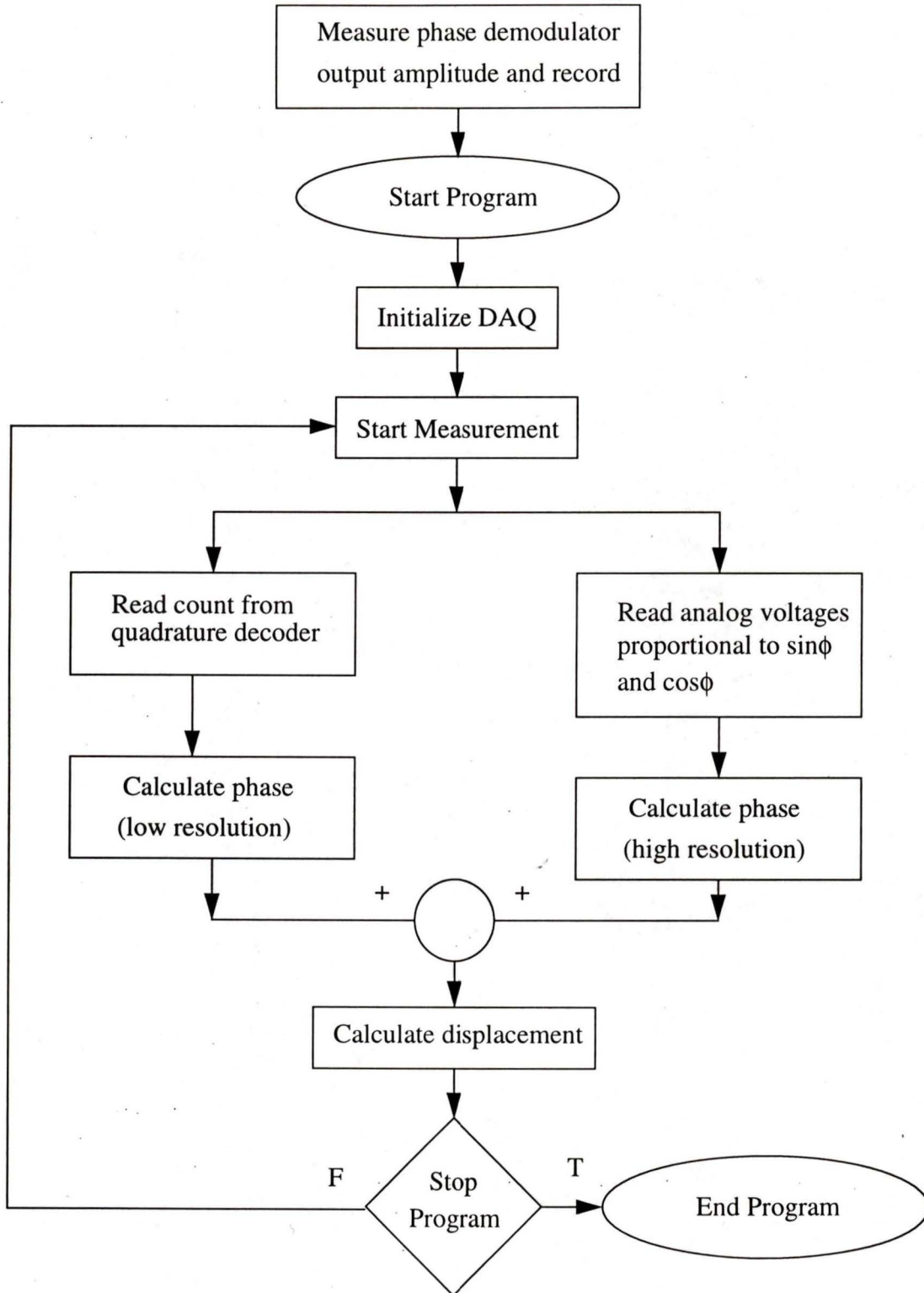


**Figure 4.3:** Displacement measurement algorithm flow diagram

---

The phase demodulator amplitude adjustment, phase measurement, and displacement measurement is explained below using text and pseudo-code.

### 4.2.1 Amplitude Adjustment

The amplitude of the phase demodulator output is typically  $\pm 3.5$  V, but can fluctuate as much as 5% over the span of several days. In addition the signal will also have an offset of approximately 50 mV, also slightly variable over time. A program has been written to measure the amplitude and offset of the phase demodulator output and write these values to a file. The software described in the following sections reads these values from the file and automatically compensates.

It is necessary to measure the output amplitude in this way only when the alignment of laser beam has been changed, which will change the amplitude of the beat signal by 5 to 10%. It is prudent however to run the measurement program at the beginning of any test run.

### 4.2.2 Phase Measurement

To find the phase angle, the voltage is scaled by the output amplitude and inverted. If the output becomes larger than the amplitude due to noise or some other anomaly, the scaled value is automatically set to  $\pm 1$ . This prevents the program from stalling due to an “out of range” return.

Inversion of the sine and cosine signals produces a total of four angles, two for each inversion. The correct angle is the one common to both channels. The angles found for the sine and cosine voltages generally differ by a small amount due to noise, especially in areas of low sensitivity. In order to estimate the true phase angle, the angles must be weighted according to the signal sensitivity.

The algorithm for computing the phase angle  $\phi$  between the inputs for any pair of demodulator output voltages is

$$\phi = \frac{[(\phi_1 \times W_1) + (\phi_2 \times W_2)]}{W_1 + W_2} \quad (4.2)$$

where:  $\phi_1$  = phase angle found from sine voltage  
 $W_1$  = weighting of  $\phi_1$   
 $\phi_2$  = phase angle found from cosine voltage  
 $W_2$  = weighting of  $\phi_2$

The weighting of the phase angles is based on the slope of the curve at the measured phase angle. This places more weight on areas with high sensitivity (eg. sine at 180 degrees) and less weight on areas with low sensitivity (eg. cosine at 0 degrees). The procedure for estimating phase angle is illustrated in the following flow diagram.

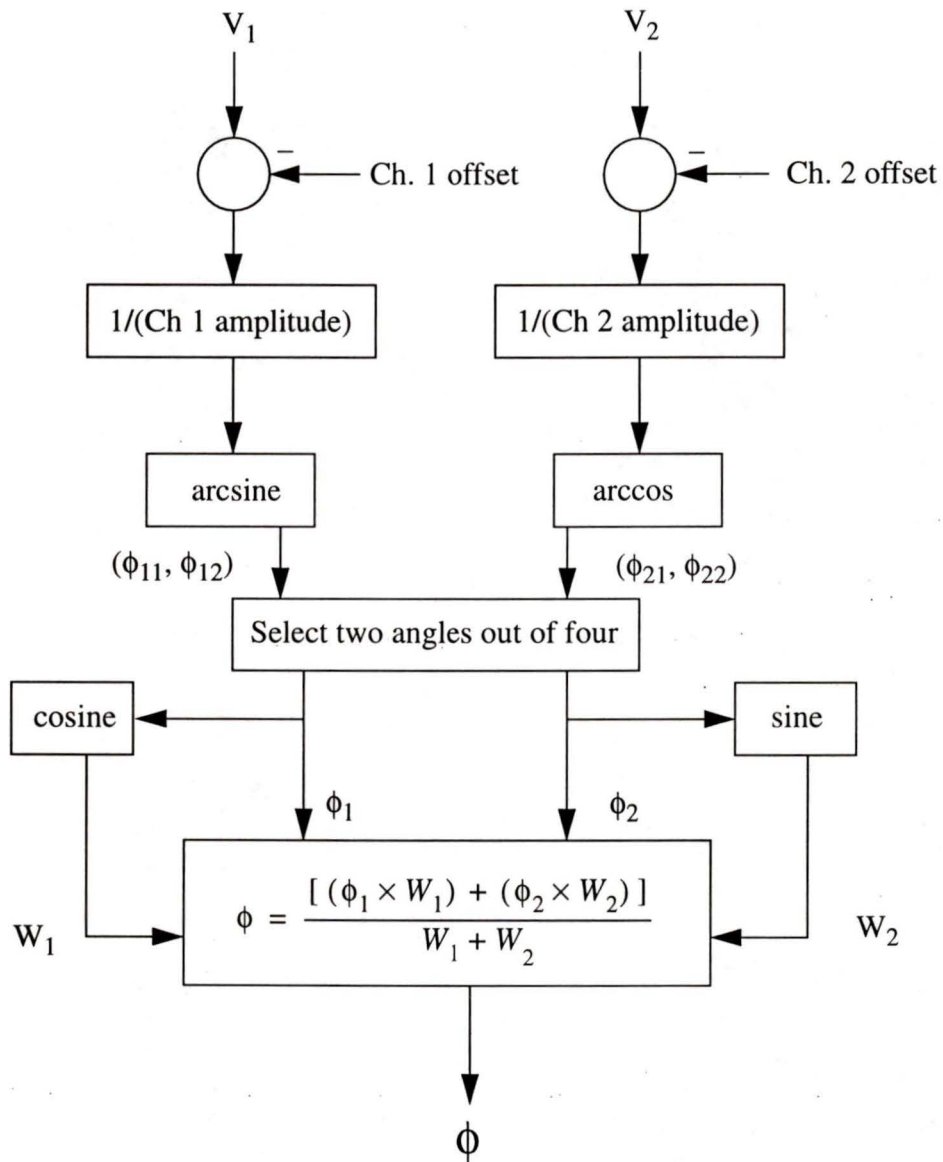


**Figure 4.4:** Phase measurement flow diagram

### 4.2.3 Displacement Measurement

Now that the phase angle  $\phi$  has been estimated, the displacement can also be estimated. At this point in the program the starting point (start), and the quadrature count (X) have been determined. The algorithm is shown in figure 4.5.

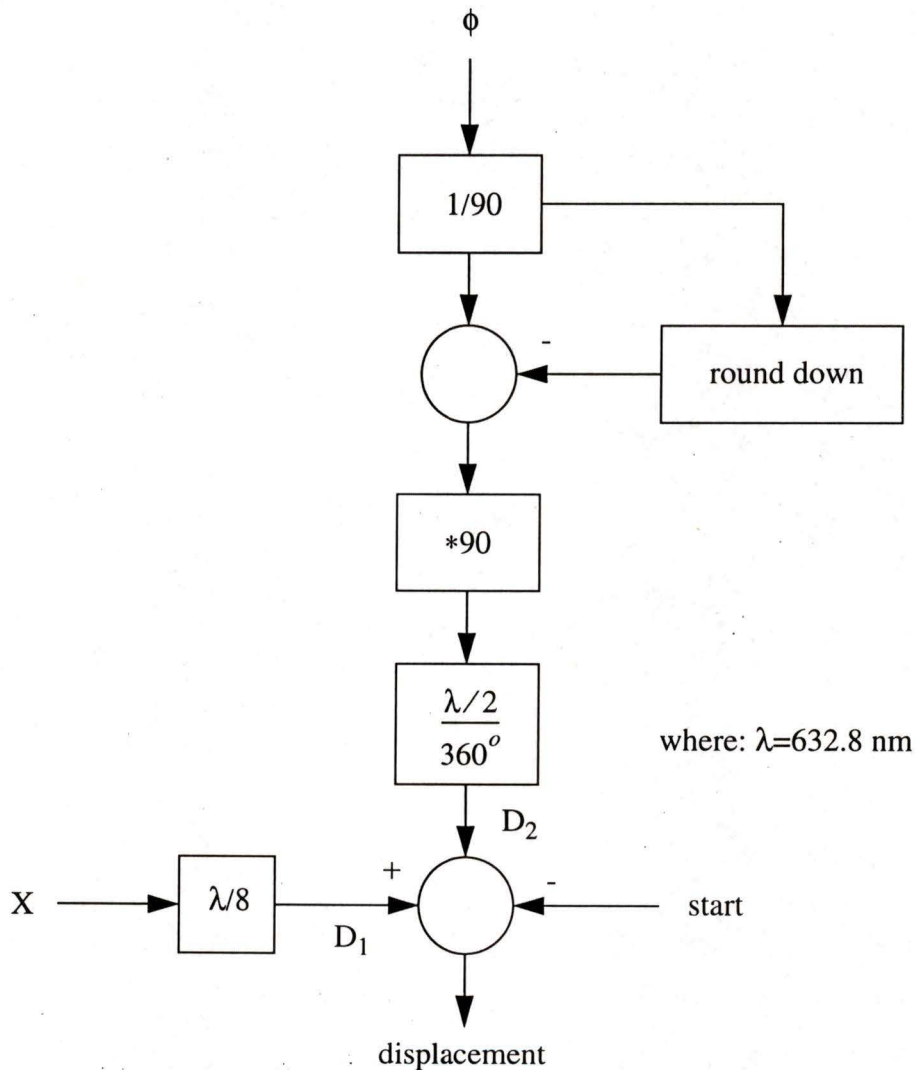


**Figure 4.5:** Displacement measurement flow diagram

The quadrature encoder counts every 90 degrees, and given that 360 degrees corresponds to  $\lambda/2$ , the encoder has a resolution of  $\lambda/8$ . The higher resolution displacement  $D_2$  is calculated using the phase angle  $\phi$ . Because the encoder count X includes phase angle incre-

---

ments of 90 degrees,  $n \cdot 90$  is subtracted from the phase angle, where  $n$  is the number of whole number multiples of 90 degrees that can be taken from  $\phi$  (eg.  $\phi=290 \rightarrow \phi=20$ ). Finally, the displacement  $D_1$  and  $D_2$  are added, and the starting position is subtracted. This yields the final displacement measurement.

## **5.0 RF Noise**

The accuracy of the phase measurement is largely determined by the level of RF noise present in the phase demodulator circuit. As a result, it is crucial to maximize the signal to noise ratio of the beat signal. This chapter describes the many measures taken to remove RF noise from the phase demodulator circuit.

### **5.1 Beat Signal**

As described in section 4.1, phase demodulation is performed in hardware using the heterodyne interferometer beat signal and a reference signal. The 70 MHz beat signal output from the high frequency amplifier is both weak and noisy, making it exceptionally difficult to make accurate phase measurements. Figure 5.1 shows the actual output from the amplifier and the corresponding spectrum.

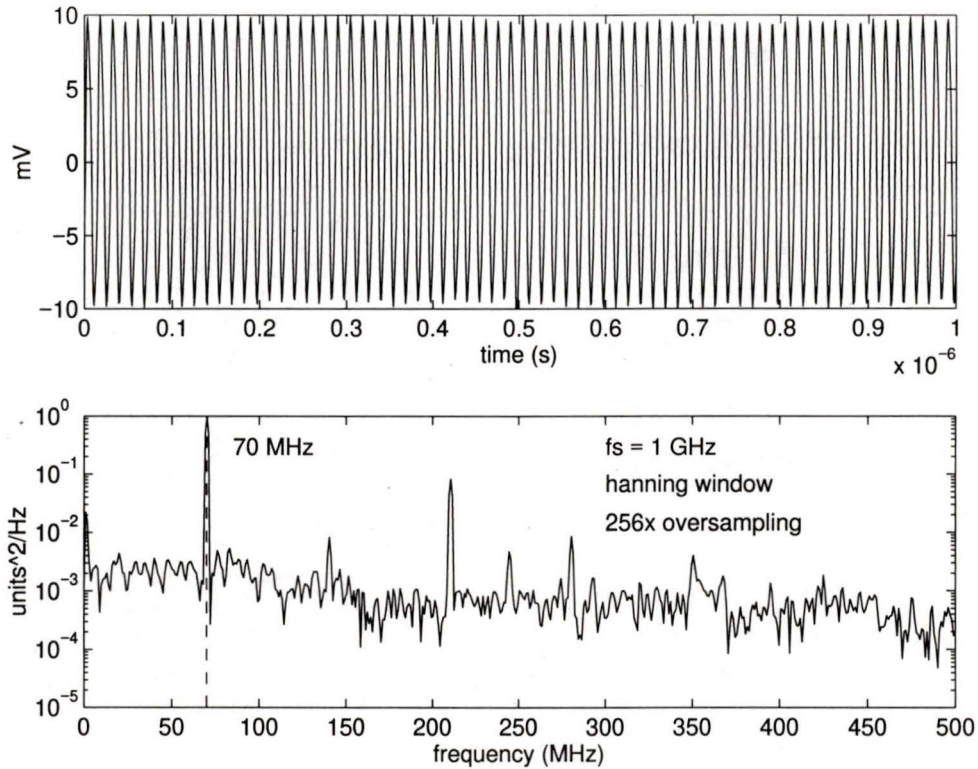


**Figure 5.1:** Heterodyne interferometer beat signal

The spectrum and time series indicate a significant RF noise contamination, with several high frequency components which can disrupt the phase measurement process. Phase measurement is further complicated by the fact that the amplitude of the beat signal varies with time. In order to make an accurate phase measurement, the beat signal must be thoroughly filtered and the amplitude must be stabilized.

## 5.2 Sources of RF Noise

The phase demodulator circuit must filter and/or block RF noise carried through broadcasting and physical connections to the circuit. Specifically, RF noise can be passed into the circuit through the signal and reference connections, power connections, connections to the computer data acquisition (DAQ) system, and noise generated by radio transmissions picked up and amplified at the inputs of the high speed comparators. The connections to the computer DAQ boards are particularly noisy due to the close proximity of the

switching power supply and high speed digital circuitry. RF noise of this nature can range anywhere from 10 MHz to hundreds of MHz.

### 5.3 RF Noise Reduction Techniques

Many noise reduction techniques are employed within the phase demodulator circuit to reduce high frequency noise. Physical connections, such as power leads or computer connections, have lower impedance for noise transmittance and are the primary source of noise. For this reason, all pathways into the circuit are carefully shielded.

All power connections are first passed through a 24  $\mu\text{H}$  hash RF choke - resonant at 25 MHz. This is followed by ferromagnetic beads, one bead having maximum impedance below 50 MHz, and the second between 40 MHz and 200 MHz. Any power connections to RF circuit components are tied to ground through mica capacitors. The power supply filtering circuitry is shown in figure 5.2.

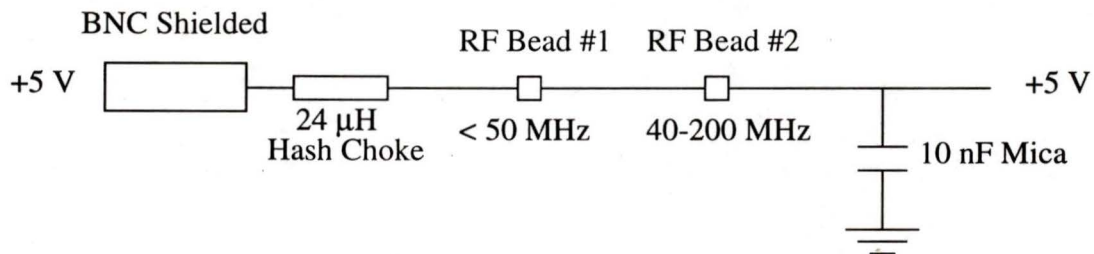


**Figure 5.2:** RF conductive shielding

On critical power supply connections (eg. high frequency comparators), a broadband card entry filter is used instead of the mica capacitor. The card entry filter employs a tantalum capacitor to remove high frequency components and a ceramic capacitor to remove low frequency components, in series with a 1 ohm resistor. The resistor reduces the Q of resonance and prevents the tantalum capacitor from burning out when passing very high frequency components. The card entry filter circuit and frequency response curves (figure 5.3) are taken from a paper by Walt Jung and John McDonald [38].

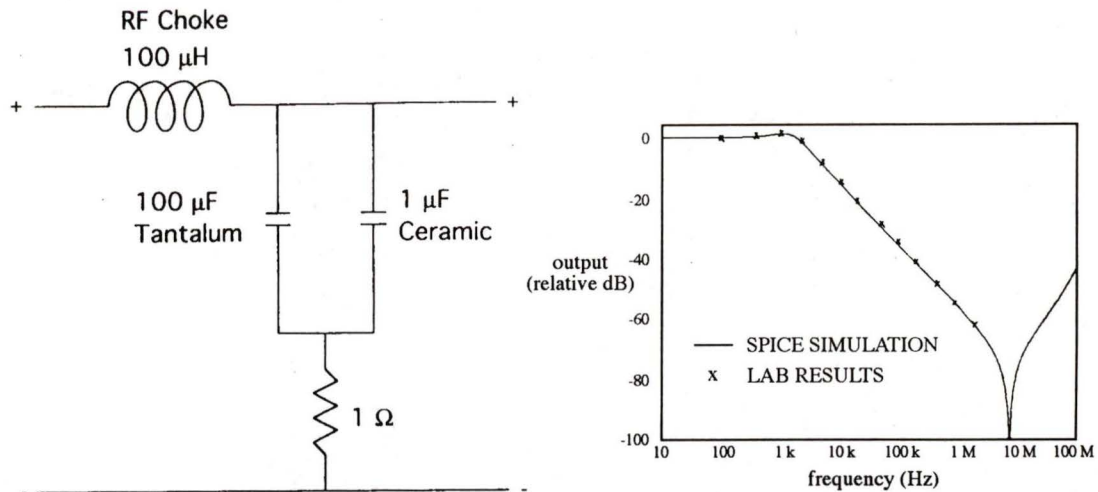


**Figure 5.3:** Card entry filter

In addition to the power shielding, special care must be taken when connecting the circuit to the computer DAQ system due to the excessive RF noise produced by the computer's switching power supply and digital electronics. Amphenol filter connectors are used to remove this noise source. These connectors are specifically designed for connection to computers, and have a low pass filter built into each conductor.

## 5.4 RF Shielding

Once conductive paths for RF noise have been eliminated, the circuit must be protected from radiative paths. This is accomplished using an aluminum alloy enclosure. This type of conductive enclosure is used to shield sensitive circuits from the effects of external RF fields. The shield box presents an impedance mismatch to the incident interference because the impedance of the shield is lower than the wave impedance of the incident field.

The effectiveness of the conductive shield depends on two things: the loss due to reflection of the incident wave, and the loss due to absorption of the transmitted wave within the

shielding material. These concepts are illustrated in figure 5.4.

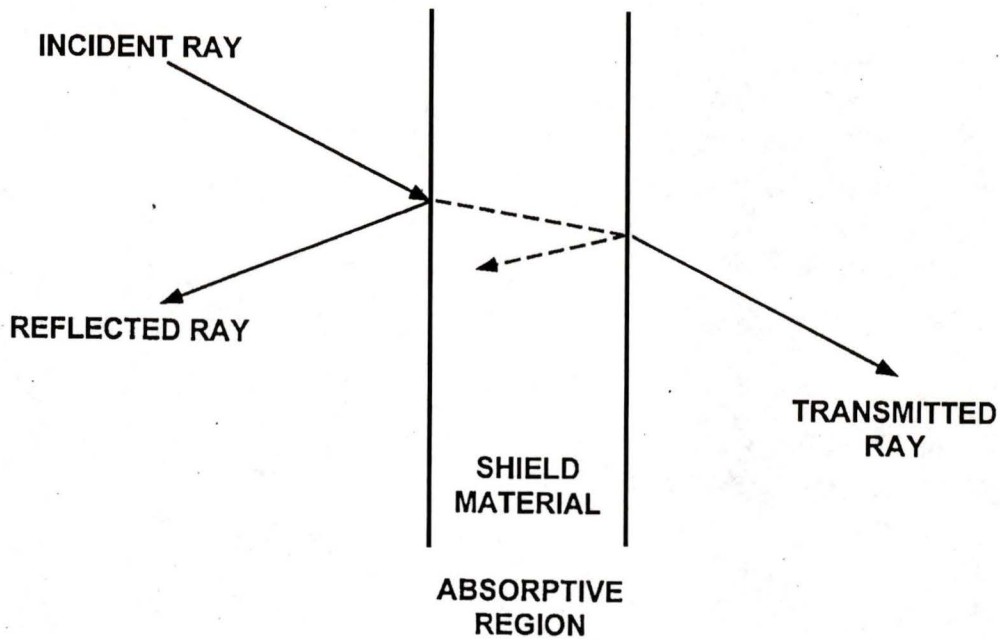


**Figure 5.4:** Reflection and absorption of RF shielding

Reflection loss at the interface between two media depends on the difference in the characteristic impedances of the two media. For electric fields, reflection loss depends on the frequency of the interference and the shielding material. This loss in the far field ( $r > \lambda/2\pi$ ) can be expressed in dB, and is given by [39]

$$R(dB) = 168 + 10 \log \left[ \frac{\sigma_r}{\mu_r f} \right] \quad (5.1)$$

where:  $\sigma_r$  = relative conductivity of the shielding material (Siemens/m)  
 $\mu_r$  = relative permeability of the shielding material (Henries/m)  
 $f$  = frequency of the interference (Hz)  
 $r$  = distance from source of the interference (m)

Wave attenuation due to absorption is shown in the following equation [39]

$$A (dB) = 3.34t \sqrt{\sigma_r \mu_r f} \quad (5.2)$$

where:  $t$  = thickness of the shield material (in)

Reflection loss for plane waves in the far field decreases with increasing frequency because the shield impedance  $Z_s$  increases with frequency. The shield impedance for aluminum is given by [39]

$$|Z_s| = 4.71 \times 10^{-7} \sqrt{f} \quad (5.3)$$

Absorption loss, on the other hand, increases with frequency. For electric fields and plane waves, the primary shielding mechanism is reflection loss, and at high frequencies, the mechanism is absorption loss. For RF interference, high conductivity materials, such as copper or aluminum, provide adequate shielding [39].

## 5.5 Amplitude Stabilization

Constant amplitude is essential in any phase measurement system. In the case of the phase demodulator circuit, the output of the Mini-Circuits phase demodulator circuit component is proportional to both phase and the amplitude of the input signals. For this reason, it is crucial to eliminate fluctuations in the beat signal amplitude. High speed comparators are used to square the signal and provide a constant amplitude of  $\pm 500$  mV. Amplitude fluctuations of up to 20 percent will not be reflected in the comparator output. However, because amplitude fluctuations are sometimes greater than 20 percent, a two stage amplification has been employed (see figure 4.1).

## 5.6 RF Filtering

Any RF noise that remains in beat signal after employing all of the RF reduction techniques described in section 5.3 must be filtered. The 70 MHz beat signal, after filtering and amplification, is shown in figure 5.5. The spectrum, when compared to the original signal shown in figure 5.1, indicates that the noise components at 140 and 210 MHz have been reduced by 20 dB. This is a modest attenuation, but sufficient to reduce non-linearity error in the mini-circuit phase detector output to a sub-nanometer scale.

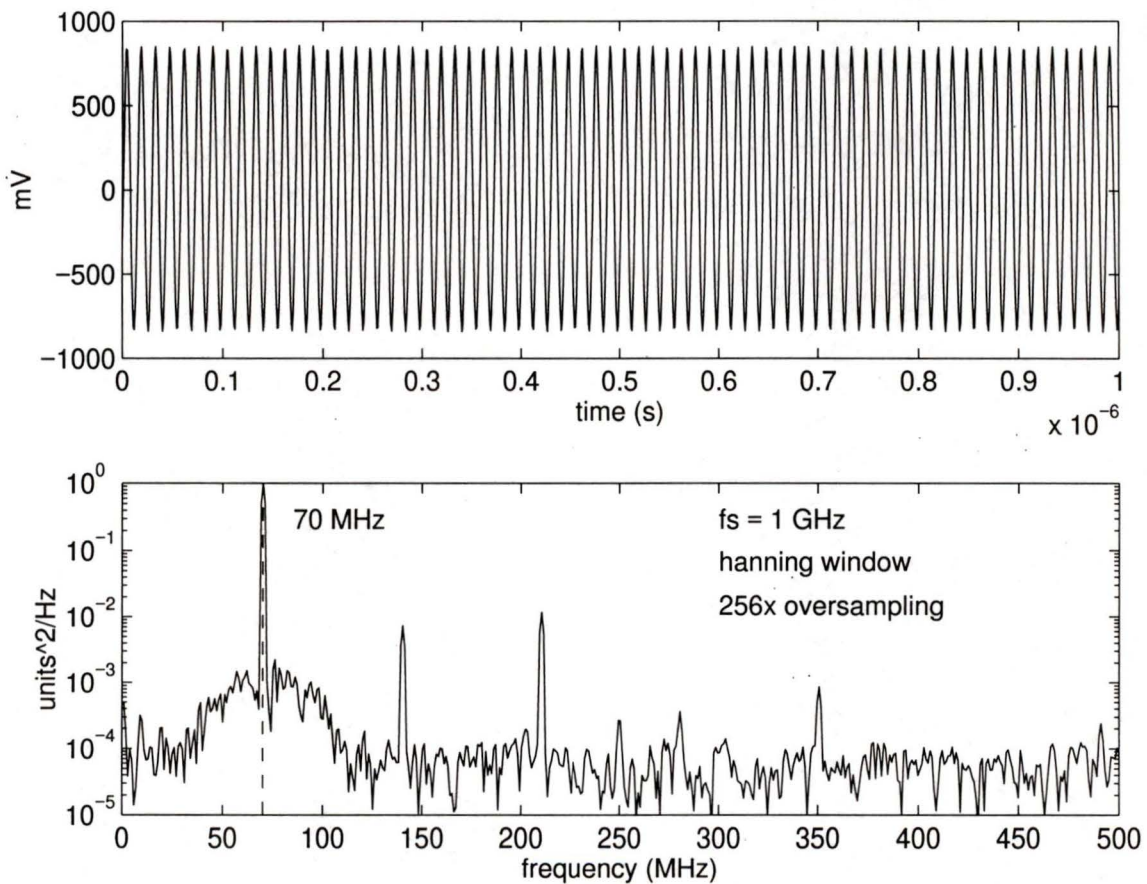


**Figure 5.5:** Filtered beat signal

Further filtering is required to eliminate RF noise in the low frequency circuitry. The Mini-Circuits phase detector outputs a DC signal proportional to the sine of the phase angle. The component, however, does not completely isolate the low frequency circuitry from the 70 MHz input signals and carries frequency components at 70 MHz and several higher

harmonics. Figure 5.6 shows the AC component of the phase demodulator output and spectrum.

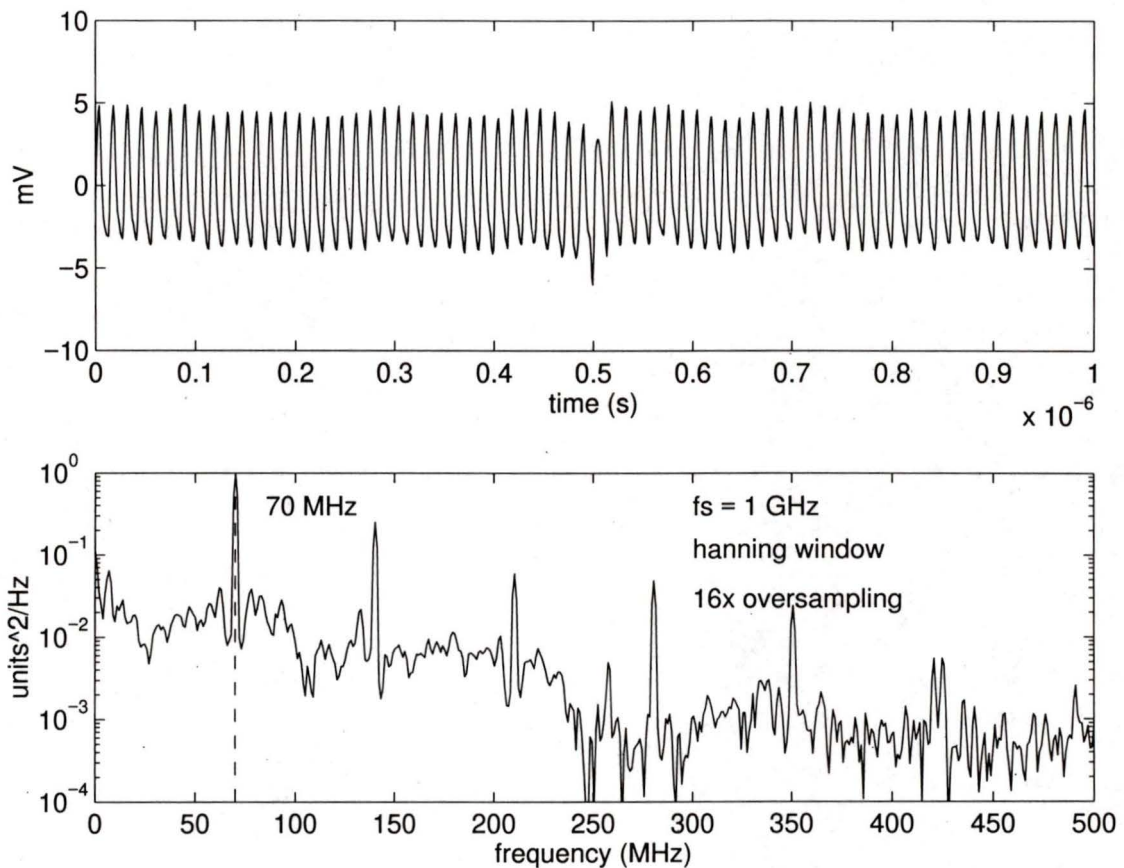


**Figure 5.6:** Phase detector RF output

The output from the Mini-Circuits phase detector must be filtered before it is squared and sent to the quadrature decoder. The center frequency of the second order low pass filter is set at 700 kHz. This ensures that no aliasing occurs in the encoder measurements, and still allows enough bandwidth for speeds of up to 22 cm/s to be detected (see equation (4.1) on page 44). The spectrum after the first filter stage is shown in figure 5.7.

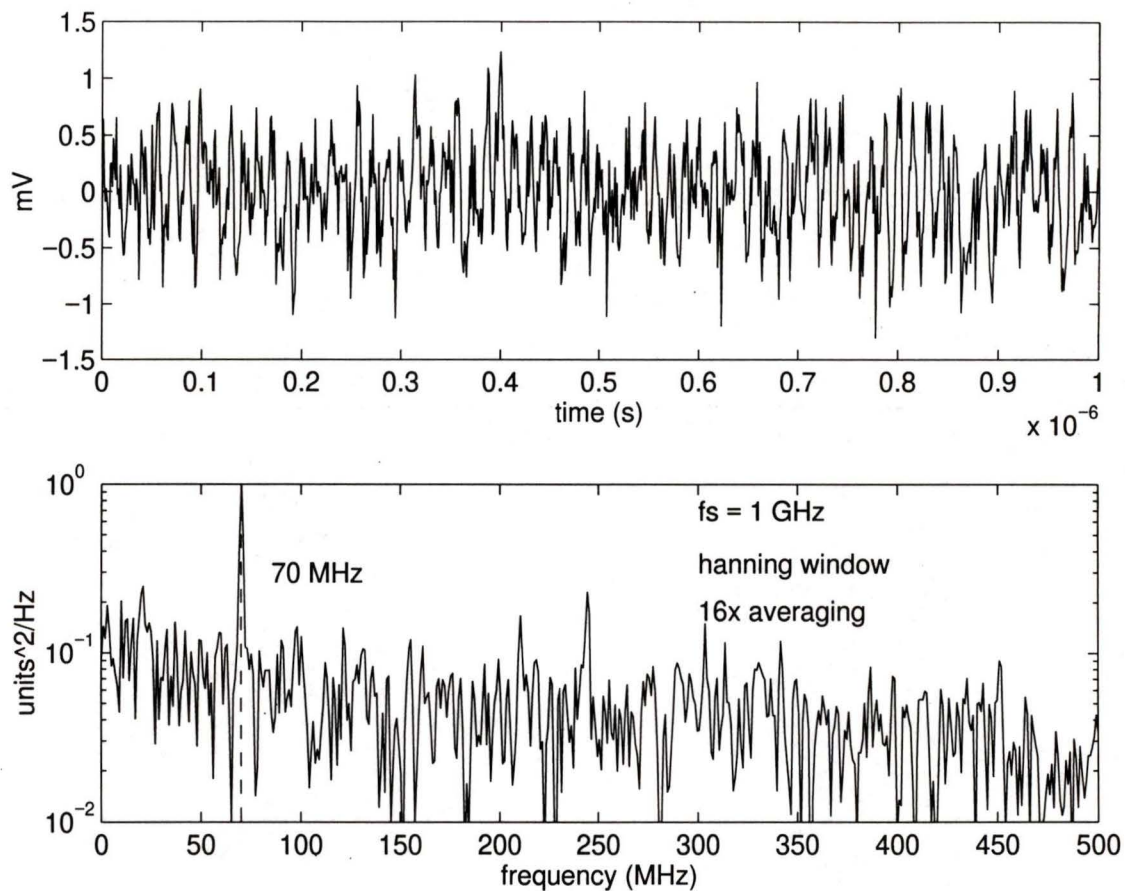


**Figure 5.7:** *Spectrum of phase detector output after first filter stage*

The RF components are still present due to parasitic inductances in the capacitors and wiring, but have been attenuated by approximately 40 dB.

The only way of further reducing RF noise levels in the phase demodulator circuit is the use of a printed circuit board. This will ensure a compact design with low impedance connections between components. In general, printed circuit boards are far more durable and reliable. It is only now, after the prototype stage of the circuit design, that this becomes an option.

## 6.0 Displacement Errors

There are numerous sources of error which affect any nanometer scale displacement measurement. Displacement errors can be categorized by their frequency: low, medium, and wide band noise sources. Estimates of noise sources are summarized in table 6.1.

**Table 6.1: Sources of displacement errors**

Source	Displacement
<b>Low frequency noise sources (&lt;25 Hz)</b>	
Cumulative (expected values) <sup>a</sup>	
Laser wavelength drift <sup>b</sup>	1 ppm/K
Refractive index of air change <sup>c</sup>	
Temperature	1 ppm/K
Pressure	0.003 ppm/Pa
Humidity	0.01 ppm/%change
Non-cumulative (expected values)	
Optical table and mounts thermal expansion <sup>d</sup>	100 nm/K
Building vibration	varies
<b>Medium frequency noise sources (&gt;25 Hz)</b>	
Acoustic and other mechanical vibrations	varies
<b>Wide band noise sources</b>	
Optical shot noise	0.01 pm/ $\sqrt{\text{Hz}}$

<sup>a</sup>1 ppm = 10 nm over 10 mm measurement range

<sup>b</sup>Data from the manufacturer

<sup>c</sup>Data taken from Estler [40]

<sup>d</sup>Data taken from Charette [37]

## 6.1 Low Frequency Noise

Noise falling below 25 Hz is considered low frequency noise. As shown in table 6.1, low frequency noise sources are further divided into cumulative and non-cumulative. These two types of error are described in sections 6.1.1 and 6.1.2.

### 6.1.1 Cumulative Error

Cumulative errors occur only when the target moves from the balanced position. The interferometer is balanced when the optical path lengths of the signal and reference beams are exactly equal. This means that a phase change in the signal and reference beams due to changes in laser wavelength are equal and opposite, and will cancel.

Cumulative errors are typically measured in absolute change of the refractive index. A change in 1 part per million (ppm) of the refractive index corresponds to a 10 nm displacement error over a range of 10 mm. This is shown below, assuming a laser wavelength of 632.8 nm at  $n=1$

$$error = \left( \frac{PD}{\lambda} - \frac{PD}{\lambda^*} \right) \cdot \lambda \quad (6.1)$$

$$error = \left( \frac{10mm}{\lambda} - \frac{10mm}{\lambda / (1 + 1 \times 10^{-6})} \right) \cdot \lambda = 10nm \quad (6.2)$$

where: PD = path length difference between the signal and reference beams

$\lambda^*$  = wavelength after 1 ppm change in refractive index

---

The wavelength of the laser in air is a function of the refractive index. Changes in refractive index occur due to fluctuations in the environmental conditions: temperature, pressure, and humidity. See section 6.5 for a more detailed description of the relationship between refractive index and ambient parameters.

The laser wavelength can also shift due to instabilities in the laser output. The laser output will drift slightly due to self heating of the laser cavity from the current flowing through the laser medium and changes in room temperature. The wavelength of the laser is a function of the length of the laser cavity. As the cavity heats, there is expansion, and the wavelength changes slightly. For convenience, error due to laser wavelength drift is also measured in ppm/K. This effect contributes 1 ppm/K, comparable to the effect of temperature on the refractive index. Note that laser wavelength drift can be virtually eliminated by using a stabilized laser, but at considerable expense.

In practice, it is very difficult to perfectly balance the interferometer. The path lengths can only be gauged by eye, leading to an uncertainty of at least 1 mm.

### **6.1.2 Non-cumulative Error**

Non-cumulative noise sources affect the displacement measurement regardless of the position of the target. This includes thermal heating of optical components, building vibration, and acoustics. Control of non-cumulative errors can be accomplished through strict environmental control. This is discussed further in section 6.4.

## **6.2 Medium Frequency Noise**

Medium frequency noise is defined as 25 Hz or greater. The primary sources of medium frequency noise are acoustics and building vibrations. Fans, doors closing, people talking, or large trucks passing by will cause nm scale vibration on the optical table. Energy carried in these disturbances is primarily low frequency because of larger attenuation at higher frequencies, but vibration at frequencies greater than 25 Hz can and do reach the interferometer. Medium frequency noise can be largely avoided by taking measurements at night, when there is less activity in the building. Additional, measures taken to reduce

medium frequency noise are described in section 6.4.

### 6.3 Wide Band Noise

The primary source of wide band noise is the photodiode's optical shot noise. Shot noise ( $i_n$ ) is caused by the time varying flux of photons incident on the photodiode, and the quantized nature of photon energy. The output of the photodiode will change in quantized steps determined by the energy carried by a single photon. In addition, the output will fluctuate slightly over time, even when the intensity of the incident beam is constant. This is due to the statistical nature of quantum theory. Because the output from the photodiode is essentially digital, the spectrum will contain white noise. The generation of this noise is known as the Schottky effect.

Since shot noise is broadband, it is defined as a function of bandwidth.

$$i_n = \sqrt{2eI_o\Delta f} \quad (6.3)$$

where:  $e$  = charge carried by an electron  
 $I_o$  = photocurrent output from photodiode  
 $\Delta f$  = bandwidth of electronics used to sample  $I_o$

Wide band noise generated by the photodiode defines a maximum theoretical resolution of any interferometry system. The following expression describes the minimum detectable displacement  $\delta_{min}$  in heterodyne interferometers [37].

$$\delta_{min} = k_o^{-1} \left( \frac{2hc\Delta f}{P_o\lambda\eta} \right)^{1/2} \quad (6.4)$$

where:  $k_o$  = magnitude of the wave vector in free space  
 $h$  = Planck's constant  
 $c$  = speed of light  
 $\Delta f$  = electronics bandwidth (assumed 1 kHz)

$P_o$  = optical power incident onto the photodetector (1 mW)

$\lambda$  = laser wavelength (632.8 nm)

$\eta$  = quantum efficiency of the photodetector at the laser wavelength (60%)

This yields  $\delta_{\min} = 0.10$  pm. Under normal laboratory conditions, the environmental noise sources are expected to dominate significantly over the optical shot noise.

## 6.4 Noise Suppression

Many measures were implemented to remove low and medium frequency noise from the signal. The interferometer resides in an environmentally controlled room. The room has been separated from the building's air conditioning system to prevent unwanted heating or air circulation. The windows have been insulated to prevent heat exchange and subsequent changes in temperature. All devices requiring a fan or other moving parts have been moved outside of the room and the interferometer has been placed on a vibration damping table. The table has natural frequencies between 1 and 2 Hz, and therefore damps out high frequency vibration effectively, but is still susceptible to low frequency oscillations. Measurements taken at night generally are less prone to drift because of lower, more stable ambient temperatures and less activity in the building.

## 6.5 Compensation for Changes in Ambient Parameters

Considerable effort has been devoted to the compensation of cumulative and non-cumulative errors caused by changes in ambient parameters. Contributors include Estler [40], Bobroff [41], and Stone [42]. The first step in compensation is determining a relationship between ambient parameters and refractive index.

The refractive index of air is a well-known function of atmospheric pressure, air temperature, relative humidity, and carbon dioxide concentration by volume. An empirical equation developed by Edlen [43] has been used extensively in metrology. In 1981, however,

Jones [44] combined a precise determination of the density of moist air with Edlen's formulation to yield another representation. For a vacuum wavelength of  $\lambda = 632.8$  nm, typical of He-Ne lasers, Jones' result is

$$n(P, T, H, y) = 1 + A - B \quad (6.5)$$

$$A = 78.603 [1 + 0.540 (y - 0.0003)] \left[ \frac{P}{TZ} \right] \times 10^{-8} \quad (6.6)$$

$$B = (0.00042066 \cdot f \cdot e_s \cdot H) \times 10^{-8} \quad (6.7)$$

where:  $n$  = refractive index of air  
 $P$  = atmospheric pressure  
 $T$  = air temperature  
 $H$  = relative humidity  
 $y$  = carbon dioxide concentration  
 $Z$  = compressibility factor  
 $f$  = enhancement factor

In these equations pressure is in pascals, temperature in kelvins, humidity in percent, and  $y$  is the fractional  $\text{CO}_2$  concentration by volume. Three additional factors occur in Jones' representation:  $Z$  is a compressibility factor which reflects the departure of moist air from ideal gas behavior,  $f$  is an enhancement factor related to the effective saturation vapor pressure of water in air, and  $e_s$  is the saturation vapor pressure of pure water vapor over a plane surface of pure liquid water. Tables of  $Z$ ,  $F$ , and  $e_s$  are included in the appendix of the paper written by Jones.

By computing the partial derivatives of  $n(P, T, H, y)$  with respect to each of its arguments and evaluating the resulting expressions at near-standard conditions ( $P = 101,325$  Pa,  $T = 293.15$  K,  $H = 25\%$ , and  $y = 0.00034$ ), the sensitivity of the refractive index to changes in the ambient environment may be determined. Table 6.2 displays the change in each

parameter which causes a change of +1 part in  $10^8$  in the refractive index, as determined by Estler [40].

**Table 6.2: Sensitivity of refractive index to environmental parameters**

Parameter	Nominal Value	Change for which $\Delta n = +1$ part in $10^8$
Pressure	101,325 Pa (760 mmHg)	+3.73 Pa (+0.028 mmHg)
Temperature	293.15 K	-0.01°C
Humidity	25%	-1%
Carbon dioxide concentration	340 ppm	+67 ppm

It was proven in equations (6.1) and (6.2) that a change of 1 ppm in the refractive index causes a 10 nm error over a 10 mm measurement range. The effect of each of the ambient parameters is described in more detail in the following sections.

### 6.5.1 Pressure

As atmospheric pressure increases, so does air density, resulting in an increase in refractive index. This sensitivity is important for two reasons. During periods of rapid climatic change (a passing cold front, for example), atmospheric pressure may fluctuate by hundreds of pascals. Furthermore, using a vertically translating axis, it may be necessary to correct for the decrease in pressure with altitude. Near the earth's surface this gravitationally induced pressure gradient is approximately -13 Pa per meter, resulting in a decrease in  $n_{\text{air}}$  of more than three parts in  $10^8$  for each meter of vertical translation.

### 6.5.2 Temperature

Temperature will generally fluctuate 10 degrees or more over the course of a day. In addition, temperature gradients of a tenth of a degree can exist from one side of the optical table to the other, even in the relatively stable environment of a laboratory. The three fold

---

effect of changes in the refractive index, thermal expansion of optical components, and thermal expansion of the laser cavity causing wavelength shifts, makes temperature a crucial factor in controlling drift.

### **6.5.3 Humidity**

Water vapor is ~15% less refractive than dry air [40]. Therefore, as the relative humidity increases the refractive index decreases. This effect contributes only 0.01 ppm per percentage change in humidity. Over the course of a year, this may become significant but is generally not compensated for.

### **6.5.4 Carbon Dioxide**

Carbon dioxide is ~50% more refractive than standard air [40], meaning that an increase in CO<sub>2</sub> concentration causes an increase in the refractive index of air. A review article by Revell [45] surveys the present state of knowledge of the concentration of CO<sub>2</sub> in the earth's atmosphere. After 20 years of continuous measurement of CO<sub>2</sub> levels, Revell estimated an increase of approximately 1.4 ppm/year. Given that the refractive index changes only 0.01 ppm for a 67 ppm change in CO<sub>2</sub> concentration, it is unlikely that variation in  $y$  could be large enough to cause significant drift.

## 7.0 Calibration Method

The interferometer was successfully calibrated using a BM Hi-Tech piezoelectric wafer. A piezoelectric actuator was chosen from many alternatives because it is easily implemented, accurate, resistant to noise, and has a relatively wide bandwidth. The piezoelectric wafer was mounted inside a holder shown in figure 7.1. A hole in the center of the holder allows the laser beam to pass through and reflect off the mirror attached to the surface of the piezoelectric using double sided tape. The piezoelectric holder provides an insulated, rigid base, and spring-loads the piezoelectric to prevent any movement during calibration.

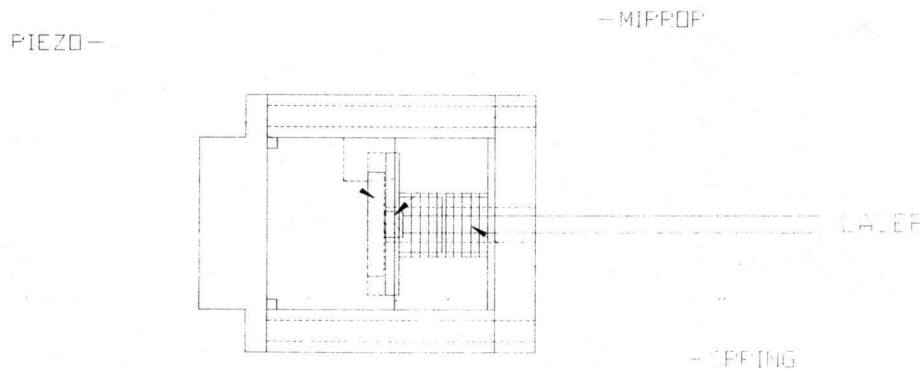


**Figure 7.1:** Piezoelectric holder

The holder is in turn mounted to a kinematic mirror mount which allows the piezoelectric to be rotated about two orthogonal axes, thereby aligning the laser beam to the photo-

diode.

Deflection of the piezoelectric occurs when a potential is created across the two surfaces. This causes an electric field to form within the piezoelectric material, expanding or contracting the crystal lattice structure depending on the direction of the applied field. The amount of deflection is given by a material property named the  $d_{33}$ .

$$\Delta x = d_{33} \cdot V \quad (7.1)$$

where:  $d_{33} = 580 \pm 5 \text{ pm/V}$  [46]

Assuming that the voltage can be measured to within 0.5 V, the uncertainty of a measurement taken with  $V = 50 \text{ V}$  will be

$$\Delta x = (580 \pm 0.86\%)(50.0 \pm 1\%) = 29.0 \text{ nm} \pm 1.86\% = 29.0 \pm 0.5 \text{ nm} \quad (7.2)$$

This is well within the desired accuracy of  $\pm 1 \text{ nm}$ .

To create a periodic, repeatable deflection of the piezoelectric, a stepping circuit was implemented to create a modified square wave. The circuit is capable of outputting between 0 and 250 V, which corresponds to a displacement range of 0 to 72.5 nm.

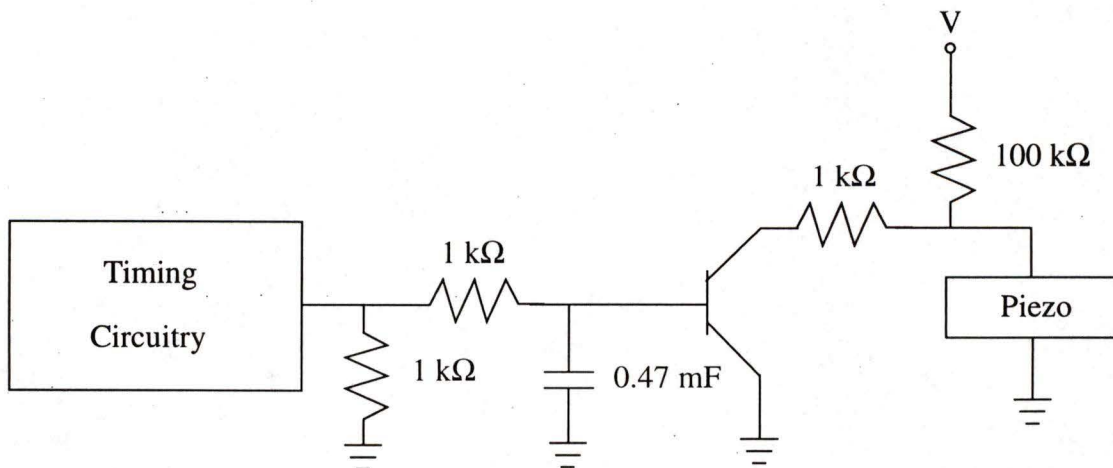


**Figure 7.2:** Piezoelectric stepping circuit

The timer circuitry can be programmed for any frequency, and activates the transistor with a 5 V output. In order to avoid jogging the piezoelectric or the mirror through excessive acceleration, the voltage is ramped using a 470  $\mu\text{F}$  capacitor in parallel with the transistor. The output from the circuit, at a setting of 50 V, is shown in figure 7.3.

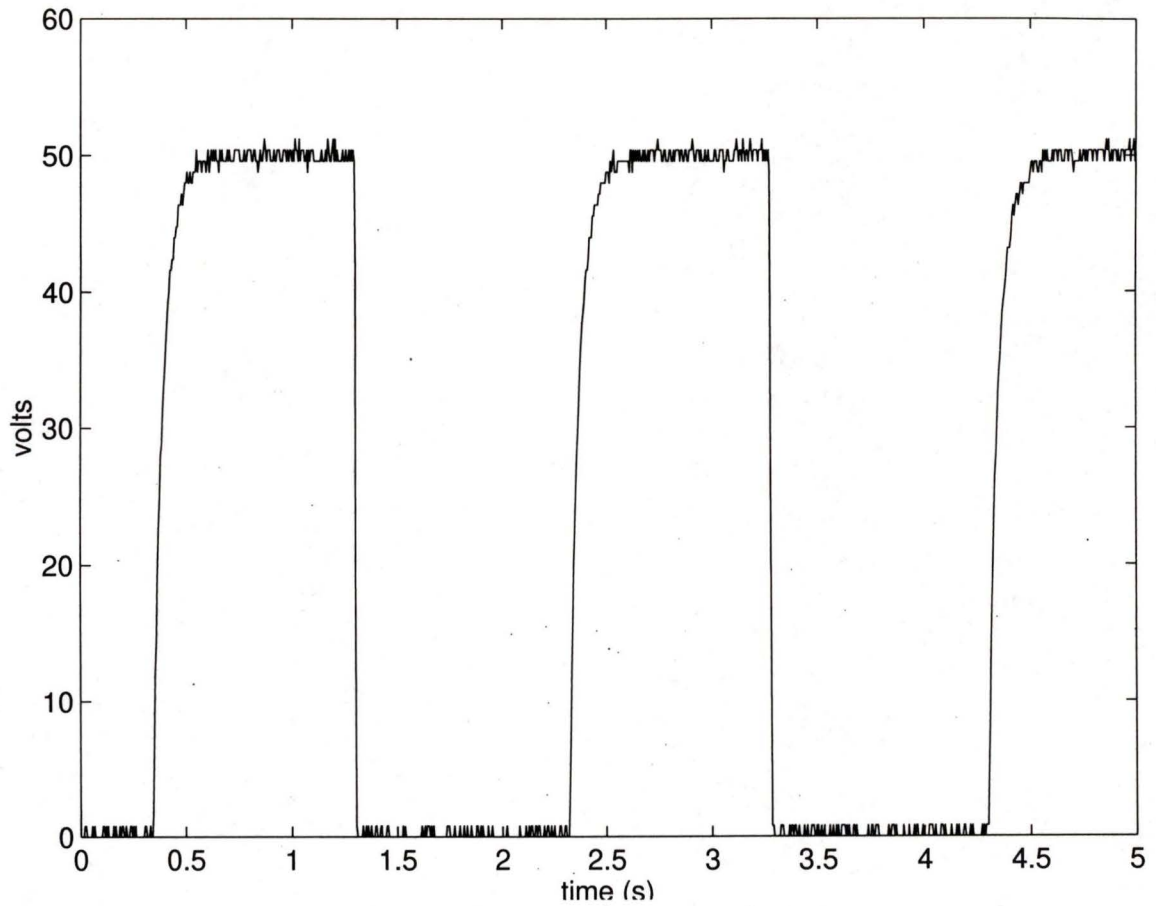


*Figure 7.3: Piezoelectric circuit output*

# 8.0 Results

The following section outlines the calibration results, measurement of bandwidth and drift, as well as the attempt to measure the effects of temperature on drift.

## 8.1 Calibration

The heterodyne interferometer is calibrated using a BM-Hitech ceramic piezoelectric. A known voltage is applied to the ceramic, creating a known displacement. Figure 8.1 shows the measured displacements for six different voltage settings.

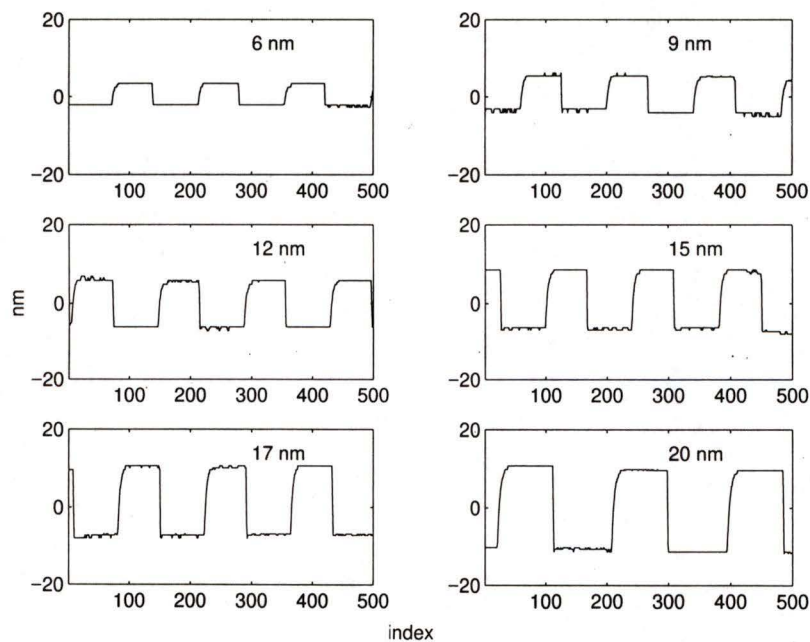


*Figure 8.1: Interferometer measurement of piezoelectric steps*

A total of 17 displacements were measured between 6 and 29 nm. Repeated measurements confirmed that the instrument is both accurate and repeatable to within 1 nm. The measured displacements for two data sets are shown in figures 8.2 and 8.3.

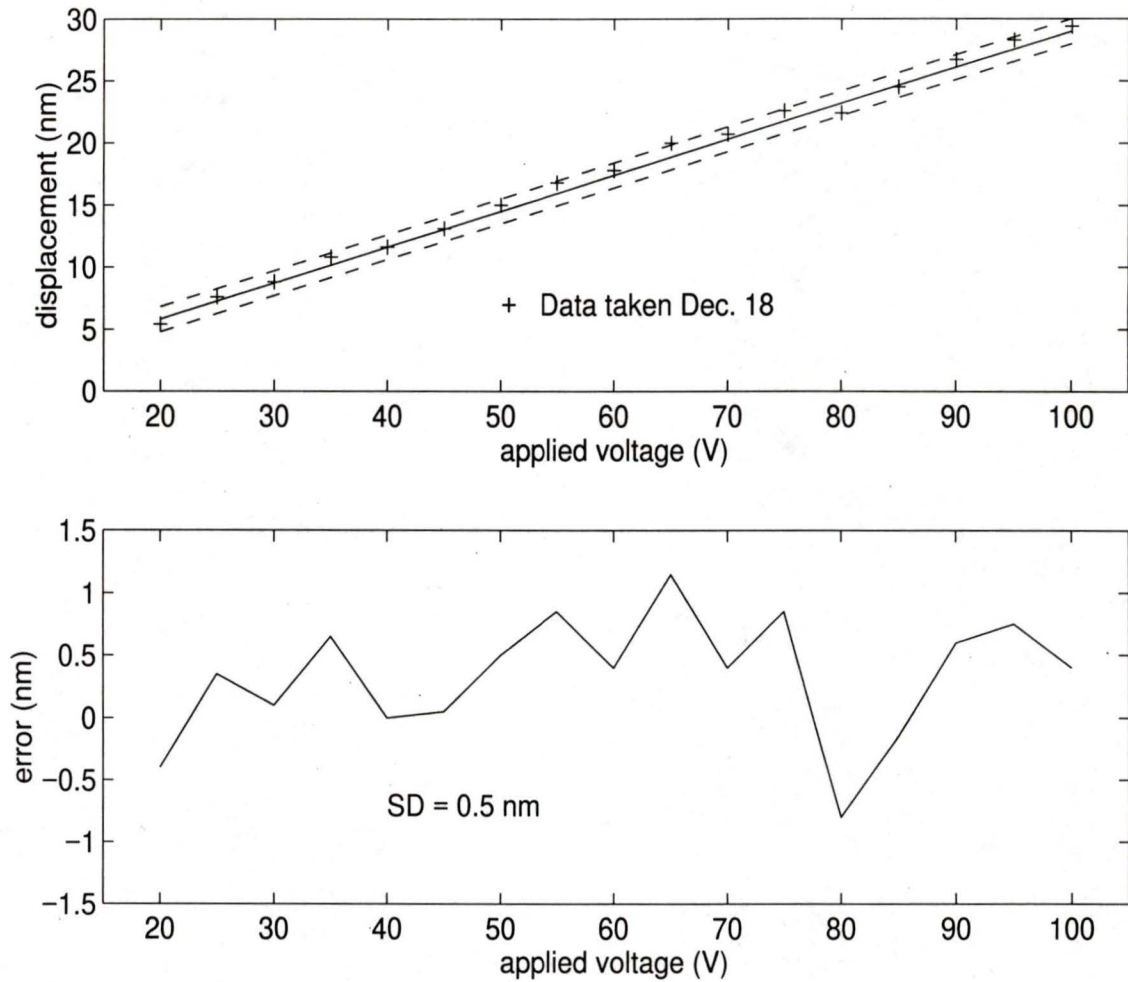


**Figure 8.2:** Interferometer calibration data - Dec. 18

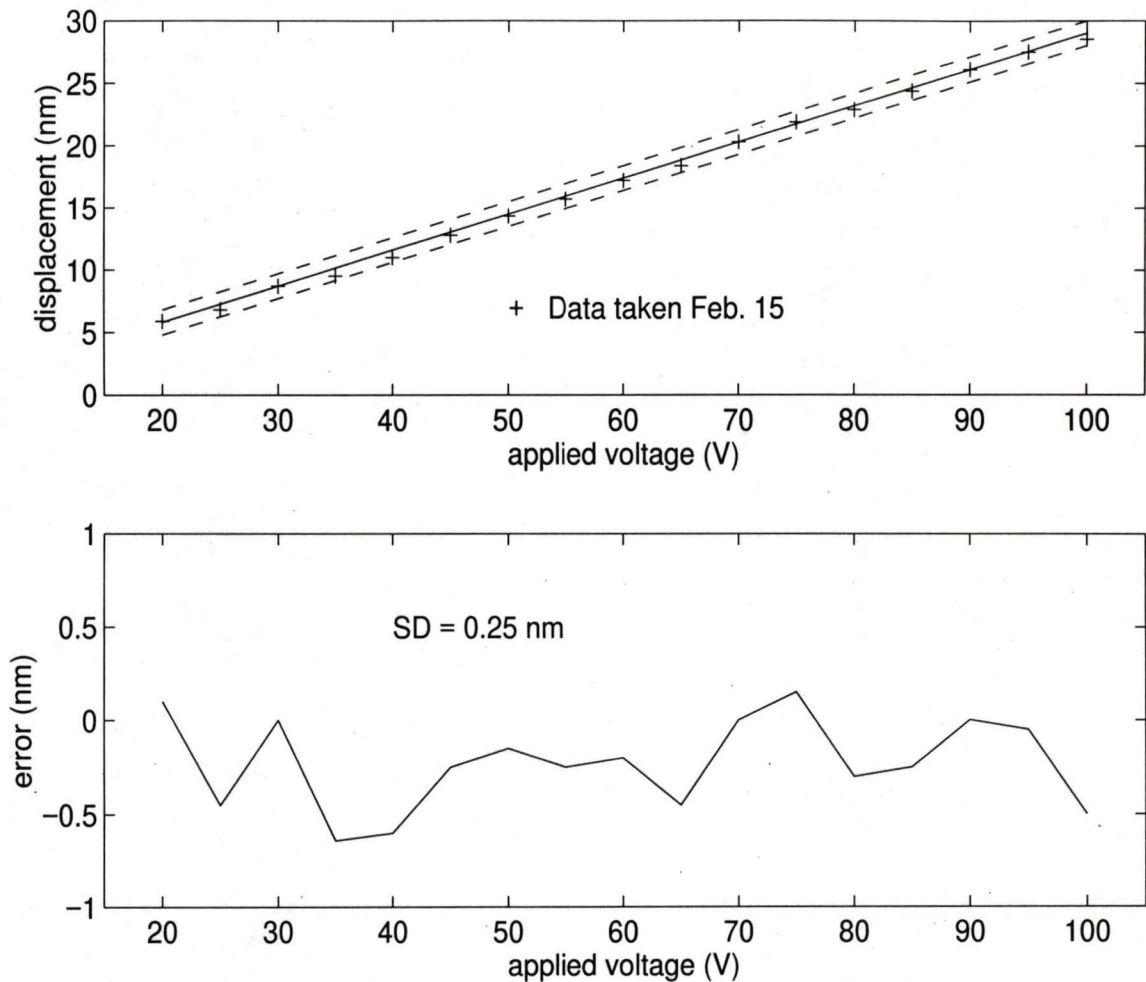


**Figure 8.3:** Interferometer calibration data - Feb. 15

The solid line indicated the expected output, and the dashed lines corresponds to  $\pm 1$  nm. Both data sets were taken late at night, which accounts for the low standard deviation. Measurements taken during the day are noticeable less accurate, as described in the following section.

Resolution is defined as one standard deviation of the measured data, and is somewhere between 0.25 nm and 0.5 nm. Accuracy can be safely defined as three standard deviations and is somewhere between 0.75 nm and 1.5 nm.

---

## 8.2 Displacement Error Analysis

As described in section 6.1, low frequency drift in the interferometer output is caused by low frequency fluctuations in temperature, pressure, humidity, and laser wavelength, as well as seismic disturbances. Medium frequency error is caused by building vibrations and acoustics.

In an attempt to control higher frequency vibration, the optical table was placed on inflatable tires. The tires have natural frequencies in the range of 1 to 2 Hz, and effectively damp out noise caused by floor vibration and acoustics. The system, however becomes more susceptible to vibration below the natural frequencies of the table. Sharp impacts caused by doors closing and people walking carry enough energy at low frequencies to start the table oscillating.

Sections 8.2.1 and 8.2.2 analyze low and high frequency displacement errors in the interferometer output. In both sections, a comparison is made between displacement error with and without tires.

### 8.2.1 Low Frequency

The following figures show drift in the interferometer output over a 40 minute period at 2 Hz. To prevent aliasing, each point consists of 200 points sampled at 1000 Hz and averaged. Two data sets were taken at different times of day to demonstrate the effect of ambient conditions and the amount of activity in the building on the interferometer output.

Data shown in figure 8.4 was taken with the optical table mounted on vibration damping tires. One was taken in the morning on a weekday. There was activity both in the building and within the lab, and the temperature was increasing. The second data set was taken at night. Temperature was relatively stable, and there was very little activity in the building.

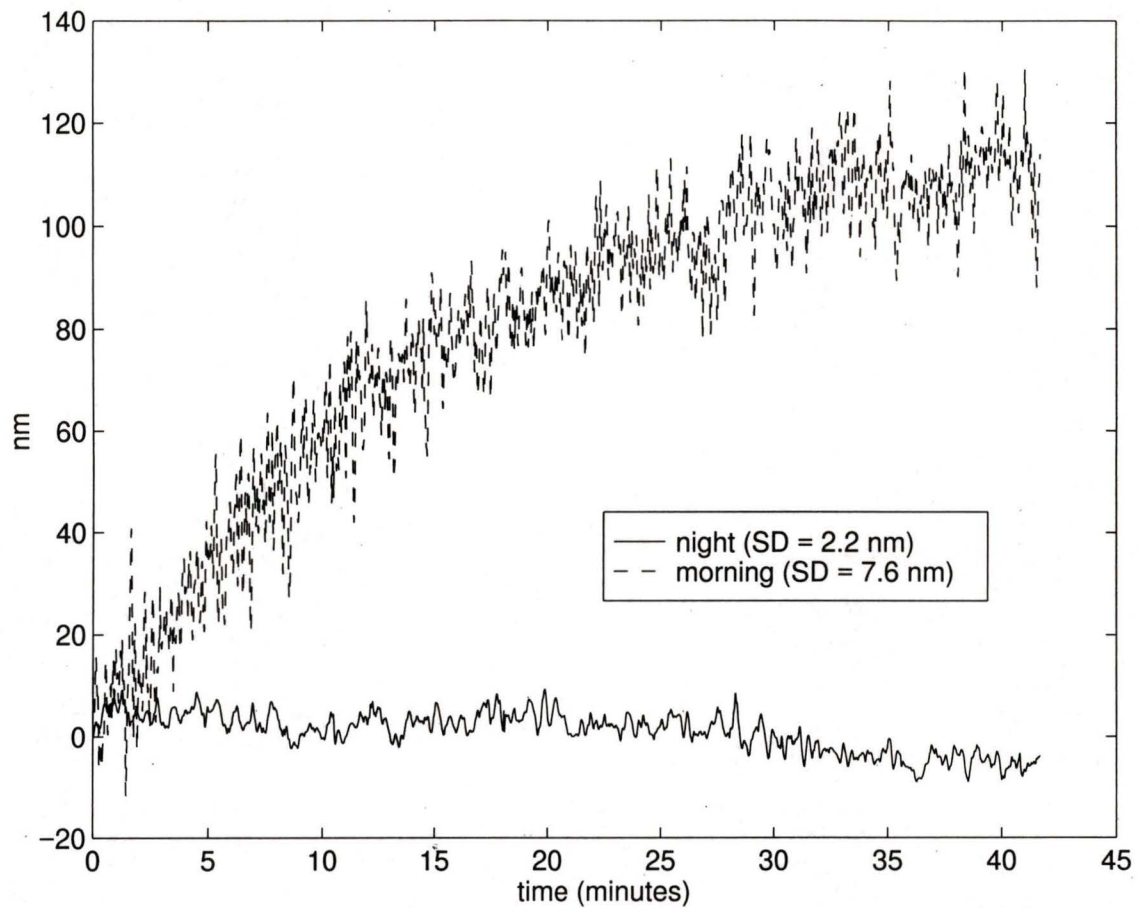


**Figure 8.4:** Interferometer long term drift - with tires

The deterministic component of the two signals is due to change in the ambient temperature - this is discussed further in section 8.3. The output is modulated by periodic oscillations with frequencies on the order of 0.1 Hz - far too low for effective damping by the tires.

The standard deviation of the periodic component is calculated by removing the deterministic trends, and can be seen to increase significantly during the day time when the activity in the building is greater. This suggests that much of the non-deterministic drift is caused by vibration and acoustics, which obviously have greater amplitude during the day when there is activity in the building.

Figure 8.5 shows data sets taken with the vibration damping tires of the optical table deflated. As before, one data set was taken in the morning on a weekday with temperature rising and activity in the building. The second data set was taken at night. Temperature was relatively stable, and there was very little activity in the building.

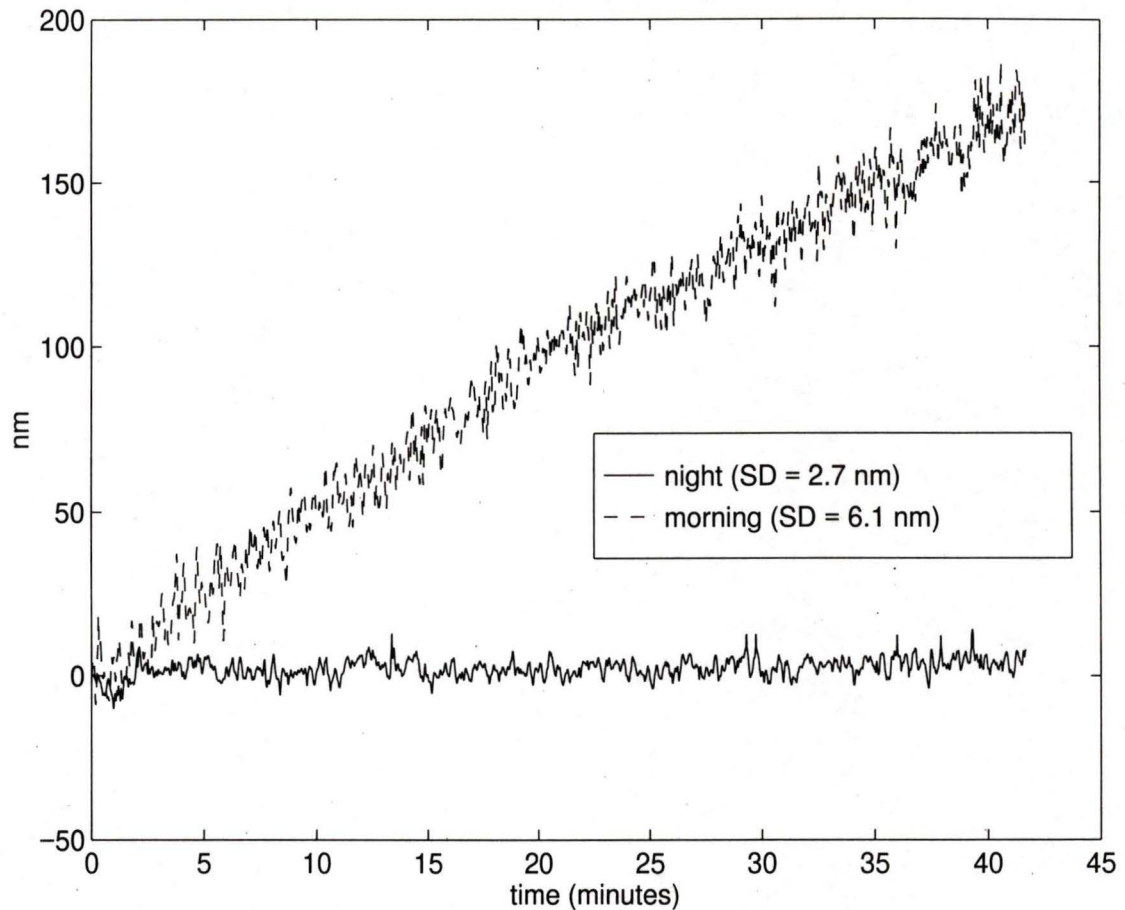


**Figure 8.5:** Interferometer long term drift - no tires

As expected, the general trends of the drift measurements was unchanged by the absence of tires: a temperature dependant deterministic component modulated by low frequency building vibrations. This confirms that the frequencies of these oscillations are too low to be damped.

---

The most likely cause of the periodic disturbance is seismic waves brought about by activity in the building. Low frequency compression waves can travel great distances with very little attenuation. The frequencies are far below the natural frequencies of the table, and would pass easily to the optical components. This theory is substantiated by the fact that the standard deviation increases significantly during the day. A second theory is the effect of pressure waves caused by the building ventilation system turning on and off. As with low frequency seismic disturbances, pressure waves can travel long distances without significant attenuation. However ventilation systems generally only trigger on an hourly basis, making it doubtful that they could contribute to the periodic component of the interferometer drift.

This leaves the difficult question of how to eliminate such low frequency disturbances. Obviously, taking measurements at night will provide better results. Even greater attenuation can be achieved by reducing the optical path lengths of both the signal and reference beams. If the optical path lengths are small enough, the phase error due to a propagating wave will be equal and in phase for both the signal and reference and will cancel.

### **8.2.2 Medium Frequency**

Medium frequency noise is measured by sampling 5 s of data at 1000 Hz. The data is anti-aliased in hardware using a second order analog filter with  $f_c = 400$  Hz.

The following data set was taken at night, with little or no activity in the lab. The optical table is mounted on a vibration damping table.

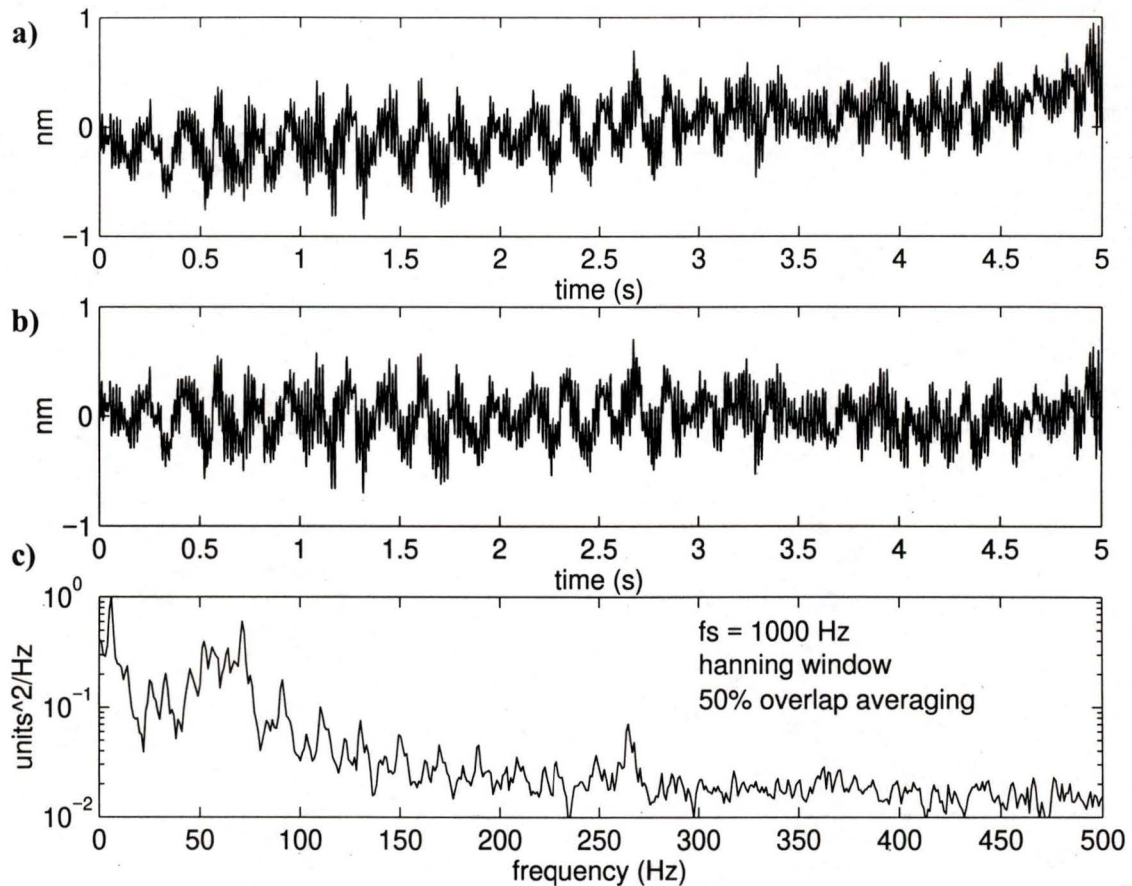


**Figure 8.6:** Interferometer short term drift - with tires

- where:
- a) Time series of displacement over 5 s interval
  - b) Time series of displacement with drift component removed
  - c) Spectrum of time series shown in b)

Due to the relative stability of ambient conditions at night, and the short time period over which the measurement was taken, low frequency drift is only  $\pm 0.5$  nm. Figure 8.6b shows the signal after removal of drift, which is then Fourier transformed using averaging in the frequency domain with 50% overlap. The residue of the free run signal is dominated by 60 Hz noise, making it difficult to take sub-nanometer measurements accurately, without resorting to averaging. However, sub-nanometer vibration can be detected, as shown in the spectrum of the free run data. The frequency component at 270 Hz corresponds to the

vibration frequency of the computer fan, located in the adjacent room (this was confirmed by measuring the vibration frequency of the fan with an accelerometer). The amplitude of this vibration signal is extremely weak after passing through the floor, and through the vibration damping table. It is estimated that the amplitude is less than half a nanometer, but is still detectable.

A second data set was taken with the vibration damping tire deflated, also at night. This data set is shown in figure 8.7.

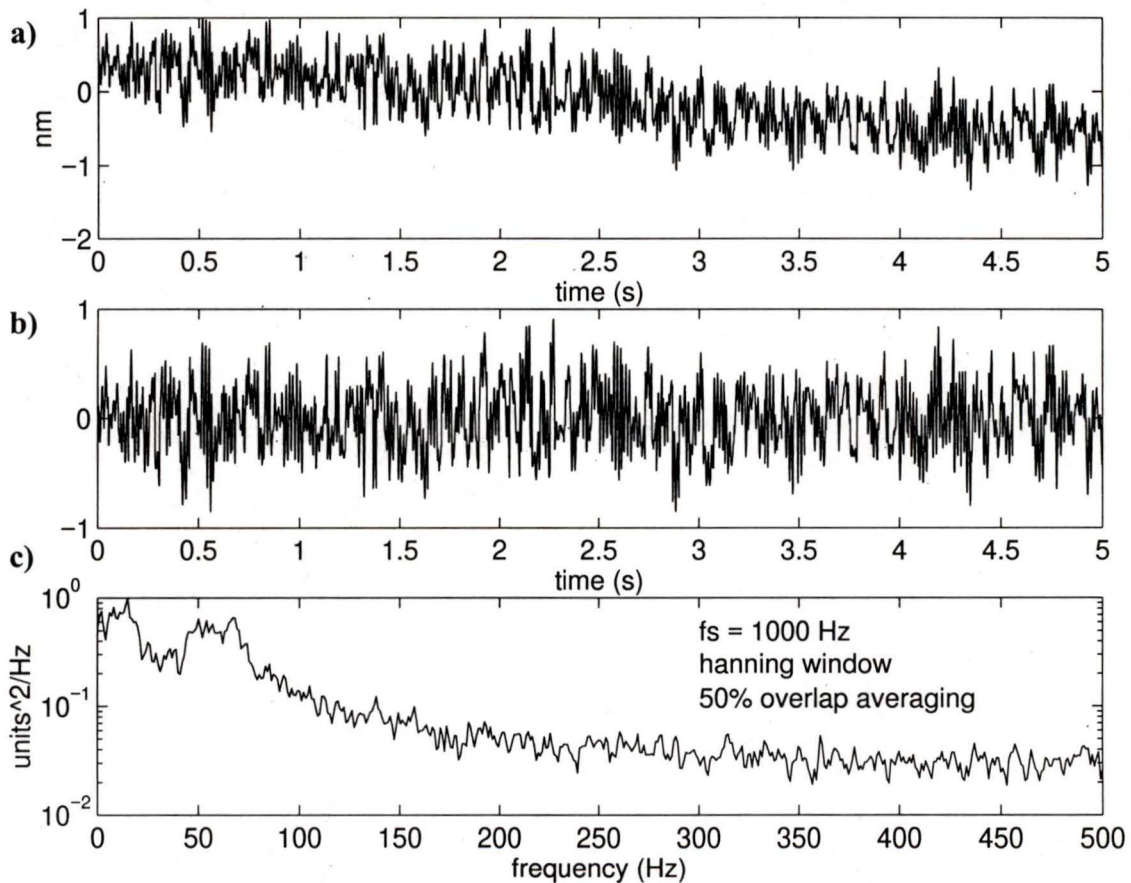


**Figure 8.7:** Interferometer short term drift - no tires

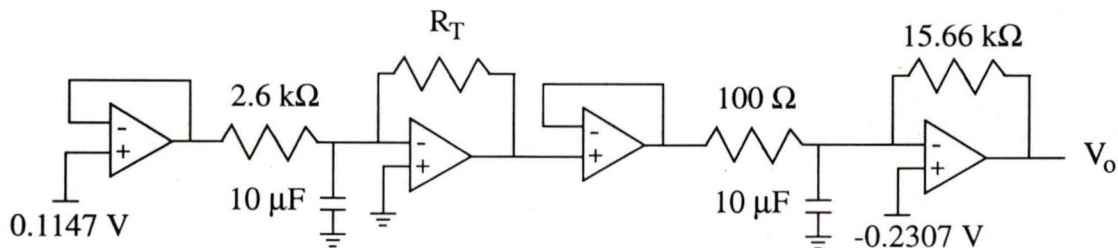
- where:
- a) Time series of displacement over 5 s interval
  - b) Time series of displacement with drift component removed
  - c) Spectrum of time series shown in b)

Figure 8.7a shows a drift of approximately 1 nm over the 5 second period. The spectrum is similar to the one shown in figure 8.6c, with vibration damping tires inflated. This indicates that there is very little medium frequency noise present at night when there is no activity within the building. It also indicates that vibration due to fans outside the room and any other vibrating machinery in the building contributes only sub-nanometer noise to the signal, virtually undetectable within the 60 Hz noise.

It is important to note that the vibration damping tires are effective in damping high frequency noise caused by people walking, talking, closing doors, etc. It is difficult to demonstrate this, however, due to the transient nature of the signals.

### 8.3 Measurement of Temperature Sensitivity

In an attempt to investigate the effect of ambient conditions on the interferometer's output, the ambient temperature was measured in conjunction with the displacement over half hour intervals. Temperature was measured using a Fenwal 5 k $\Omega$  bead thermistor. The thermistor was connected in the feedback of a operational amplifier, as shown in figure 8.8.



**Figure 8.8:** Temperature measurement circuit

After signal conditioning and filtering, the instrument sensitivity, as dictated by the A/D 12 bit converter, is 1.7 $^{\circ}$ mC. The thermistor, however, will self heat by 1 $^{\circ}$ C for every 4 mW of power. Given an input voltage of 0.1147 V, current sent through the thermistor will cause 0.01 $^{\circ}$ C drift. The thermistor is not calibrated because the intention is only to prove a cross-correlation between temperature and drift, which requires precision and not accuracy.

Three data sets were taken at different times of day in order to prove repeatability of the results. The first data set was taken at 5:30 pm; ambient temperature is decreasing.

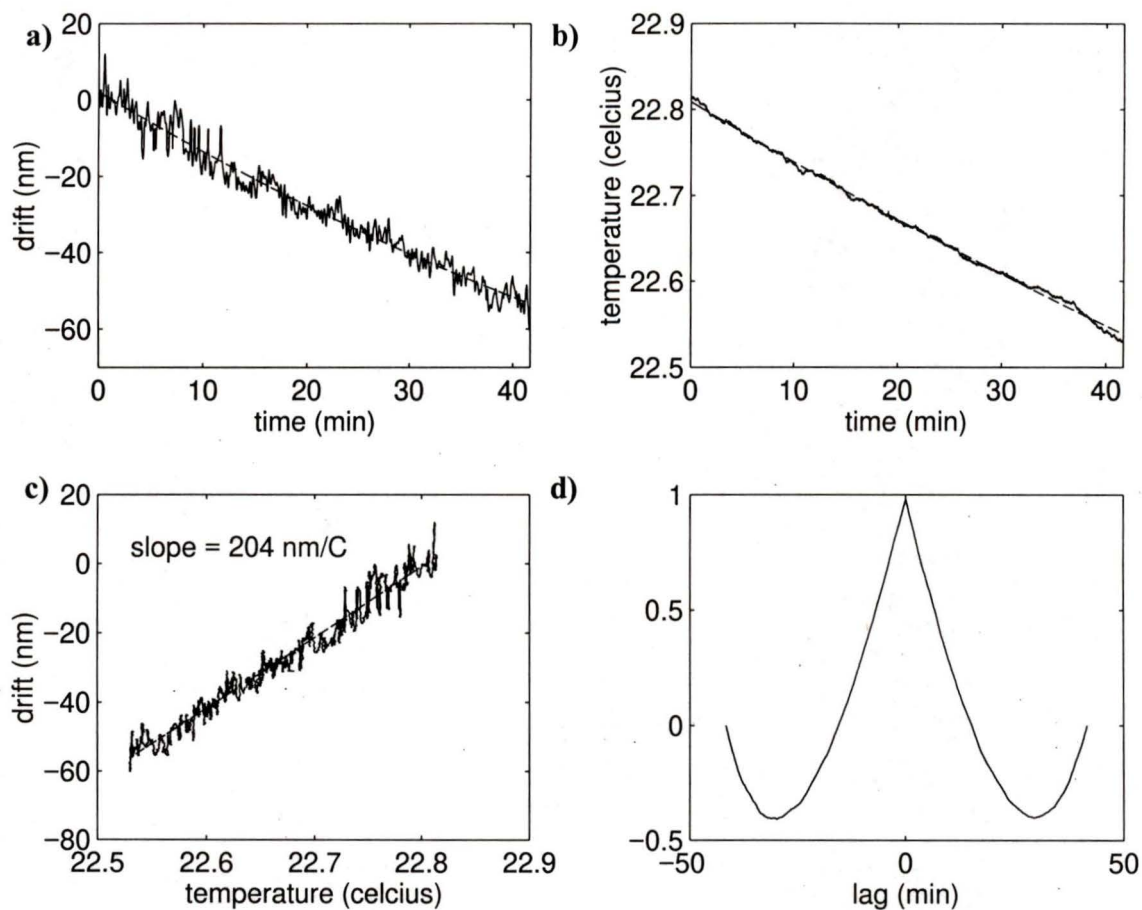


**Figure 8.9:** Temperature and displacement measurement #1

where: (a) Interferometer displacement measurement  
 (b) Temperature measurement  
 (c) Linear relationship  
 (d) Cross correlation

The instrument drifts by approximately 50 nm over the 40 minute measurement interval. When compared to the temperature change shown in part (b), we can see that there is a linear relationship with a slope of 204 nm/°C. This drift is composed of both the non-cumu-

relative error of thermal expansion of optical components, and the cumulative error caused by a shift in wavelength. Theoretically, the interferometer is balanced to prevent cumulative error, but there is significant error in the balancing process. The measured sensitivity to temperature is considerably higher than the value of  $100 \text{ nm}/^\circ\text{C}$  quoted by Charette [37]. This may be due to a different laser cavity size, a less compact design, or different materials used for the optical components. The displacement and temperature measurements are de-measured and cross-correlated in figure 8.9d. Of course, the cross-correlation of two lines is very close to one.

Figures 8.10a and 8.10c show the displacement and temperature measurements after removing the deterministic components. Figures 8.10b and 8.10d show the spectra of the displacement and temperature data sets after the deterministic component is removed.

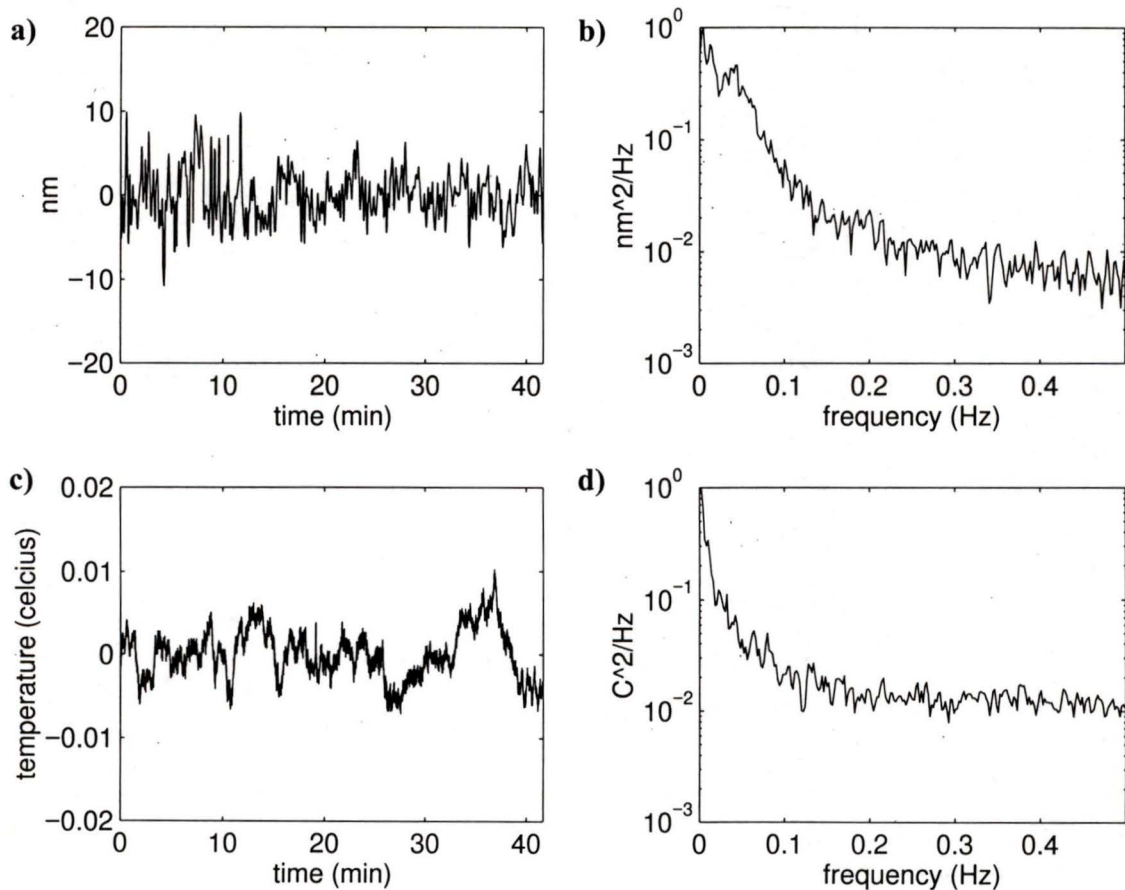


**Figure 8.10:** Periodic component of displacement and temperature #1

- where:
- (a) Periodic component of displacement drift
  - (b) Spectrum of time series shown in a)
  - (c) Periodic component of temperature
  - (d) Spectrum of time series shown in c)

It can be seen that the periodic disturbances are not caused by temperature. Temperature fluctuations shown in 8.10c have an amplitude of approximately  $\pm 0.01^\circ\text{C}$ , corresponding to  $\pm 2$  nm. The periodic component of displacement drift shown in figure 8.10a has an amplitude of approximately  $\pm 10$  nm. The relationship between 8.10a and 8.10c can be determined analytically by measuring the coherency of the two time series.

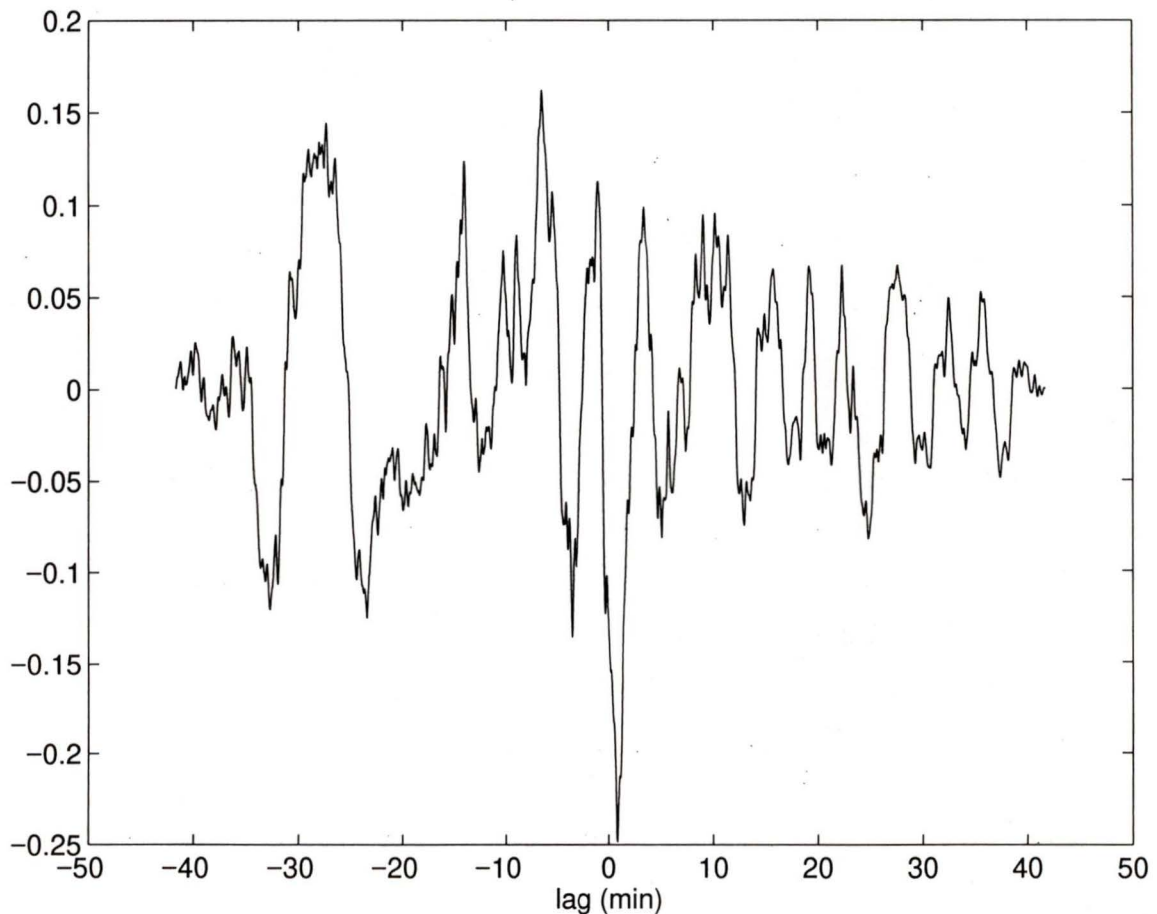


**Figure 8.11:** Cross correlation of displacement and temperature #1

Figure 8.11 shows that there is no coherency between the two signals, confirming that the

periodic fluctuations in the interferometer output are not caused by temperature fluctuations. This finding gives further weight to the argument that the periodic component of drift is caused by low frequency seismic disturbances - see section 8.2.1 for further discussion.

Figure 8.12 is a displacement and temperature set taken in the evening. Temperature is decreasing, and activity in the building is significantly less than during the daytime.

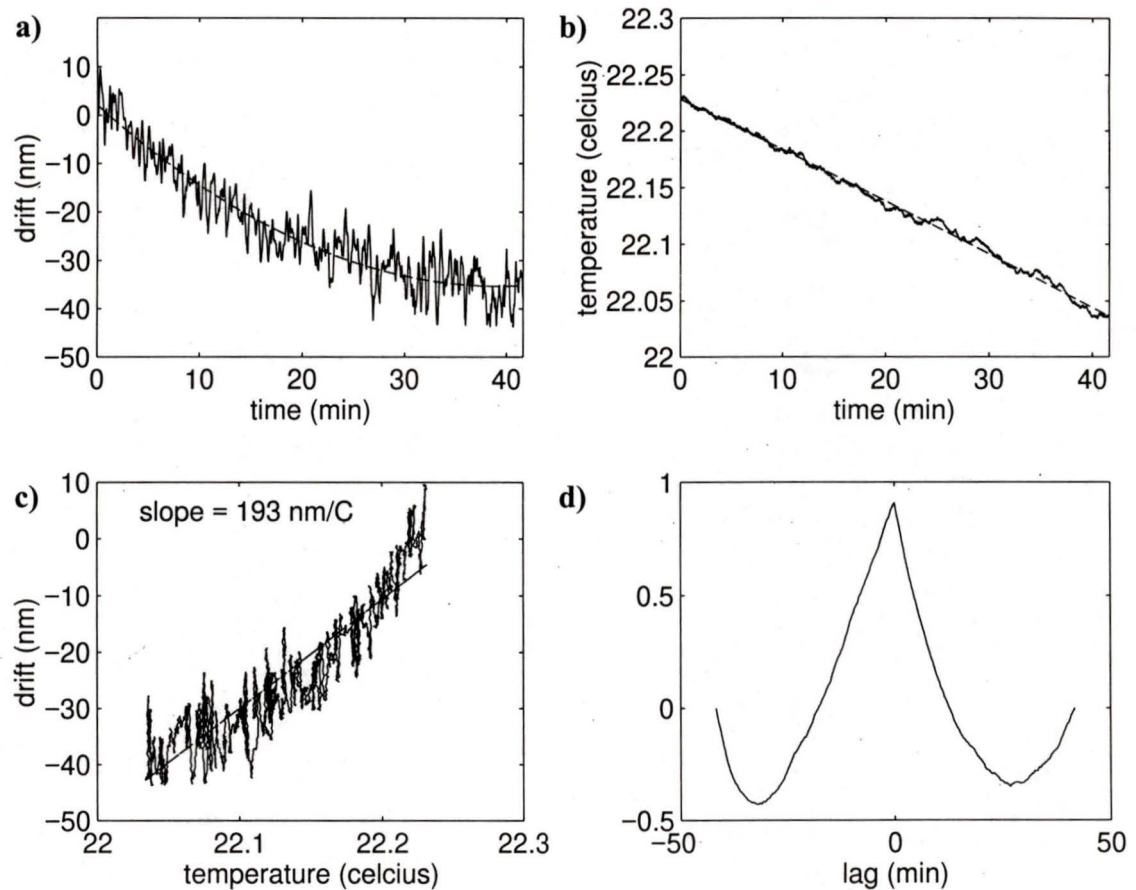


**Figure 8.12:** Temperature and displacement measurement #2

where:

- (a) Interferometer displacement measurement
- (b) Temperature measurement
- (c) Linear relationship
- (d) Cross correlation

The slope in this case is  $193 \text{ nm}/^{\circ}\text{C}$ , within 5% of the first measurement. The discrepancy in slope measurements is most likely caused by the other sources of drift, such as pressure and humidity, which do not have as strong an affect on the output. The periodic components and spectra are shown in figure 8.13.

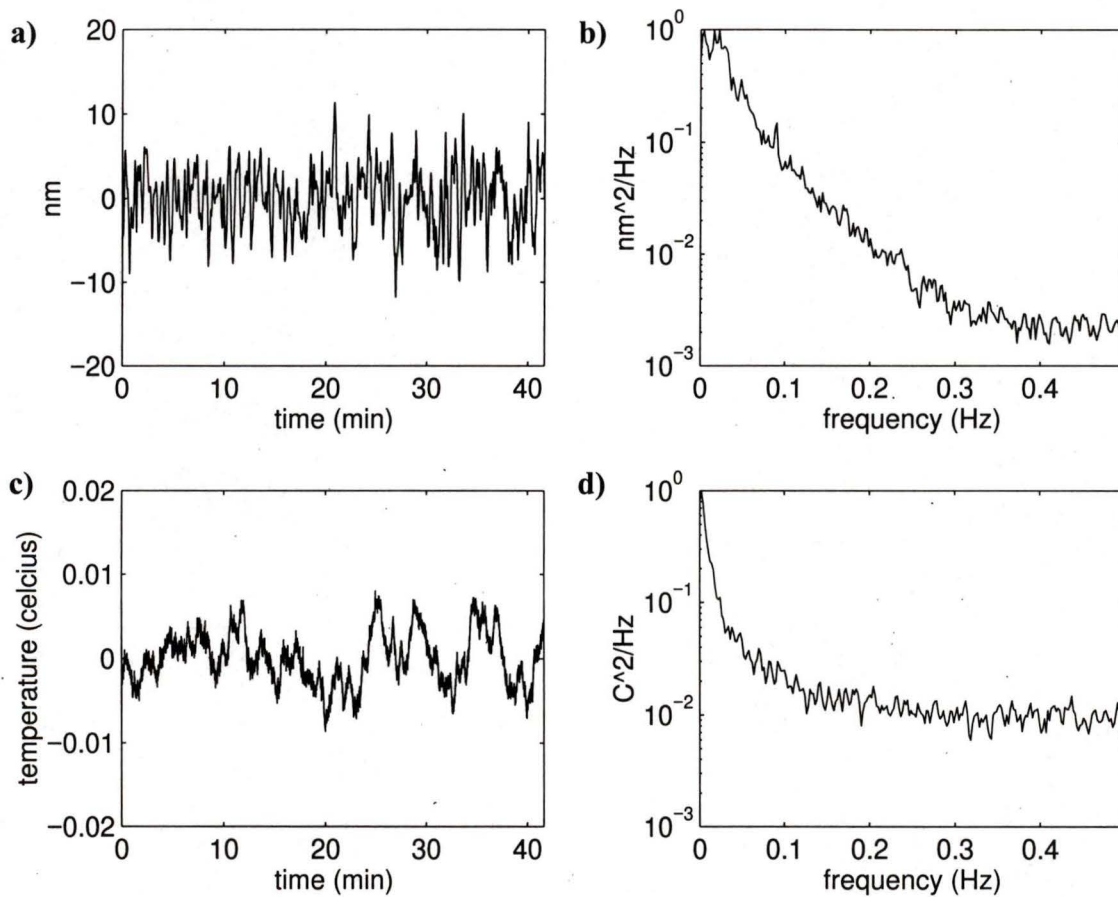


**Figure 8.13:** Periodic component of displacement and temperature #2

where: (a) Periodic component of displacement drift  
 (b) Displacement drift spectrum  
 (c) Periodic component of temperature  
 (d) Temperature spectrum

As before, both the spectra and the cross-correlation, shown in figure 8.14, indicate that the periodic component of the displacement drift are not caused by temperature changes.

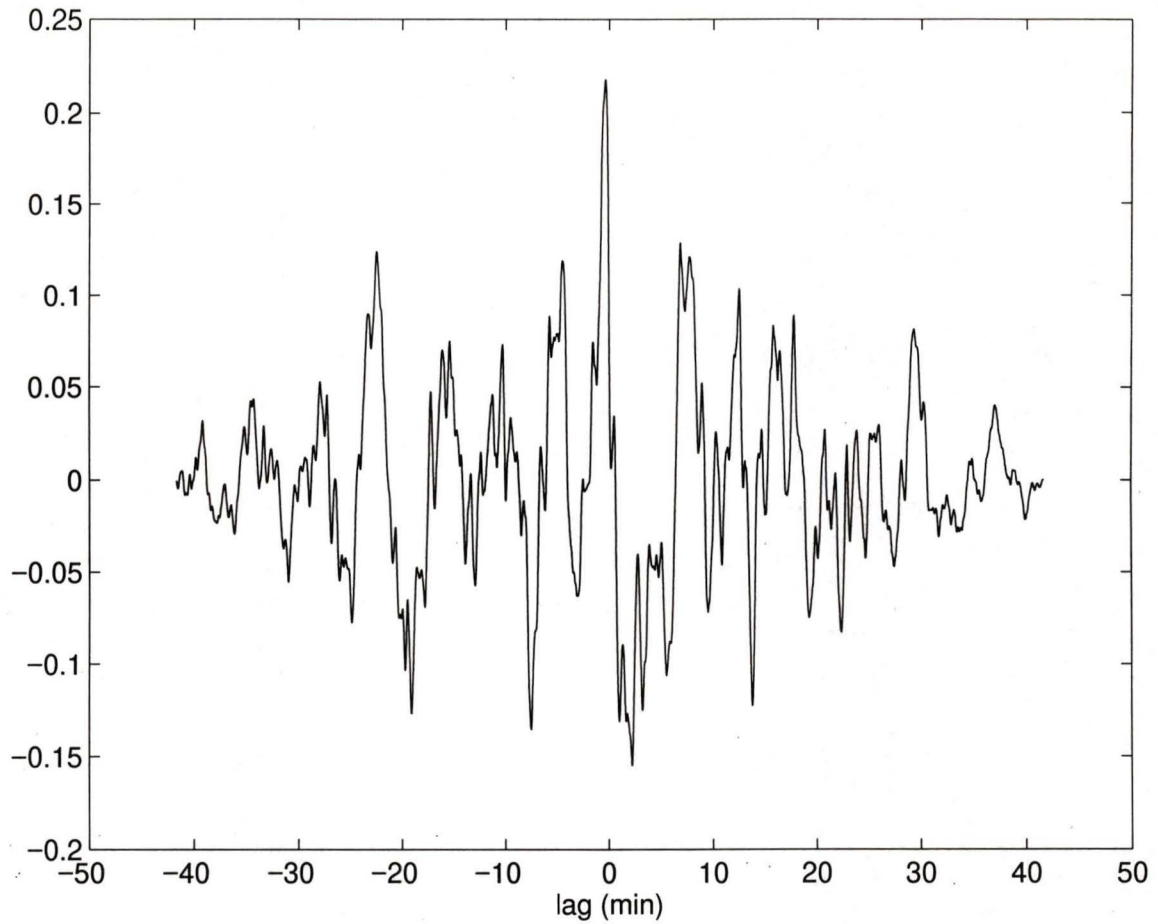


**Figure 8.14:** *Cross correlation of displacement and temperature #2*

A displacement and temperature data set was taken in the morning. Temperature was increasing and there was activity in the building and the lab. Figure 8.15 reports the data gathered in this final test.

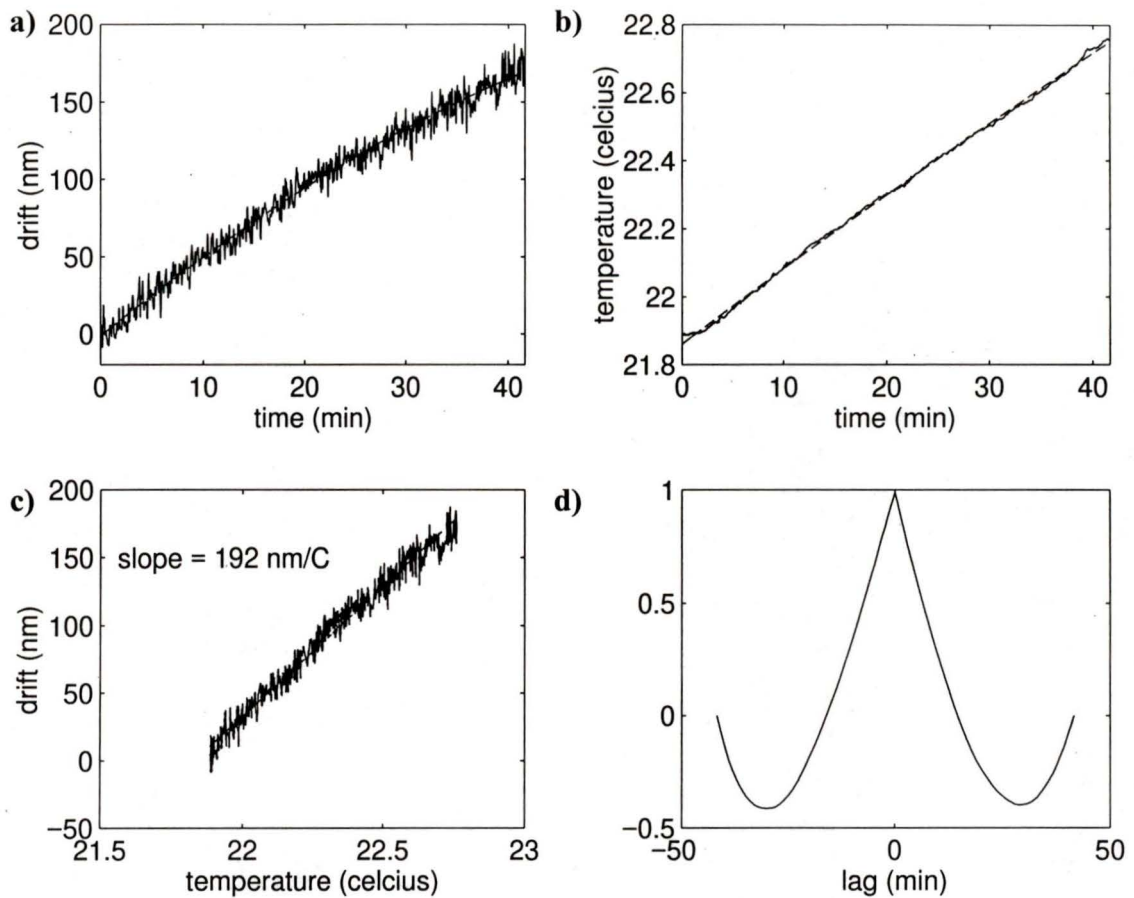


**Figure 8.15:** Temperature and displacement measurement #3

where: (a) Interferometer displacement measurement  
 (b) Temperature measurement  
 (c) Linear relationship  
 (d) Cross correlation

The slope in this case is  $192 \text{ nm}/^{\circ}\text{C}$ , very close to the previous two drift measurements. Once again, the deterministic components correlate very well, but the periodic components do not, as shown in figures 8.16 and 8.17.

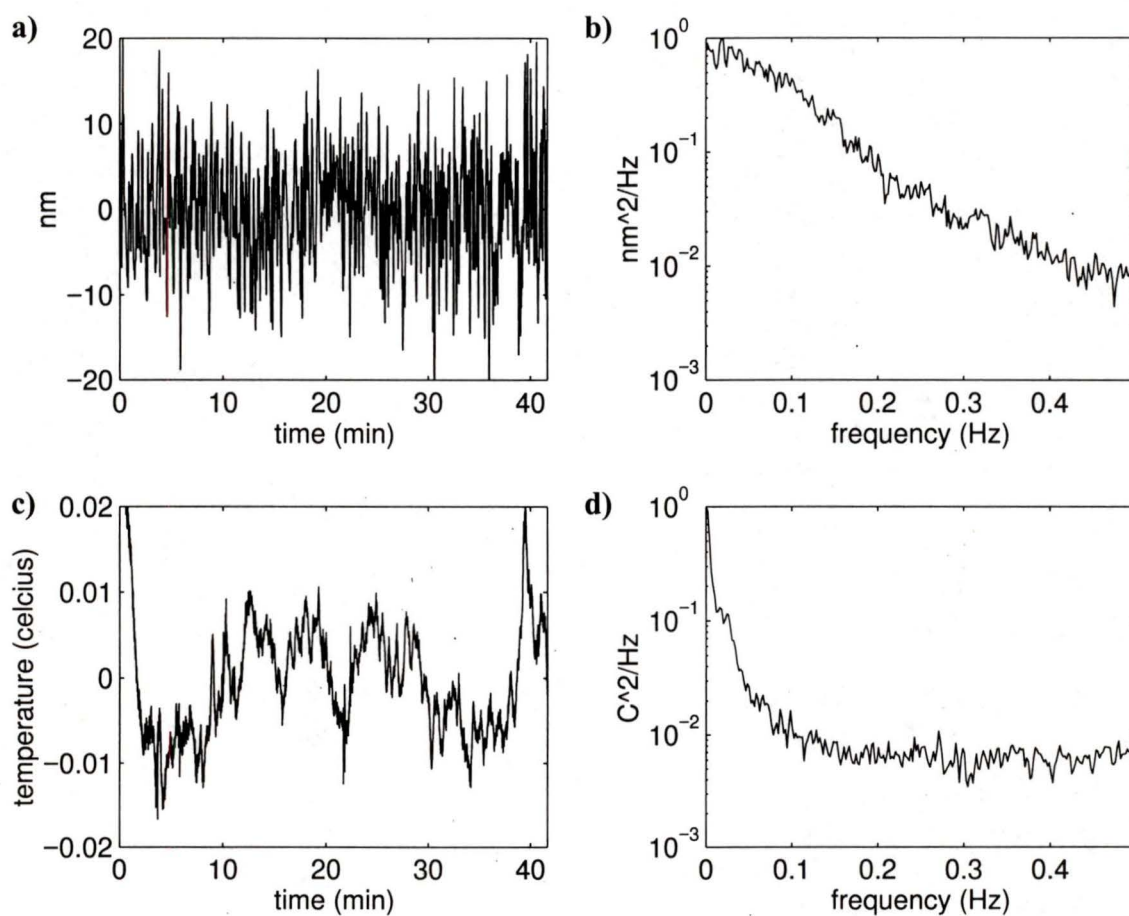


**Figure 8.16:** Periodic component of displacement and temperature #3

where:

- (a) Periodic component of displacement drift
- (b) Displacement drift spectrum
- (c) Periodic component of temperature
- (d) Temperature spectrum

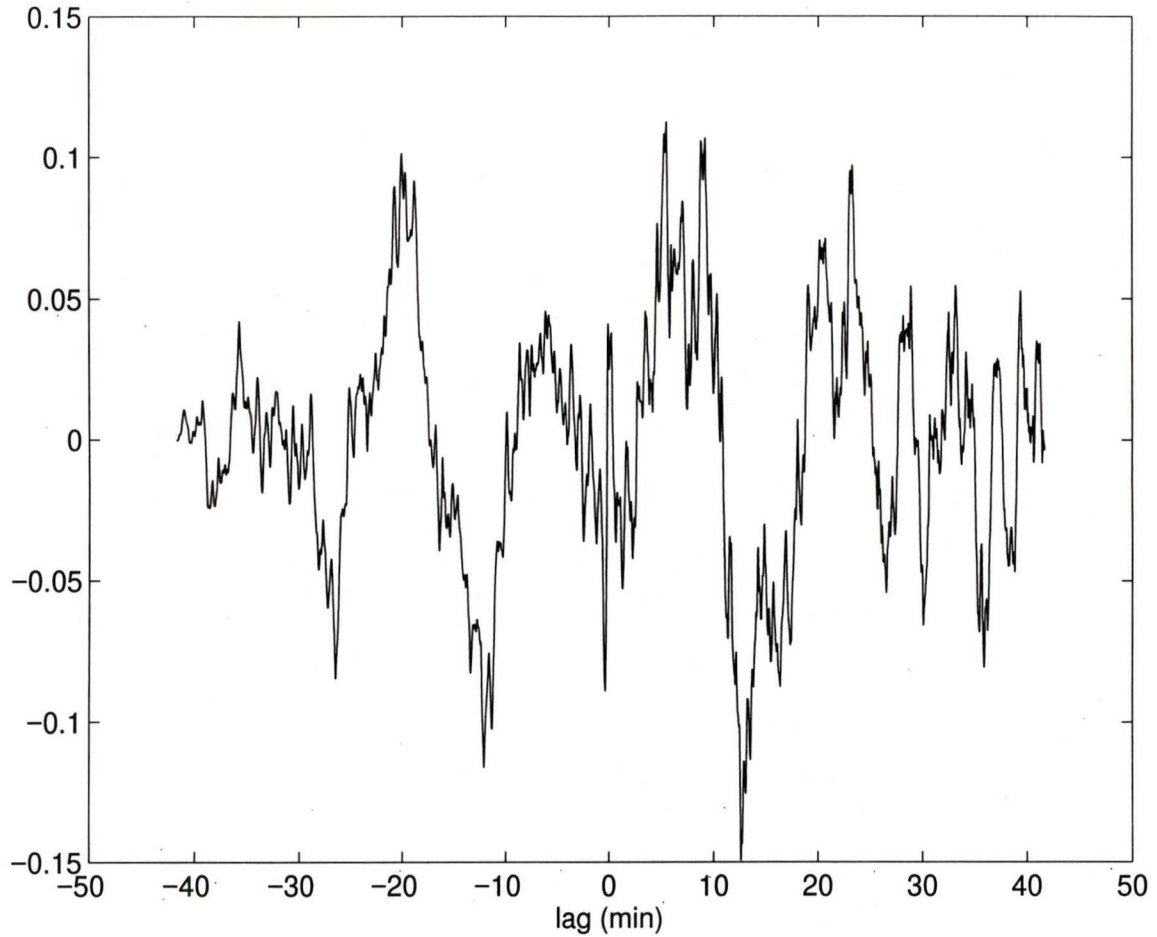


**Figure 8.17:** *Cross correlation of displacement and temperature #3*

The effect of temperature on drift, therefore, can be approximated to be  $200 \text{ nm}/^{\circ}\text{C}$ . Temperature effects on the interferometer output are extremely low frequency, with periods on the order of hours. Periodic components with frequencies of  $0.1 \text{ Hz}$  and less are present in the signal, and are most likely due to seismic disturbances. Methods for attenuating these low frequency disturbances are discussed in section 8.2.1.

## 8.4 Bandwidth

The bandwidth of the interferometer is a function of resolution. Low resolution (i.e. 80 nm or greater) measurements are sampled through the high speed quadrature decoder at a rate of 10 MHz. This is reduced by an anti-aliasing filter to approximately 1 MHz, corresponding to a maximum speed of 220 cm/s. Samples taken by the A/D board determine the low resolution portion of the displacement measurement. The sample rate of the A/D is far lower than the quadrature decoder, and can be determined by reading a periodic displacement with a known period. The following figure shows a square wave with a 2 second period.

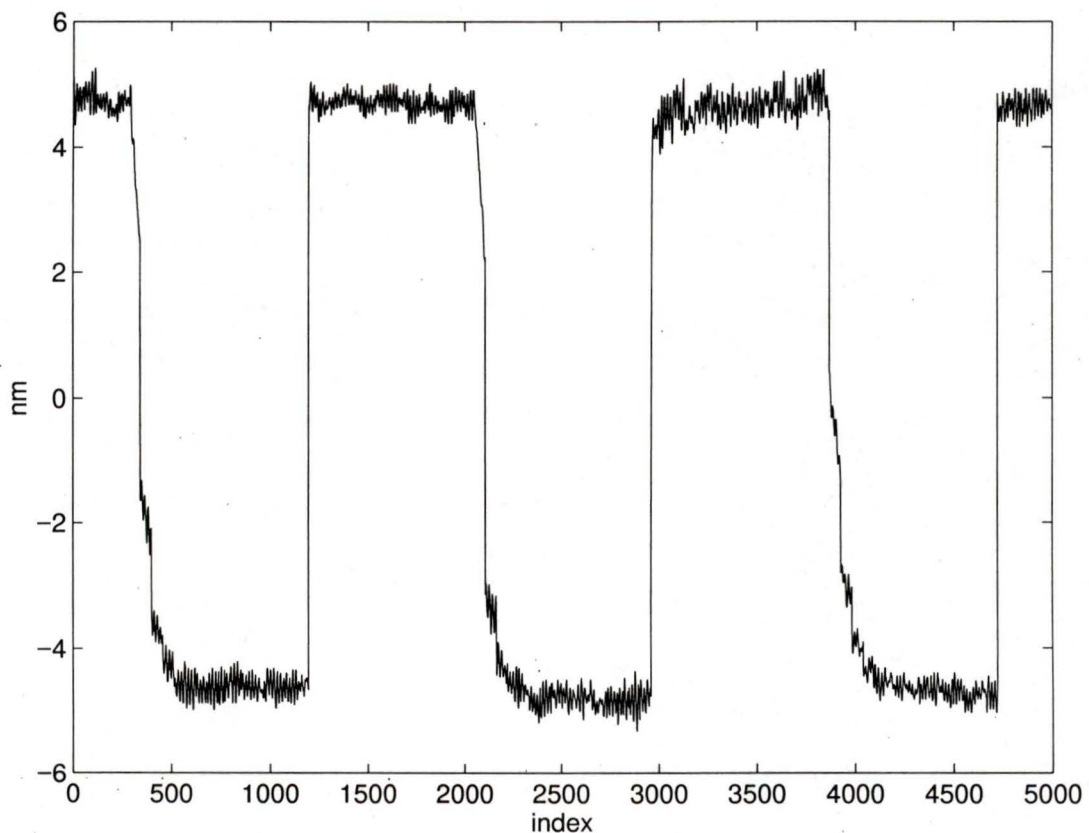


**Figure 8.18:** *1/2 Hz square wave displacement*

A sample of 5000 points was taken over a time period of approximately 5.5 s. This gives a sample frequency of 910 Hz, corresponding to a nyquist frequency of 455 Hz for nm scale deflections.

---

## 9.0 Conclusion

A heterodyne interferometer has been constructed for the purpose of nm scale displacement measurements. The interferometer meets all of the design criteria stated in the introduction: nanometer to sub-nanometer resolution, dynamic range in excess of  $1 \times 10^7$ , sample rate of 910 Hz, and the capability to take accurate displacement measurements in a variety of research areas.

The displacement measurement was calibrated using a piezoelectric ceramic wafer with a known voltage vs. displacement relationship. The heterodyne interferometer resolution was found to be approximately 0.5 nm, with accuracy of approximately 1.5 nm. The interferometer is capable of measuring displacements greater than 1 cm, resulting in a dynamic range greater than  $1 \times 10^7$ . The instrument is susceptible to low frequency drift caused by floor vibrations and changes in temperature, but this is common to almost all high resolution displacement techniques. The instrument is highly resistant to medium frequency noise sources. The heterodyne interferometer is also resistant to changes in laser intensity and changes in ambient light intensity. This resistance to noise, coupled with the non-contact nature of the measurement, makes the instrument both flexible and robust. Finally, the sample rate of the DAQ system was measured to be 910 Hz.

The displacement measurement was found to be extremely sensitive to changes in temperature. It was approximated that the output changes  $200 \text{ nm}/^\circ\text{C}$ . The measured sensitivity to

---

temperature is considerably higher than the value of  $100 \text{ nm}/^\circ\text{C}$  quoted by Charette [37]. This may be due to a different laser cavity size, a less compact design, or different materials used for the optical components.

In addition to temperature induced error, the output also reflects various sources of low frequency seismic disturbances and pressure waves. Low frequency seismic waves created by cars, people walking, and doors closing, pass through solids (and the optical vibration damping system) with very little attenuation. Pressure waves can originate from the ventilation system turning on and off. These disturbances appear in the displacement reading as periodic vibrations on the order of 0.1 Hz. These noise sources are greatly reduced at night or on weekends when there is less activity in the building. It is therefore recommended to take all measurements outside of standard University hours.

The interferometer will enhance many research areas currently being pursued by the IRIS group. Piezoelectric materials being produced in our laboratory can be characterized with greater accuracy and over a larger bandwidth than current equipment allows. The interferometer can also be used in surface profiling of smart structures currently being developed for applications in adaptive optics and vibration control.

## 9.1 Future Work

It is possible to eliminate much of the drift error through measurement of both temperature and pressure. It is recommended that temperature is measured using a thermistor, and pressure using a flexible diaphragm capacitance-type transducer. Both of these instruments are highly sensitive and can provide enough resolution to correct displacement errors due to temperature and pressure fluctuations to within 1 nm. Drift can be further reduced by reducing the optical path lengths of the reference and target beams. This will reduce the effects of vibration and acoustics.

The interferometer is capable of detecting sub-nanometer displacements accurately. To accomplish this, it is necessary to reduce the 60 Hz noise level to significantly less than the current  $\pm 0.5 \text{ nm}$ . The piezoelectric ceramic wafer used to calibrate the interferometer

---

is also capable of displacements with sub-nanometer accuracy provided that the driving voltage is measured with appropriate accuracy. Increasing the accuracy of the heterodyne interferometer would greatly improve the device as a dynamic vibration analysis tool.

---

## 10.0 References

- [1] Sensor Technology Limited, Piezoelectric Ceramics Product Catalogue and Application Notes, pg. 2-3.
- [2] Deferrari H.A, Andrews F.A., "Laser interferometric technique for measuring small-order vibration displacements," J. Acoust. Soc. Am. 39, pg. 979-980 (1966).
- [3] Deferrari H.A., Darby R.A., Andrews F.A., "Vibrational displacement and mode shape measurement by a laser interferometer," J. Acoust. Soc. Am. 42, pg. 982-990 (1967).
- [4] Keller R., Salathe R., Tachudi T., Vourmard C., "Michelson interferometer for detection of fast displacements of less than a quarter wave over small areas," Applied Optics 14, pg. 1616-1620 (1975).
- [5] Mertz L., "Real-time fringe-pattern analysis," Applied Optics 22, pg. 1535 (1983).
- [6] Mertz L., "Optical homodyne phase metrology," Applied Optics 28, pg. 1011 (1989).
- [7] Johnson M., Delaporte Y., "A passive homodyne fibre vibrometer using a three-phase detector array," Meas. Sci. Tech., pg. 854 (1993).
- [8] Mertz L., "Interferometric angle encoder," Rev. Sci. Instrum. 62, pg. 1356 (1991).
- [9] Smith L.M., Dobson C.C., "Absolute displacement measurement using modulation of the spectrum of white light in a Michelson interferometer," Applied Optics 28, pg. 3339 (1989).

- 
- [10] Danielson B.L, Boisrobert C.Y., "Absolute optical ranging using low coherence interferometry," *Applied Optics* 30, pg. 2975 (1991).
- [11] Deck L., Groot P., "High-speed noncontact profiler based on scanning white light interferometry," *Applied Optics* 33, pg. 7335 (1994).
- [12] Chen S., Palmer A.W. Palmer, Grattan K.T.V., Meggitt B.T., "Digital signal-processing techniques for electronically scanned optical fiber white light interferometry," *Applied Optics* 31, pg. 6003 (1992).
- [13] Kino G.S., Chim S.C., "Mirau correlation microscope," *Applied Optics* 29, pg 3885 (1990).
- [14] Takada K., Chida K., Noda J., Nakajima S., "Trench depth measurement system for VLSI DRAM's capacitor cells using optical fiber and Michelson interferometer," *IEEE/OSA J. Lightwave Technol.* LT-5, pg 881-887 (1987).
- [15] Bosselmann T.H., Ulrich R., "High accuracy position sensing with fiber coupled white-light interferometers," in *Proceedings, Second International Conference on Optical Fiber Sensors* (VDE - Verlag, Berlin, 1984), pg. 361-364.
- [16] Fluornay P.A, McClure R.W., Wyntjes G., "White light interferometric thickness gauge," *Applied Optics* 11, 1907-1915 (1972).
- [17] Breen S., Paton B.E., Blackford B.L., Jericho M.H., "Fiber optic displacement sensor with subangstrom resolution," *Applied Optics* 29, pg. 16 (1990).
- [18] Burov J.I., Dentcho I.V., "Multibeam interferometric methods for measuring very small periodic displacements," *Applied Optics* 28, pg. 3343 (1989).
- [19] Thomson J.K., Wickramasinghe H.K., Ash E.A., "A Fabry-Perot acoustic surface vibration detector - application to acoustic holography," *J. Phys. D* 6, pg. 677 (1973).
- [20] M. Bass, *Handbook of Optics*, vol. 1, McGraw Hill. Toronto, 1995, pg. 18.4.
- [21] Hutchins D.A, Macphall J.D., "A new design of capacitance transducer for ultrasonic displacement detection," *J. Phys. E* 18, pg. 69 (1985).
- [22] Kim K.Y., Sachse W., "Self-aligning capacitive transducer for the detection of

- broadband ultrasonic displacement signals," *Rev. Sci. Instrum.* 57, pg. 264 (1986).
- [23] Kim K.Y, Niu L., Castagnede B., Sachse W., "Miniaturized capacitive transducer for detection of broadband ultrasonic displacement signals," *Rev. Sci. Instrum.* 60, pg 2795 (1989).
- [24] Fritsch K., "Linear capacitive displacement sensor with frequency readout," *Rev. Sci. Instrum.* 58, pg. 861 (1987).
- [25] Jones R.V., Instruments and Experiences, Wiley, New York, 1988.
- [26] Whitman R.L., Korpel A., "Probing of Acoustic Surface Perturbations by Coherent Light," *Applied Optics* 8, pg. 1567 (1969).
- [27] Royer D., Dieulesaint E., Martin Y., "Improved Version of a Polarized Beam Heterodyne Interferometer," 1985 Ultrasonics Symposium, pg. 432.
- [28] Lesne J.L., "Optical Heterodyning and Doppler Effect Applied to Laser Vibrometer and Anemometer," *Proc. SPIE*, 2nd European Congress on Optics Applied to Metrology, Strasbourg (France), vol. 210, pg. 36-47 (1979).
- [29] Sommargren G.E., "Heterodyne Profilometry With Circular Scanning," *Applied Optics* 20, pg. 610 (1981).
- [30] Huang C.C., "Optical Heterodyne Profilometer," *Optical Engineering* 23, pg. 365-370 (1984).
- [31] Jean-Loup Lesne, Alain le Brum, "High Bandwidth Laser Heterodyne Interferometer to Measure Transient Mechanical Displacements," *SPIE Vol. 863 Industrial Opto-electronic Measurement Systems Using Coherent Light*, 1987.
- [32] Hecht J., The Laser Guidebook, McGraw-Hill, 1992, pg. 104.
- [33] Melles Griot, Optics, Opto-Mechanics, Lasers, Instruments Catalogue, 1995/1996, pg. 12-22.
- [34] Melles Griot, Optics, Opto-Mechanics, Lasers, Instruments Catalogue, 1995/1996, pg. 12-24 to 12-25.

- 
- [35] M. Bass, Handbook of Optics, vol. 1, McGraw Hill. Toronto, 1995, pg. 5.14.
- [36] Brillouin L., "Diffusion de la Lumiere et des Rayons X Par un Corps Transparent Homgene," *Ann. Physique*, vol. 17, p. 88, 1922.
- [37] P.G. Charette, I.W. Hunter, C.J. Brennan, "A Complete High Performance Heterodyne Interferometer Displacement Transducer for Microactuator Control," *Rev. Sci. Instrum.* 63, pg. 241-248 (1992).
- [38] W. Jung, J. McDonald, "Power Supply Noise Reduction and Filtering", *Analog Devices High Speed Design Techniques*, 1996, pg. 7-34.
- [39] Adolfo Garcia, J. McDonald, "Shielding Concepts", *Analog Devices High Speed Design Techniques*, 1996, pg. 7-89.
- [40] W.T. Estler, "High-accuracy Displacement Interferometry in Air", *Appl. Opt.* 24, March 1985, pg. 808 - 815.
- [41] Bobroff N., "Residual errors in laser interferometry from air turbulence and non-linearity," *Applied Optics* 26, pg 2676 (1987).
- [42] Stone J., Phillips S.D., Mandolfo G.A., "Correction for wavelength variation in precision interferometric displacement measurements," *Journal of Research of the National Institute of Standards and Technology* 101, pg. 671 (1996).
- [43] B. Edlen, "The Refractive Index of Air," *Metrologia* 2, 71 (1966).
- [44] F. Jones, "The Refractive Index of Air," *J. Res. Natl. Bur. Stand.* 86, 27 (1981).
- [45] R. Revell, "Carbon Dioxide and World Climate," *Scientific American* 247, pg. 35 (1982).
- [46] Wallace J., Sensor Technology Limited, personal communication.

---

# 11.0 Appendix A

## Fabry-Perot Interferometer Detection Sensitivity

This appendix expands on the calculation of detection sensitivity for the Fabry-Perot interferometer, given in section . We begin with the classic Fabry-Perot equations [19]. The reflected power  $P_r$  is related to the incident power  $P_i$  by

$$\frac{P_r}{P_i} = 1 - \frac{1}{1 + K \sin^2 \phi} \quad (11.1)$$

where:  $K = \frac{4R}{(1-R)^2}$

$R$  = reflectivity of mirror

$$\phi = \frac{2\pi g}{\lambda}$$

$g$  = mirror spacing

$\lambda$  = wavelength of laser

The sensitivity of the instrument can be written as

$$\sigma = \frac{d}{dg} \left( \frac{P_r}{P_i} \right) \quad (11.2)$$

Note that we will assume that the interferometer has been tuned to a position very close to the maximum sensitivity  $\sigma_0$ , corresponding to a phase angle  $\phi_0$ . This allows us to assume  $\sin\phi \approx \phi$ . Expanding on (11.2)

$$\sigma = \frac{d}{dg} \left( 1 + \frac{1}{1 + K\phi^2} \right) \quad (11.3)$$

Now substitute  $\phi = \frac{2\pi g}{\lambda}$

$$\sigma = \frac{d}{dg} \left( \frac{1}{1 + K \frac{4\pi^2}{\lambda^2} g^2} \right) \quad (11.4)$$

let  $a = \frac{4\pi^2}{\lambda^2}$

$$\sigma = \frac{d}{dg} \left( 1 + Kag^2 \right)^{-1} = - \left( 1 + Kag^2 \right)^{-2} (2Kag) \quad (11.5)$$

To find the maximum sensitivity, take the derivative and set it equal to zero. Begin by evaluating the derivative of  $\sigma$ .

$$\frac{d}{dg} \sigma = 2 \left( 1 + Kag^2 \right)^{-3} (2Kag)^2 - \left( 1 + Kag^2 \right)^{-2} (2Ka) \quad (11.6)$$

rearranging

$$\frac{d}{dg} \sigma = \frac{2 \left( 4K^2 a^2 g^2 \right)}{\left( 1 + Kag^2 \right)^3} - \frac{2Ka \left( 1 + Kag^2 \right)}{\left( 1 + Kag^2 \right)^3} = \frac{8K^2 a^2 g^2 - 2Ka - 2K^2 a^2 g^2}{\left( 1 + Kag^2 \right)^3} \quad (11.7)$$

simplifying

$$\frac{d}{dg}\sigma = \frac{6K^2 a^2 g^2 - 2Ka}{(1 + K a g^2)^3} \quad (11.8)$$

Now set this expression equal to zero to find the maximum sensitivity  $\sigma_o$ .

$$\frac{d}{dg}\sigma_o = \frac{6K^2 a^2 g_o^2 - 2Ka}{(1 + K a g_o^2)^3} = 0 \quad (11.9)$$

$$6K^2 a^2 g_o^2 = 2Ka \quad (11.10)$$

$$g_o^2 = \frac{1}{3Ka} = \frac{\phi_o^2}{a} \quad (11.11)$$

$$\phi_o = \sqrt{\frac{1}{3K}} \pm m\pi \quad (11.12)$$

where:  $m = 0, 1, 2, \dots$

Equation (11.12) gives the phase of the output beam at maximum sensitivity. To find the equation for maximum sensitivity, substitute (11.12) into (11.5).

$$\sigma_o = \frac{-2K a g_o}{(1 + K a g_o^2)^2} = \frac{-2Ka \left( \sqrt{\frac{1}{3Ka}} \right)}{\left( 1 + Ka \left( \frac{1}{3Ka} \right) \right)^2} \quad (11.13)$$

simplify

---

$$\sigma_o = \frac{-2\sqrt{\frac{Ka}{3}}}{\left(1 + \frac{1}{3}\right)^2} = \frac{-2 \cdot \frac{2\pi}{\lambda} \cdot \sqrt{\frac{K}{3}}}{\frac{16}{9}} \quad (11.14)$$

leading to the final result

$$\sigma_o = -\frac{9\pi}{4\lambda}\sqrt{\frac{K}{3}} \quad (11.15)$$

VITA

Surname: Stibich

Given Names: Aaron Leo

Place of Birth: Vancouver, British Columbia, Canada

Educational Institutions Attended:

Okanagan College

1990 - 1991

University of Victoria

1991 - 1997

Degrees Awarded:

B.Eng. (with distinction)

University of Victoria

1995

## PARTIAL COPYRIGHT LICENSE

I hereby grant the right to lend my thesis to users of the University of Victoria Library, and to make single copies only for such users or in response to a request from the Library of any other University, or similar institution, on its behalf or for one of its users. I further agree that permission for extensive copying of this thesis for scholarly purposes may be granted by me or a member of the University designated by me. It is understood that copying or publication of this thesis for financial gain shall not be allowed without my written permission.

Title of Thesis:

Development of a Heterodyne Interferometer For Nanometer Scale Displacement  
Measurement

Author



Aaron Leo Stibich

April 9, 1997